

**Editor-in-Chief B.E.Paton**

**Editorial board:**

Yu.S.Borisov V.F.Grabin  
Yu.Ya.Gretskii A.Ya.Ishchenko  
B.V.Khitrovskaya V.F.Khorunov  
I.V.Krivtsun  
S.I.Kuchuk-Yatsenko  
Yu.N.Lankin V.K.Lebedev  
V.N.Lipodaev L.M.Lobanov  
V.I.Makhnenko A.A.Mazur  
V.F.Moshkin O.K.Nazarenko  
I.K.Pokhodnya I.A.Ryabtsev  
Yu.A.Sterenbogen N.M.Voropai  
K.A.Yushchenko  
A.T.Zelnichenko

**International editorial council:**

N.P.Alyoshin (Russia)  
B.Braithwaite (UK)  
C.Boucher (France)  
Guan Qiao (China)  
U.Diltey (Germany)  
P.Seyffarth (Germany)  
A.S.Zubchenko (Russia)  
T.Eagar (USA)  
K.Inoue (Japan)  
N.I.Nikiforov (Russia)  
B.E.Paton (Ukraine)  
Ya.Pilarczyk (Poland)  
D. von Hofe (Germany)  
Zhang Yanmin (China)  
V.K.Sheleg (Belarus)

**Promotion group:**

V.N.Lipodaev, V.I.Lokteva  
A.T.Zelnichenko (exec. director)  
**Translators:**  
I.N.Kutianova,  
V.F.Orets, T.K.Vasilenko  
**Editor**  
N.A.Dmitrieva  
**Electron galley:**  
I.S.Batasheva, T.Yu.Snegiryova

**Address:**

E.O. Paton Electric Welding Institute,  
International Association «Welding»,  
11, Bozhenko str., 03680, Kyiv, Ukraine  
Tel.: (38044) 287 67 57  
Fax: (38044) 528 04 86  
E-mail: journal@paton.kiev.ua  
http://www.nas.gov.ua/pwj

State Registration Certificate  
KV 4790 of 09.01.2001

**Subscriptions:**

**\$324**, 12 issues per year,  
postage and packaging included.  
Back issues available.

All rights reserved.

This publication and each of the articles  
contained herein are protected by copyright.  
Permission to reproduce material contained in  
this journal must be obtained in writing from  
the Publisher.

Copies of individual articles may be obtained  
from the Publisher.

**CONTENTS**

SCIENTIFIC AND TECHNICAL

**Kuchuk-Yatsenko S.I., Shvets V.I., Gordan G.N.,  
Shvets Yu.V. and Goronkov N.D.** Features of formation  
of structure of joints of rail steel M76 to steel 110G13L  
made by flash-butt welding ..... 2

**Skulsky V.Yu.** Influence of alloying of filler material and  
welded steel on fusion zone structure ..... 9

**Markashova L.I., Grigorenko G.M., Ishchenko A.Ya.,  
Lozovskaya A.V., Kushnaryova O.S., Alekseenko T.A.  
and Chajka A.A.** Effect of scandium additions on  
structure-phase condition of weld metal produced by  
welding aluminium alloy 1460 ..... 16

**Lobanov L.M., Pivtorak V.A., Savitsky V.V. and  
Tkachuk G.I.** Procedure for determination of residual  
stresses in welded joints and structural elements using  
electron speckle-interferometry ..... 24

INDUSTRIAL

**Knysh V.V., Kuzmenko A.Z. and Vojtenko O.V.**  
Increasing fatigue resistance of welded joints by  
high-frequency mechanical peening ..... 30

**Zamkov V.N., Vrzhezhevsky E.L., Topolsky V.F. and  
Petrichenko I.K.** Repair welding of titanium blades of gas  
turbine engine compressors ..... 34

**Snisar V.V., Demchenko E.L., Fenogenov A.I. and  
Vasiliev D.V.** Renovation of bodies of energy-absorbing  
mechanisms of freight railway cars ..... 39

BRIEF INFORMATION

**Kiselevsky F.N., Shapovalov E.V. and Kolyada V.A.**  
System of laser following of weld reinforcement ..... 42

**Maksimov S.Yu. and Krazhanovsky D.V.** Content of  
acicular ferrite in weld metal in wet welding ..... 45

Thesis for a scientific degree ..... 47

NEWS ..... 48

Developed at PWI ..... 8, 15, 23, 29, 41, 44



# FEATURES OF FORMATION OF STRUCTURE OF JOINTS OF RAIL STEEL M76 TO STEEL 110G13L MADE BY FLASH-BUTT WELDING

S.I. KUCHUK-YATSENKO, V.I. SHVETS, G.N. GORDAN, Yu.V. SHVETS and N.D. GORONKOV

E.O. Paton Electric Welding Institute, NASU, Kiev, Ukraine

The paper presents the results of metallographic and X-ray microanalysis of rail steel M76 and steel 110G13L joints, made by pulsed flash-butt welding through an insert of stainless steel 08Kh18N10T.

*Keywords:* flash-butt welding, rail steel M76, 110G13L steel, 08Kh18N10T steel, microstructure, chemical inhomogeneity, heat treatment

In the world practice, flash-butt welding is used in manufacture of railway frogs. Rail ends are welded to a cast frog from 110F13L steel (Hadfield steel), using an insert of austenitic steel.

According to the accepted technology [1], an austenitic insert, in which chromium, carbon and titanium content is specified, is welded to a rail end, the butt joint is annealed at 350–1000 °C for 2–5 h, and cooled in air. Then a high-manganese core of the frog is welded to the insert with subsequent cooling in air. Welding is performed with intermittent resistant preheating with subsequent surface melting.

The E.O. Paton Electric Welding Institute developed a technology of welding railway frogs based on pulsed flash-butt welding that provides a highly concentrated heating and, therefore, a narrower HAZ. Technology envisages application of an insert of standard austenitic steel without postweld heat treatment of the joints. Operating sequence is the same [2].

The purpose of this work is investigation of the microstructure and chemical inhomogeneity of the joint metal and their influence on mechanical properties of the latter.

The paper deals with joints of R65 rails from steel M76 with cast billets of steel 110G13L, welded through an austenitic insert, corresponding to the rail profile and made from standard rolled stock of 08Kh18N10T steel. Welding was performed in the modes ensuring the strength and ductility values required by the specification [3]. At mode selection the

heat input was varied by changing the process duration. Optimum width of austenitic insert was taken to be equal to 15–20 mm. Steel composition is given in Table 1.

Metallographic examination was conducted in the optical microscope Neophot-32. The CAMEBAX microanalyzer MS-50 was used for X-ray microanalysis. Microhardness of the structural components was measured in the LECO hardness meter.

General view of the microstructure of a three-element welded joint is shown in Figure 1.

As is seen, intermittent globular, as well as growing from the boundary crystallographically oriented acicular carbides were revealed along the grain boundaries in the HAZ of austenitic steel 110G13L (Figure 1, a). A band of homogeneous austenite forms at the contact boundary. This is in agreement with the published data [4]: intensive precipitation of  $(\text{FeMn})_3\text{C}$  carbide accompanied by a decrease of the mechanical properties proceeds in 110G13L steel in the temperature range of 250–800 °C (250–950 °C by the data of [5]). In the above welding mode, carbide formation is not developed and does not influence the strength properties of the joint, because of the short-term heating.

The metal develops austenitic structural components of an intermediate composition along the line of the joint of 110G13L and 08Kh18N10T steel. Microhardness in the transition zone varies in the range of HV 0.5-1880–2900, which is indicative of the absence of phases leading to embrittlement.

Microstructure of 08Kh18N10T steel in the middle region of the insert is that of polygonal austenite with

**Table 1.** Composition (wt.%) of steels welded

Steel	Cr	Ni	Mn	Ti	Si	C	P	S	Cu
08Kh18N10T (insert)	17.2	9.7	0.90	0.55	0.620	0.072	0.034	0.014	0.23
M76 (rail)	--	--	0.81	--	0.029	0.724	0.007	0.014	--
110G13L (frog)	--	--	14.10	--	--	1.200	0.030	0.002	--

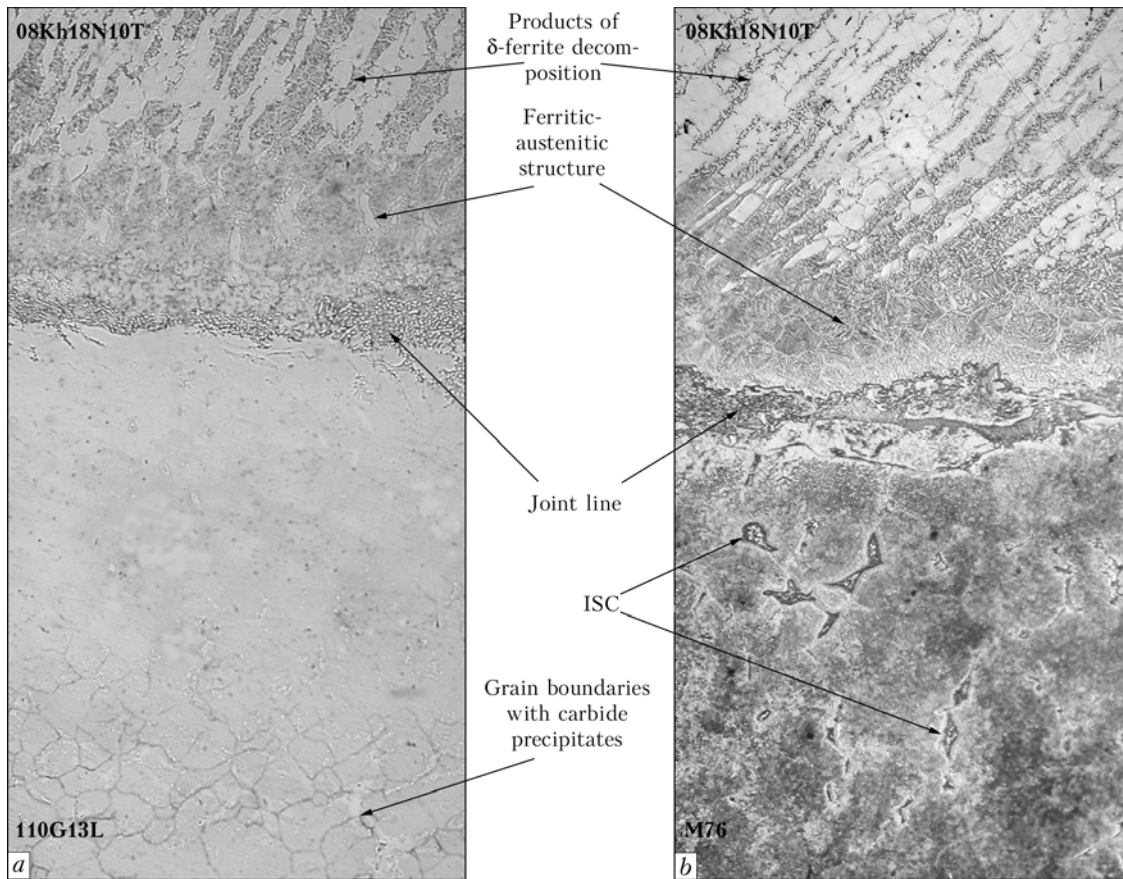


**Figure 1.** Microstructure of transition zone on contact boundary of joint of 08Kh18N10T and 110G13L steels (a) and 08Kh18N10T and M76 steels (b) (x50)

δ-ferrite inclusions, elongated along the rolling direction. Products of decomposition of δ-ferrite and an austenitic-ferritic layer formed as a result of phase recrystallization, are observed in the near-contact regions 5–6 mm wide, both on the side of M76 steel, and on the side of 110G13L steel (Figure 1, a and b).

Microstructure of the HAZ metal of rail steel M76 (Figure 1, b) is close to that of a similar joint [6]. Its difference from the similar joint consists in that the volume fraction of free ferrite is higher in the near-contact zone. A decarbonated layer of ferrite forms along the boundary (Table 2, Nos. 1, 2) with microhardness *HV* 0.1-1270.

A characteristic feature of the joint is presence of a light-coloured structural component in the rail steel

at down to 3 mm depth. We will call this structural component located between the grain blocks, the interblock structural component (ISC).

Microstructure of the metal along the joint line of M76 and 08Kh18N10T steels is non-uniform within its surface (Figure 2), and requires a more detailed study.

Alongside sections of direct contact of rail steel and 08Kh18N10T steel (Figure 3, a), also sections with an intermediate structure similar to that of the cast metal (Figure 3, c) are observed. An acicular phase is found in austenitic grains of 08Kh18N10T steel (Figure 3, b). In the ferrite layer of rail steel new structural elements of an oval shape with a high hardness of *HV* 0.1-6130 may appear (Figure 3, d).

**Table 2.** Composition (wt.%) of structural components of near-contact layer of rail steel M76

No.	Structural component	Si	Ti	Cr	Mn	Ni	Fe	C
1	Ferrite in near-contact layer of M76	0.392	0.014	0.207	1.076	0.010	99.109	0
2		0.431	0.012	0.015	0.993	0	98.548	0
3	Acicular phase in near-contact layer of 08Kh18N10T	0.594	0.153	10.457	1.242	7.585	79.958	0.012
4	Oval structural elements in near-contact layer of M76	0.464	0.042	2.893	0.961	1.150	93.928	0.142
5	Light-coloured phase in ISC	0.539	0.026	5.266	1.389	1.774	90.018	0.978
6	ISC–matrix interface in M76	0.497	0.020	2.631	1.125	2.047	92.488	1.193
7	Boundary of grains between ISC	0.598	1.328	3.753	1.313	1.839	88.652	2.518
8		0.474	0.046	1.285	0.972	0.569	95.434	1.220

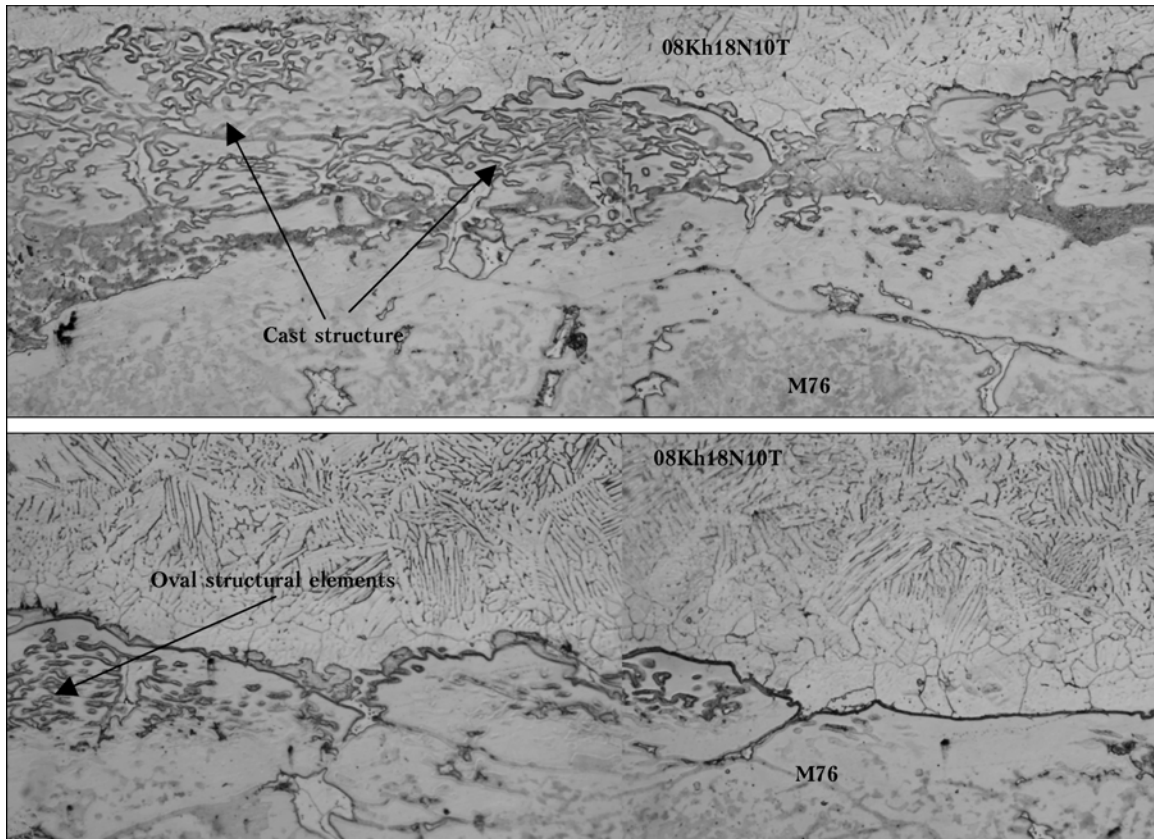


**Figure 2.** Microstructure of metal along the joint line of steels 08Kh18N10T and M76 ( $\times 250$ )

As is seen from the progress of the curves of element distribution in Figure 4, a, in the section of direct contact chromium distribution proceeds jump-like at transition through the contact boundary. The joint forms at practically complete pressing of the melt out of the joint zone.

In the section with an acicular phase in 08Kh18N10T steel, the monotonically decreasing curve of chromium distribution changes to a horizontal plateau (Figure 4, b). A peak corresponding to 0.7 wt.% Ti is observed on the curve of titanium distribution on the contact boundary. Carbon content also rises. It is obvious that in this case, the melt not pressed out of the joint zone, solidifies on steel 08Kh18N10T. Similar to carbon, titanium at solidification is ousted into the liquid phase and localized on the boundary.

Solidifying austenite contains 10.457 wt.% Cr and 7.585 wt.% Ni (Table 2, No.3). At such a content of these elements, austenite loses its stability, this leading to hardening structure formation.

The observed peaks on the curves of chromium and carbon distribution at transition into rail steel were obtained at intersection of the oval elements of the structure.

Analysis of the composition of microvolumes showed that in addition to chromium, the oval structural elements contain nickel and titanium, as well as carbon. Carbon and titanium content is small, being higher, however, than in the surrounding metal (Table 2, No.4).

Apparently, the oval structural elements formed in the sites of partial melting of rail steel. A higher solubility in the liquid phase leads to enrichment of the formed melt volumes in alloying elements diffusing through the surrounding hard metal from the melt on the boundary.

Progress of the curve of chromium distribution in the region with the cast metal structure (Figure 4, c) is indicative of cast structure formation on the basis of rail steel M76. Two structural components are present in the microstructure of the considered regions. One of them contains 10.405 wt.% Cr and 7.058 wt.% Ni, and the other component has 8.828 and 5.712 wt.%, respectively. Microhardness ( $HV$  0.1-3450, 5330 and 4530) of these structural components is much higher than in the adjacent layers of rail steel M76, and of austenite of 08Kh18N10T steel, being  $HV$  0.1-1270,  $HV$  0.1-2160, respectively.

It is obvious that the cast structure is the result of development of partial melting of rail steel. Partial melting of inner volumes of the near-boundary layer is caused by heating of rail steel M76 at the edge up to temperatures which are in the melting temperature range, its width being 90 °C. New oval structural elements in M76 steel are observed at the initial stage of the solid-liquid layer formation. If this process becomes developed, then the near-boundary layer of rail steel is in the solid-liquid state. No pressing-out of metal occurs at upsetting in the solid-liquid state. Structures similar to cast metal form in the metal along the joint line.

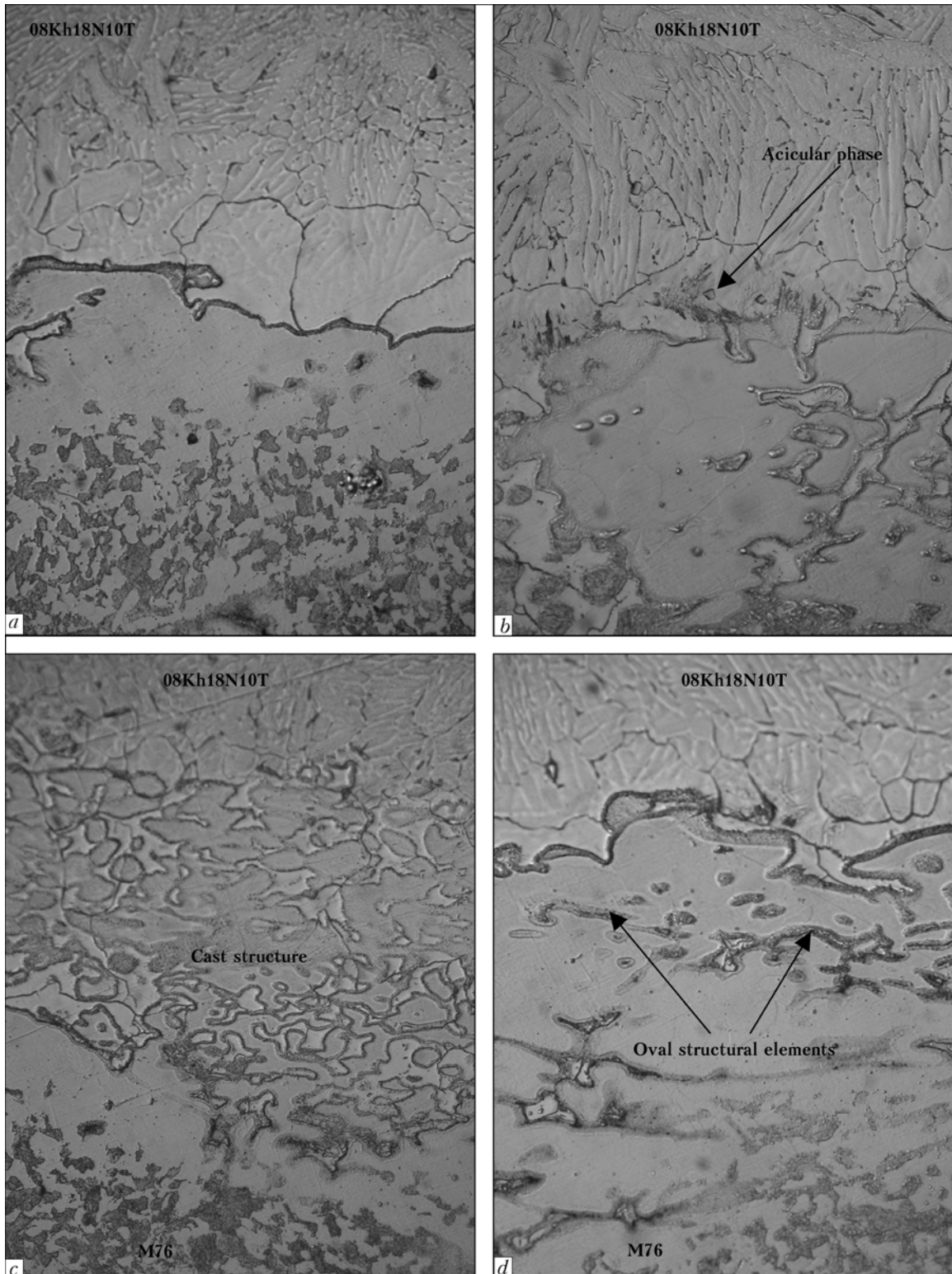


**Figure 3.** Characteristic sections of microstructure of metal along the line of 08Kh18N10T to M76 joint: *a* — direct contact of joined steels; *b* — acicular phase in near-contact grains of 08Kh18N10T steel austenite; *c* — «cast structure»; *d* — oval structural elements in ferrite layer of rail steel M76 ( $\times 500$ )

Mixing of the liquid phase of the solid-liquid layer with the joint zone melt increases the content of Cr–Ni steel elements in it. Residual regions of the solid phase have a lower, but still high content of Cr–Ni steel elements.

Thus, a number of phases of an intermediate composition form in the metal layer along the joint line,

which may lead to formation of carbides and hardening structures. It should be noted that their volume fraction in the weld metal determines the ductile properties of the joint. In view of the spreading of these phases and their non-uniform distribution within the joint surface, they do not lead to any considerable lowering of the ductile properties.

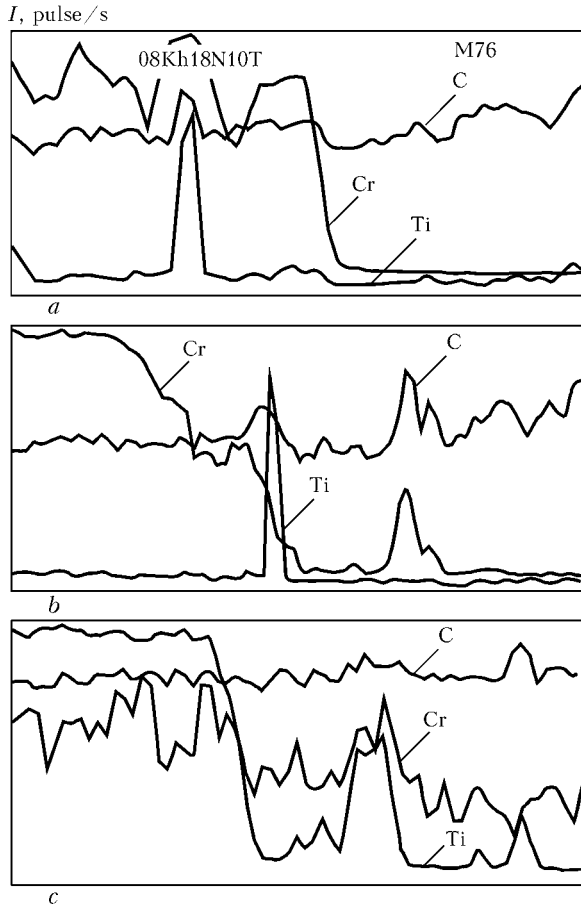


**Figure 4.** Profilegrams of element distribution in characteristic regions of metal layer microstructure along joint line of steels 08Kh18N10T and M76: a-c — see Figure 3

ISC investigation revealed its structural inhomogeneity (Figure 5). Fine inclusions and acicular phase are observed on the boundary with the matrix. Formation of the latter is also found in the ISC volume. In a number of cases non-metallic inclusions and eutectic colonies are also found in the ISC.

Microhardness of ISC light field is equal to *HV* 0.1-4130, and in the places of acicular phase accumulation it reaches *HV* 0.1-6130, this being much higher than that of the neighbouring grains of the sorbite of rail steel M76 (*HV* 0.1-3120).

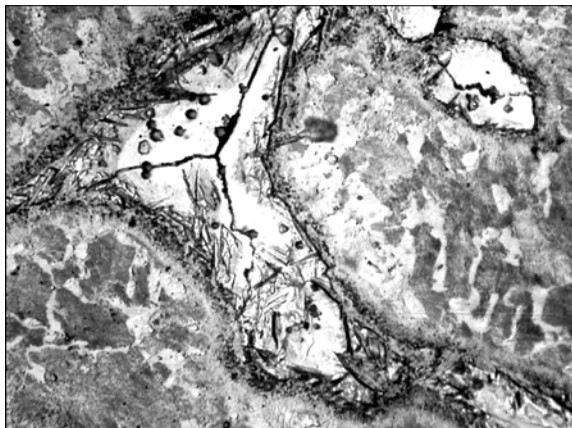


**Figure 5.** Microstructure of ISC formed in M76 to 08Kh18N10T joint (×1000)

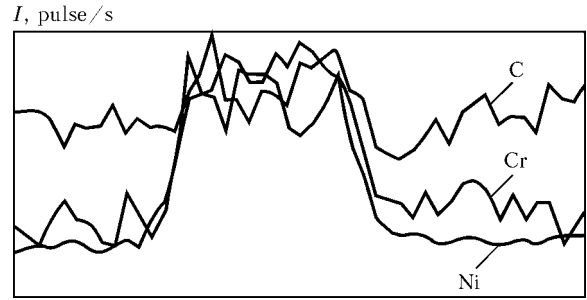


**Figure 6.** Profilegram of element distribution at ISC scanning

Analysis of element distribution at ISC linear scanning (Figure 6) showed that it contains nickel and chromium, i.e. elements of Cr–Ni steel. Carbon content is higher than in rail steel.

According to the results of analysis of the composition of metal microvolume (Table 2, Nos. 5 and 6) within ISC the content of elements was as follows, wt. %: 0.978–1.193C, 1.125–1.389Mn, 1.774–2.047Ni, 2.631–5.277Cr, the regions at the boundary being depleted in chromium. ISC also contains 0.200–0.026 wt. % Ti.

In individual regions of the grain boundaries between ISC a higher content of alloying elements was registered, wt. %: 1.238Ti, 3.753Cr and 2.518C (Table 2, Nos. 7 and 8).

It is obvious that ISC forms as a result of penetration of Cr–Ni steel elements along the grain boundaries into rail steel to a distance greatly exceeding the capabilities of solid phase diffusion. Considering that it forms predominantly in the sites of clustering of non-metallic inclusions of the type of sulphides and phosphides, which may produce low-melting eutectics as a result of concentration surface melting (eutectics with melting temperature of about 1000 °C are found in Fe–Mn–S, Fe–P, Fe–Mn–P, Fe–Cr–Ni–Ti–C systems [4, 5]), ISC formation is attributable to diffusion through the surface melted metal on grain boundaries.

High deformation at upsetting promotes opening of grain boundaries and melt penetration from the joint zone into the volumes between the grain blocks.

Higher content of carbon and manganese in ISC compared to rail steel is caused by their diffusion from

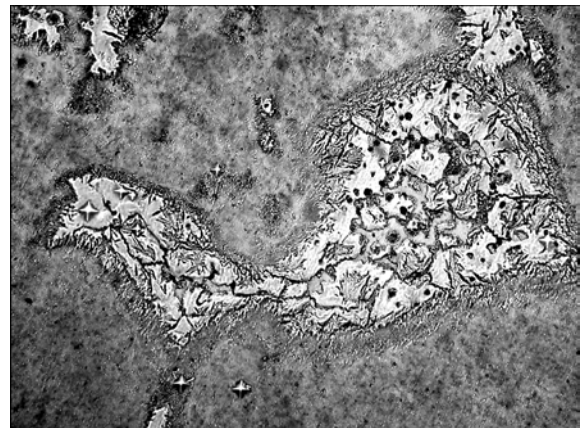


**Figure 7.** ISC microstructure after annealing at 550 °C (×1000)



the matrix as a result of a higher solubility in the liquid phase.

Fine inclusions fringing the ISC, probably, are carbide phases. Carbide phases of such active carbide-forming elements as titanium and chromium, may also form on the boundaries of grains connecting the individual ISC, along which these element diffuse into the rail steel.

ISC acicular phase, probably, is the product of martensite transformation of alloyed austenite.

In the microstructure of ISC of a large volume, grain boundaries, and in some cases also eutectic colonies, are detected, which were found to be enriched in phosphorus (about 12 wt.%).

Results of microstructural examination suggest that ISC have a low ductility, and may be the source of crack initiation and propagation. This suggestion was confirmed during performance of full-scale testing for static and impact bending. In 80 % of the cases samples failed in the rail steel HAZ at 2–3 mm distance from the contact boundary, i.e. in the sections, where ISC is present. In addition, increase of welding heat input causing an increase of ISC volume fraction, leads to lowering of the joint strength properties at testing for static bending (deflection, breaking load).

Heat treatment by subsequent heating at 550 and 850 °C with soaking for 2 h in both the cases was conducted to improve the strength properties of M76 and 08Kh18N10T steels.

For joints of steels 110G13L and 08Kh18N10T the issue of heat treatment application was not considered, since, as it is known from [4], this would have led to a considerable deterioration of the properties of steel 110G13L.

It is established that after annealing at 550 °C in the HAZ of M76 steel the lamellar pearlite turns into granular pearlite as a result of coagulation of the carbide phase. Precipitation of globular carbides in the form of bands fringing the ISC and connecting the ISC to each other is noted. Carbides are also formed on the contact boundary of steel M76 and on the boundary of sections of partial melting of steel M76. Acicular phase and eutectic colonies in the ISC volume are preserved (Figure 7), and mechanical properties stay at the same level at full-scale testing.

In the case of annealing at 850 °C the acicular phase disappears from ISC as a result of phase recrystallization, while carbide formation becomes more intensive. Numerous inclusions of globular carbides fill practically all the ISC volume (Figure 8, a).

Carbide clusters are also found in the metal layer on the joint line in the regions of partial melting of M76 steel (Figure 8, c), and in austenitic grains of 08Kh18N10T steel (Figure 8, b). Considering the low content of carbon in the metal of the joint line, formation of chromium carbides can be assumed in this case.

A low density of carbide inclusions, particularly, if this pertains to boundary precipitates in 08Kh18N10T steel, lowers the ductility.

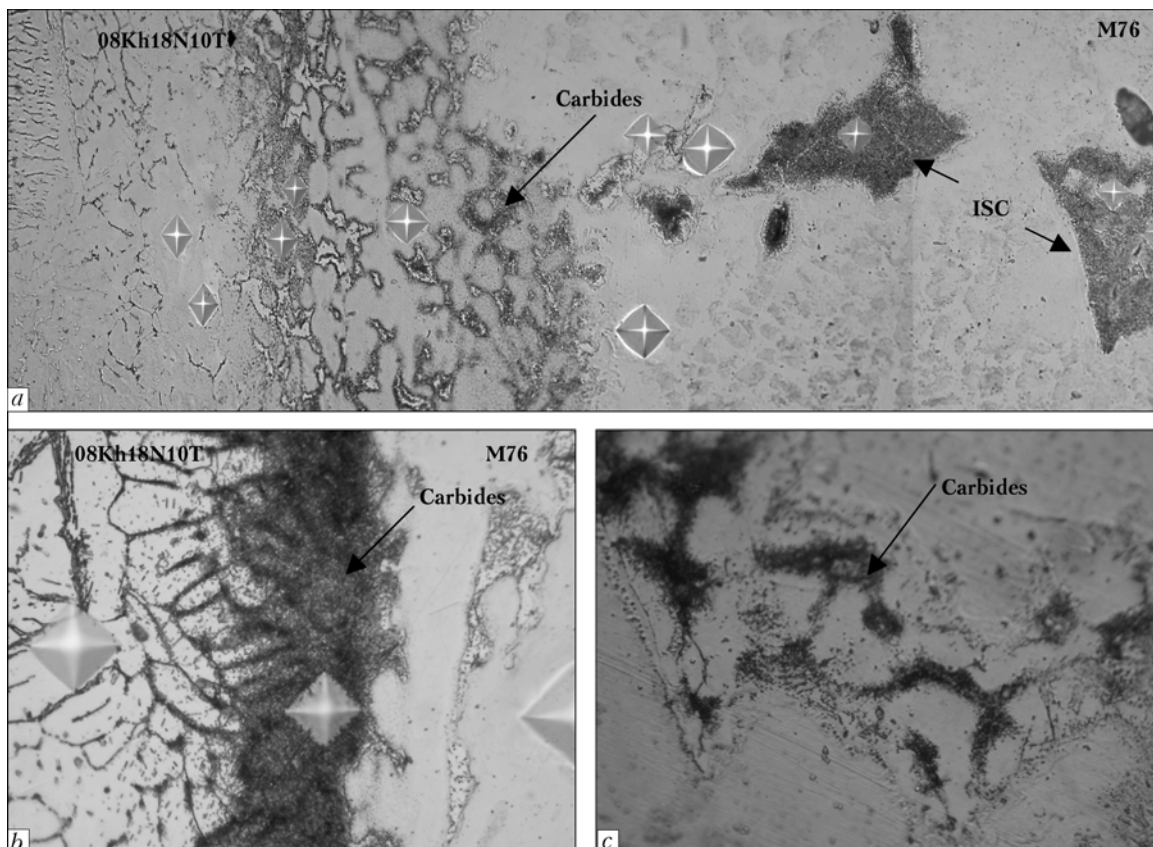


**Figure 8.** Microstructure of joint of M76 and 08Kh18N10T steels after annealing at 850 °C: a — transition zone ( $\times 25$ ); b — carbides in 08Kh18N10T steel on the contact boundary ( $\times 1000$ ); c — carbides in metal on the joint line ( $\times 1000$ )



For this reason, as shown by full-scale testing, heat treatment does not yield any essential improvement of the joint properties.

It appears to be efficient to limit the volume fraction of unfavourable structural components lowering the ductile properties, by increasing the heating rate and shortening heating duration.

Elimination of heat treatment enables eliminating the limitations on carbon content in 08Kh18N10T steel.

## CONCLUSIONS

1. Non-equilibrium structural components of an intermediate composition prone to transformations with carbide precipitation and formation of hardening structures, form in the metal of joints of M76 rail steel and 110G13L steel, made by flash-butt welding through an intermediate insert from steel 08Kh18N10T.

2. Mechanical strength and ductility values of the joints are quite high, due to an isolated and non-uniform nature of these structural component distribution. Improvement of these values is observed at reduction of their volume fraction.

3. Application of postweld heat treatment is ineffective, as it causes formation of high-density carbide clusters in the joint structure.

4. Use of welding technologies, which envisage highly concentrated heating in combination with a controllable thermoderformational process, provides rather high mechanical properties of the joints of the above steels, meeting the specification requirements.

1. Blulsauer, I. *Method of joining railway point parts from austenite high-manganese steel castings to carbon steel rail*. Appl. 91890157.0 Europe. Int. Cl. 0 476 881 A1. Publ. 22.01.92.
2. Kuchuk-Yatsenko, S.I., Shvets, Yu.V., Dumchev, E.A. et al. (2005) Flash-butt welding of railway frogs with rail ends using an intermediate insert. *The Paton Welding J.*, 1, 2-4.
3. *DP 32-4520.13.500-007-2002 TU*: Railway frog and core with welded rail ends of R65, R50 and USC60 type using an insert or without it. Test batch. Valid from 01.01.2003 to 01.01.2006.
4. Gruzin, P.L., Grigorin, V.I., Mural, V.V. et al. (1969) Transformations in high-manganese austenitic steel. *Metallovedenie i Termooobrabotka Metallov*, 1, 5-9.
5. Tkachenko, F.K., Efremenko, V.G. (1990) Structure and phase transformations in deformed high-manganese steel. *Ibid.*, 2, 8-10.
6. Kuchuk-Yatsenko, S.I. (1992) *Flash-butt welding*. Kiev: Naukova Dumka.

## ADVANCED TECHNOLOGY OF UNDERWATER FLASH-BUTT WELDING OF OFF-SHORE PIPELINES

E.O. Paton Electric Welding Institute has an advanced highly productive technology of automatic underwater welding of pipes, which is based on the results of a R&D package on flash-butt welding. Welding is performed in a local chamber with just the welding zone being insulated from the water.

Full automation of the welding cycle allows excluding the participation of welders-divers and increasing the safety of underwater operations. The technology provides a high and stable quality of welded joints at a high efficiency, irrespective of the diving depth. Equipment is fitted with a highly reliable, verified in practice system of on-line control of weld quality.



Lowering under the water of the flash-butt welding machine used for welding pipelines

Macrosection of a welded joint made under water



**Purpose and application.** Technology is designed for underwater welding of pipes in construction and repair of off-shore pipelines.

**Status and level of development.** Developed machine for underwater flash-butt welding of pipes of 57–325 mm diameter was tested in the actual conditions of the Black Sea at down to 60 m depth. Welded joints completely satisfied the requirements of API 1104 standard on all the indices. Repair of an underwater pipeline of 219 mm diameter with 20 mm wall thickness was performed. Technologies of flash-butt welding were developed for construction and repair of off-shore pipelines under water.

**Form of co-operation.** To be determined through negotiations. PWI is open to co-operation with companies to develop highly efficient underwater complexes for construction and repair of off-shore

Contacts: Prof. Kuchuk-Yatsenko S.I.  
E-mail: chvertko@paton.kiev.ua



# INFLUENCE OF ALLOYING OF FILLER MATERIAL AND WELDED STEEL ON FUSION ZONE STRUCTURE

V. Yu. SKULSKY

E.O. Paton Electric Welding Institute, NASU, Kiev, Ukraine

Features of structure formation in the fusion zone of joints on materials of different alloying systems and pertaining to different structural classes are considered in the case of welded joints made on steels using welding consumables. Depending upon the relationship of temperatures of the solidification range  $T_L$ - $T_S$  of the base and weld metal, partial melting of the grains may develop in the fusion zone, its degree being determined by the differences in the values of these temperatures for the combined materials and cooling of the metal in the near-weld zone. The final structure is influenced by the thermodynamic activity of carbon and its redistribution between the weld and base metal, which also depends on the combined material alloying.

*Keywords:* arc welding, fusion zone, dissimilar and similar joints, solidification ranges, latent melting heat, molten pool, base metal, melting of grains, carbon redistribution

Study of properties of the martensite heat-resistant steel with increased content of chromium (~ 9 wt.%) showed that in welded joints, produced using identically alloyed welding consumables, between weld and HAZ metals a zone is formed, morphology of which is similar to that of cast metal, but different from the weld structure [1]. It is shown that this zone relates to the base metal (BM), in which grains were submitted to heating up to the temperatures of their partial or complete melting, while the BM melt, which was formed as a result of this process, did not participate in mixing with a deposited filler metal and formed so called unmixed zone [2, 3]. In such areas of fusion zone (FZ) occurrence of separate light grains was noted, presumably relating to  $\delta$ -ferrite, which formed as a result of phase transformation caused by metal overheating before melting of the inter-grain areas and carbon redistribution [1]. Formation of such structure in joints of the studied heat-resistant high-chromium steels is regularly observed both in manual and mechanized fusion welding. Experiments with application of austenite consumables in welding of chro-

mium steel showed that metal structure in FZ may change. In general, change of the content of alloying elements in composition of welding consumables (the level of alloying) is accompanied not just by production of a certain structural state of the deposited material (the weld metal), but also by achievement of other values of its critical temperatures liquidus-solidus ( $T_L$ - $T_S$ ).

The goal of this work consisted in study of regularities of formation of the FZ metal structure in welded joints, produced as a result of combination of several types of base and filler materials having both different structural classes and level of solidification range temperatures  $T_L$ - $T_S$ .

Represented in this work steels, welding wires and electrodes (Table 1), are used in different fields and are selected only for the purpose of modeling various types of experimental joints. Values  $T_L$ - $T_S$  were determined using differential thermal analysis. Combinations of materials, used for producing experimental joints, are given in Table 2. Microsection of specimens for metallographic studies were cut across longitudinal axis of produced beads. Determination of FZ microstructure in the metal of martensite structure was carried out by chemical etching in solution of hydrochloric

**Table 1.** List of materials with different type of alloying

Material	Structural class	$T_S$ , °C	$T_L$ , °C
Steel R91 (0.12C-9Cr-MoVNbNiN)	$\dot{I}$ *	1480	1515
Steel EP794 (02Kh8N22C6)	$\dot{A}$ *	1250	1380
Flux-cored wire PP9 (0.12C-9Cr-MoVNbNiN)	$\dot{I}$	1480	1515
Wire (Sv-04Kh19N9T)	$\dot{A}$	1380	1440**
Coated electrodes R89 (experimental ones) (0.12C-9Cr-MoVNbNiN)	$\dot{I}$	1480	1515
Coated electrodes KTI-9A (0.12C-11Cr-NiMoV)	$\dot{I}$	N/D	
Coated electrodes ANV-17 (02Kh19N18G5AM4)	$\dot{A}$	1330	1380
Coated electrodes MNCh-2 (65Ni-Cu)	$\dot{A}$	1290	1330**

\* M --- martensite, A --- austenite; \*\* --- data obtained on the cooling branch.

**Table 2.** Combinations of materials in studied joints and conditions of their producing

Combination of material types		Characteristics of welding (deposition) process
Welded steel (structural class)	Electrode material	
R91 (M)	PP9 (M)	Automatic deposition of bead on surface of steel using flux SFT9: $d_{\text{wire}} = 3.2 \text{ mm}$ ; $I_w = 350\text{--}370 \text{ A}$ ; $U_a = 37\text{--}39 \text{ V}$ ; $v_w = 19 \text{ m/h}$
R91 (M)	Sv-04Kh19N9T (A)	Automatic deposition of bead on surface of steel using flux SFT9: $d_{\text{wire}} = 3 \text{ mm}$ ; $I_w = 330\text{--}360 \text{ A}$ ; $U_a = 37\text{--}39 \text{ V}$ ; $v_w = 19 \text{ m/h}$
R91 (M)	ANV-17 (A)	Deposition of bead on steel using manual arc welding: $d_{\text{el}} = 3 \text{ mm}$ ; $I_w = 110\text{--}115 \text{ A}$ ; $U_a = 22\text{--}24 \text{ V}$
R91 (M)	MNCh-2 (A)	Deposition of bead on steel into V-shape groove using manual arc welding: $d_{\text{el}} = 3 \text{ mm}$ ; $I_w = 100\text{--}115 \text{ A}$ ; $U_a = 22\text{--}24 \text{ V}$
EP794 (A)	R89 (M)	Manual welding of butt joint with V-groov: $d_{\text{el}} = 3 \text{ mm}$ ; $I_w = 115\text{--}120 \text{ A}$ ; $U_a = 22\text{--}24 \text{ V}$

ric acid, while in high-alloy metal it was determined electrolytically in solution of oxalic acid. Light microscope Neophot-32 was used for study of the microstructure. Microhardness was studied using hardness gauge PMT-3. X-ray micro-spectral analysis was carried out using the CAMEBAX installation.

Steels and consumables were selected in such way that values of solidification range temperatures ( $T_L$ – $T_S$ ) in produced joints were identical, lower and higher than in BM. Experiments were carried out

mainly using steel with 9 wt.% Cr, which relates to the group of new heat-resistant steels and is important for research.

**Similar combination of martensite materials (M–M).** FZ microstructure, produced in case of equality of thermal-physical characteristics of the welded martensite steel and a deposited metal, is shown in Figure 1. Graphic presentation of values  $T_L$ – $T_S$  allows approximate estimating values of these temperatures for the weld metal depending upon the share of the base and the filler metals (FM). In this case irrespective of the mixing degree identity of solidification range temperatures of the steel, pure electrode material and the joint metal is preserved. As it was already noted, the structure in FZ (in manual and mechanized processes of welding) is formed during melting of BM grains, beginning from inter-grain boundaries and practically till their complete melting. Completeness of melting of the BM grains is affected by the degree of preheating of adjacent to the molten pool edges (as a result of the heat emitted by the welding arc, waste gas, and free-stream convective flows) and character of dissipation of heat, which passes through the pool walls.

Convective flows represent rather powerful mechanism of entrainment into the process of mixing of liquid phases in the pool. Under action of these flows (Figure 2) even takes place separation of mutually bonded BM grains, although such groups, evidently, have lower mobility than liquid metal. Formation of liquid inter-grain interlayers, along which takes place breaking of the groups of more strongly inter-bonded grains, should be considered the reason of this separation. Although mobility of the liquid increases by means of approaching the pool walls, speed of its displacement reduces because of the action of inter-phase tension near the boundary metal–liquid and friction (tangent stresses) between the layers. As a result mixing worsens, and area of variable chemical composition forms.

Hence one may draw conclusion that probable condition for preservation near the pool walls of the liquid BM layer, which would not mix up with the pool metal, is attenuation and absence of convection in the

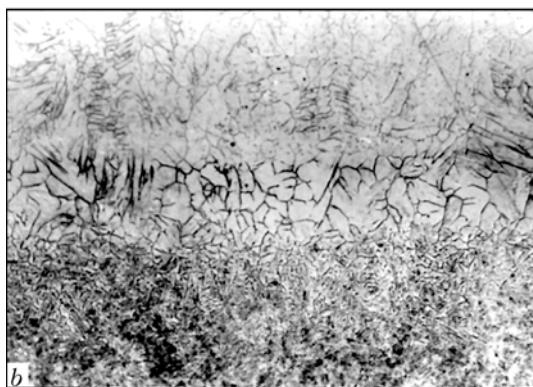
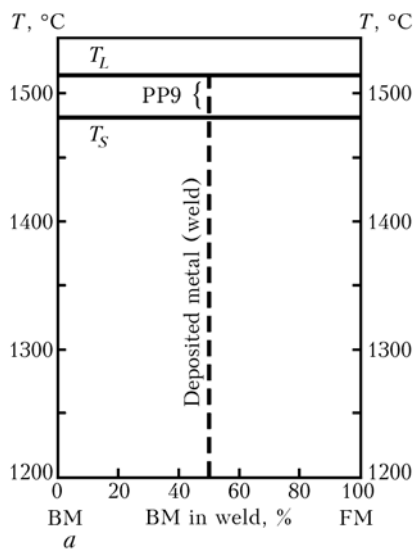


**Figure 1.** Schematic presentation of  $T_L$ – $T_S$  range for BM (steel R91), metal deposited by filler wire PP9 and metal of single-layer bead deposited on steel in similar combination of M–M (a) type, and metal microstructure in FZ (b) ( $\times 250$ )

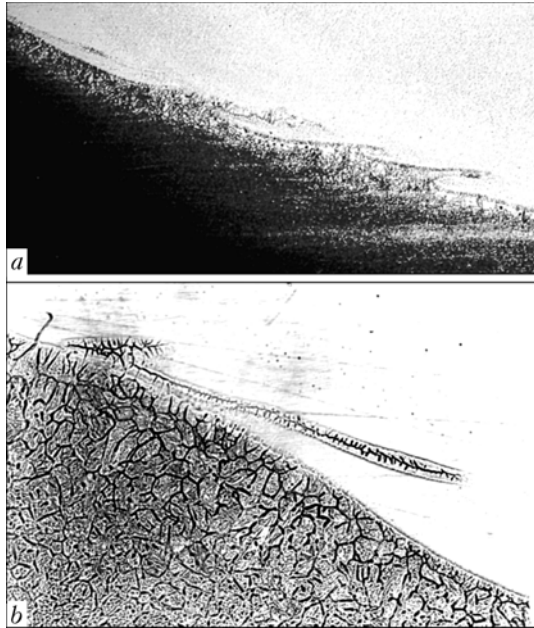


**Figure 2.** Microstructure of metal in FZ with separated layers of BM under action of convective flows in deposition of beads on martensite steel using austenite welding consumables (combination M-A): a — wire Sv-04Kh19N9T ( $\times 50$ ); b — electrode ANV-17 ( $\times 250$ )

near-wall area. The latter condition is possible only provided solidification of a certain portion of the weld metal is sufficiently developed. In this case the melt along the boundary weld-BM should originate after beginning of solidification of the adjacent portions of the weld metal as a result of additional overheating of BM by the heat, released by the weld metal during its cooling before aggregate state starts to change, and by the released latent heat of melting.

So, first solidification of the weld metal, accompanied by the melt cooling and formation in it of crystalline frame, which excludes convection, and release of latent heat of melting, and then formation (or preservation and increase of the quantity of earlier formed) of interlayer of liquid BM as a result of consumption by it of a portion of released by the weld latent heat of melting will be observed. According to [4, 5], exactly released latent heat of melting is the main factor, which is able to cause additional overheating of the metal from the near-solidus temperatures to the melt point and formation of a layer of molten BM over weld edges. It follows from this that the higher is temperature of the weld metal solidification range in comparison with that of the welded steel, the more developed should be steel melting during solidification of the weld. This statement is confirmed by presented below results of the experiments.

In similar joints considered above, the most favorable conditions for development of melting of the BM grains and formation of non-mixed zone are created in proximity of shoulders (the area, designated by a circle in Figure 3), which are formed as a result of drastic transition from less deep to more deep penetration, which is characteristic of welds with central tongue-like penetration in cross-section. Here juxta-

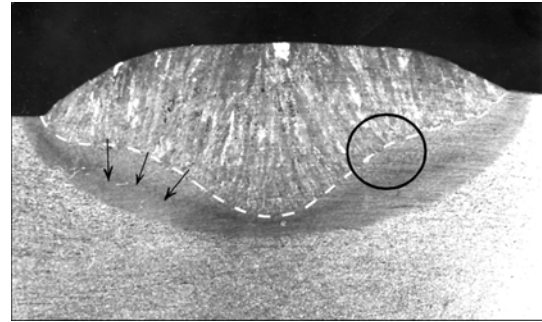


**Figure 3.** Macrosection of weld with central deep penetration and variable width of formed HAZ (circle indicates area of maximum FZ width, arrows indicate schematic direction of emanated from the interface weld-BM intersecting heat flows)

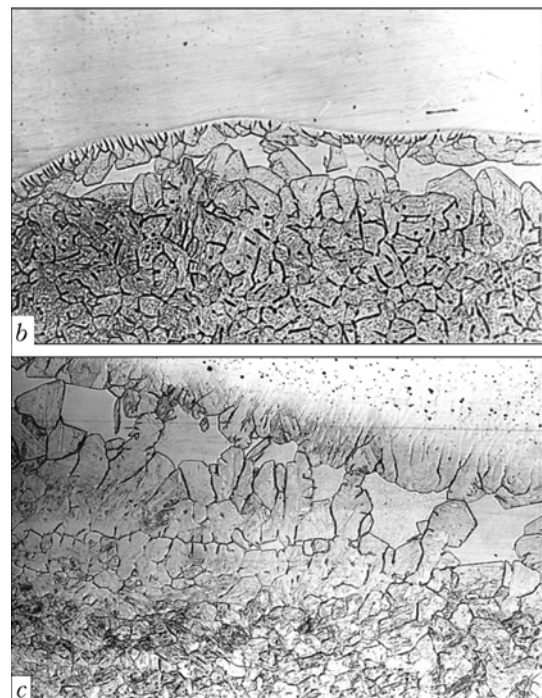
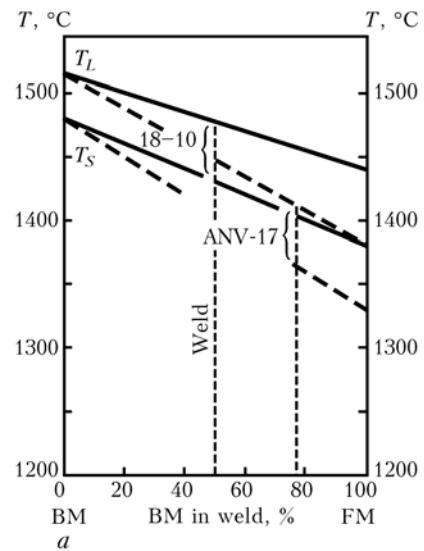


**Figure 4.** Schematic presentation of  $T_L-T_S$  range for steel R91, metal deposited by electrodes ANV-17 and wire Sv-04Kh19N9T and metal produced in manual (with electrodes ANV-17) and mechanized (with wire Sv-04Kh19N9T) single-layer deposition of beads on steel (a), and microstructure of metal in FZ in deposition with electrodes ANV-17 (b) ( $\times 240$ ) and wire Sv-04Kh19N9T (c) ( $\times 400$ )

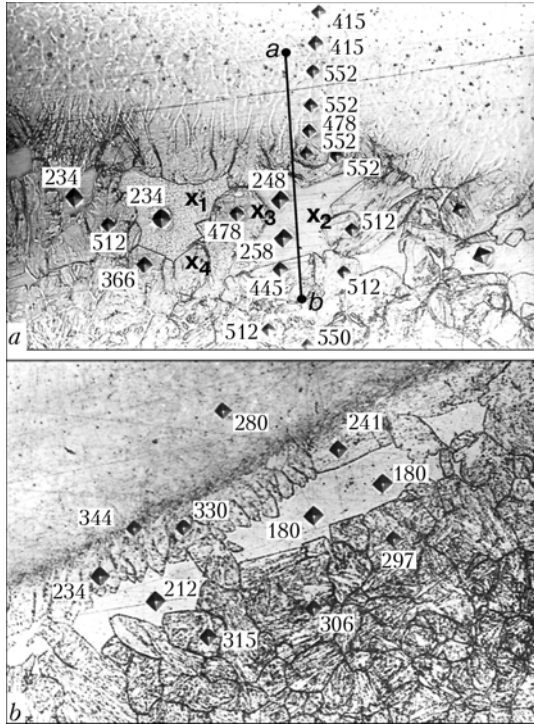


**Figure 5.** Microhardness of structural components in FZ in deposition of bead on martensite steel with 9 % Cr using wire Sv-04Kh19N9T after welding (a) and tempering (b) ( $\times 400$ )

position of thermal flows, which move away from the weld normal to the surface of its interface with BM (are shown by arrows), enables more efficient heating of areas adjacent to the near-weld zone. As a result both HAZ and FZ acquire in this zone maximum width (in the form of a dull strip around the weld, in which phase re-solidification took place) [1]. Under the area of narrow and deep penetration HAZ and FZ have minimum width because of rapid heat dissipation.

**Dissimilar martensite-austenite combination (M-A).** Metal structures in FZ area in case of using consumables,  $T_L-T_S$  values of which are lower than those of BM, are considered on examples of combinations of martensite steel (R91) and austenite consumables with the following types of alloying: Fe-Cr-Ni (wire Sv-04Kh19N9T), Fe-Cr-Ni-Mo-Mn (electrodes ANV-17) (Figures 4-6), and Ni-Cu (electrodes MNCh-2) (Figure 7).

Values of solidification range temperatures of beads being deposited, depending upon the share of BM (~ 50 % in automatic deposition using wire of the type 18-10, and ~ 23 % in deposition using electrodes ANV-17), shift to the area of higher temperatures in comparison with the deposited filler material (Figure 4, a). In contrast to the M-M combination, coarse-crystalline structure in FZ of the weld metal and BM is not formed. Clear transition from BM with martensite structure to lighter cast austenite-martensite structure of the weld is observed. Near the pool walls, mainly in peripheral parts of the weld cross-section, structure of the weld has areas with clearly pronounced heterogeneity, because of incomplete mixing of the deposited and delaminated BM. In zone of

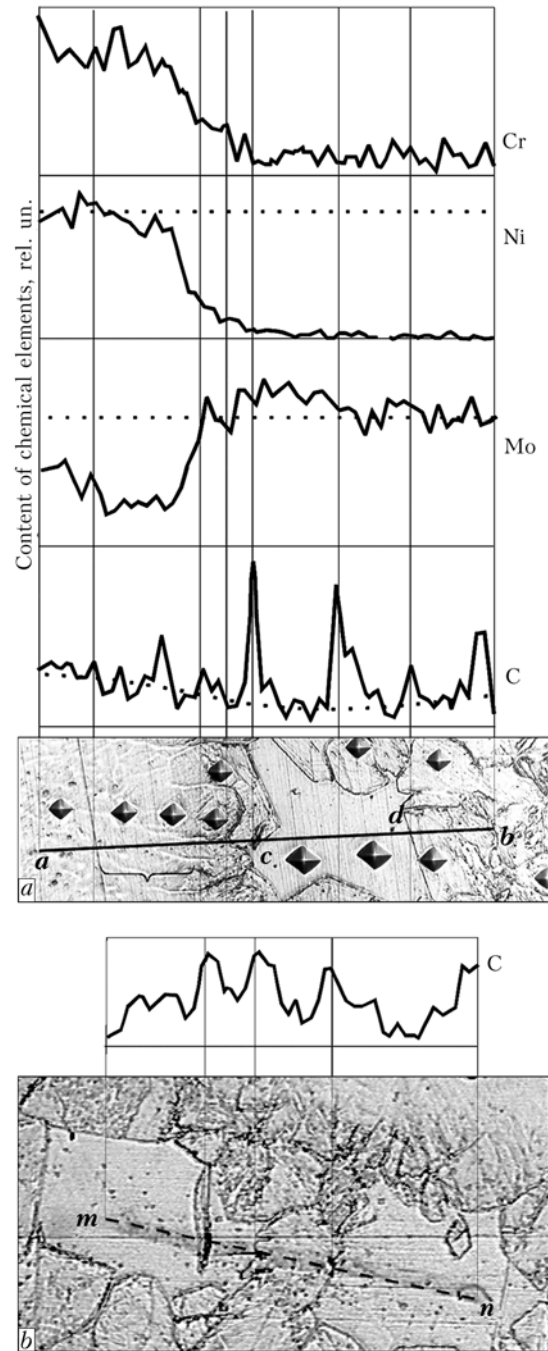


**Figure 6.** Distribution of Cr, Ni, Mo and C in FZ in the area a-b (see Figure 5) in deposition of bead on steel R91 using wire Sv-04Kh19N9T (a), and distribution of carbon between two light grains (fragment of structure in Figure 4, c) in the area m-n parallel to boundary of BM with the weld (b)

active spot of the arc column bottom of the pool is smoother and structure is more homogeneous.

Frequently in such dissimilar combinations in BM form rows of light, presumably  $\delta$ -ferrite, grains parallel to the boundary of the weld (Figures 4, b, c, and 5). Comparison of distribution of main alloying elements (Cr, Ni, Mo) with microstructure in the area of transition from BM to the weld shows (Figure 6, a) that boundary of the weld passes rather close to the areas of «white» phase. Taking into account peculiarities of the microstructure, one may draw conclusion that in the process of the joint formation a



thin interlayer, consisting from incompletely molten fragments of BM grains, could exist, from which started solidification of the zone of variable composition with fine-cell primary structure.

«White» phase differs from the surrounding martensite by rather low hardness (see Figure 5, a), which proves absence of propensity of this zone to hardening. Mean value of the martensite microhardness in the near-weld zone is  $HV\ 0.2-527$ , light grains  $HV\ 0.2-243$ , austenite-martensite weld (in center of the weld)  $HV\ 0.2-488$ . After tempering, microhardness of light grains remains close to the initial one ( $HV\ 0.2-180-212$ ), while microhardness of martensite (mean value) reduces to  $HV\ 0.2-290$ ; microhardness of the weld metal in its central parts also reduces to  $HV\ 0.2-209-220$ . For comparison with initial structure of the joint of M-A type after welding (Figure 5, a), in Figure 5, b the same type joint is shown after tempering (760 °C, 1 h) with indication of the values of the weld metal microhardness near the pool wall and phase components in the near-weld zone.

As far as content of alloying elements in considered light  $\delta$ -ferrite grains almost does not differ from that of the surrounding martensite steel (Table 3), the main reason of their formation should be considered depletion of carbon in these microareas because of its migration into the weld and in the area of the molten grain boundaries. So, resultant distribution of carbon between FZ metal and the weld (Figure 6, a) shows that a certain decrease of its mean basic content is observed in the weld (dotted line). Peak values of carbon accumulations are observed on interfaces  $\delta$ -ferrite-martensite (in the area of points c and d) and in the area of grain boundaries, which have a darker contrast. Peak value of carbon content in center of  $\delta$ -ferrite grain is, evidently, connected with its microinhomogeneity. Distribution of carbon in the area of the near-weld zone  $m-n$  in Figure 6, b also shows its

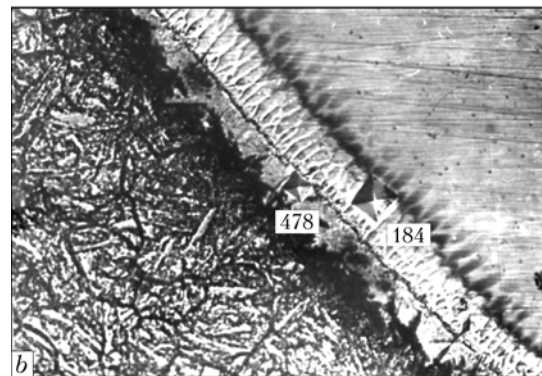
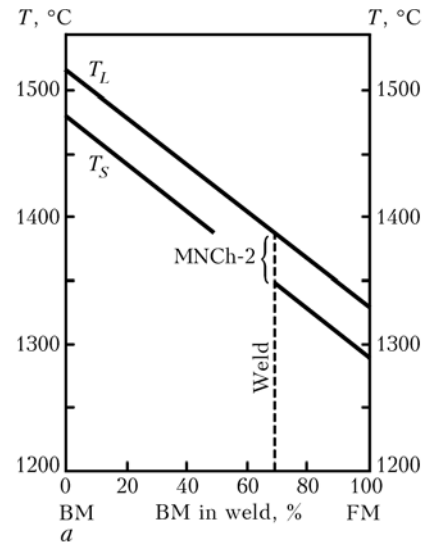


**Figure 7.** Schematic presentation of  $T_L-T_S$  range for BM (steel R91), metal deposited with electrodes MNCh-2 (Ni-Cu system) and metal of bead deposited on steel in dissimilar joint of M-A type (a), and microstructure of metal in FZ (b) ( $\times 1000$ )

peak values near phase interface, whereby certain trend towards reduction of its basic level in the area of  $\delta$ -ferrite grains is observed. Absence in  $\delta$ -ferrite grains of dispersed precipitates after tempering is one

**Table 3.** Results of electron probe analysis in FZ in deposition of beads on steel R91 using austenite consumables (without heat treatment)

Object of analysis*	Mass share of elements, %						
	Si	Cr	Mo	Nb	Ni	Mn	Ti
Martensite phase (point 3) (point 4)	Submerged arc deposition using wire Sv-04Kh19N9T**						
	0.603	10.158	1.308	0.020	0.21	0.080	0.050
	0.578	10.249	1.203	0.085	0.12	0.094	0.002
	Deposition using electrodes ANV-17***						
	0.582	10.293	1.258	0.026	0.844	0.232	0.005
Light $\delta$ -ferrite grain (point 2) (point 1)	Submerged arc deposition using wire Sv-04Kh19N9T**						
	0.556	10.010	1.198	0.271	0.367	0.138	0
	0.622	10.206	1.427	0.369	0.126	0.024	0
	Deposition using electrodes ANV-17***						
	0.505	10.344	1.211	0	0.360	0.140	0.005

\* --- point numbers in brackets correspond to indexes near cross-lines in Figure 5, a, which designate places of EPMA. \*\* --- deposition on steel: 0.1C-0.34Si-0.47Mn-0.003S-0.018P-8.5Cr-0.28Ni-0.93Mo-0.2V-0.072Nb-0.06N. \*\*\* --- deposition on steel: 0.085C-0.33Si-0.43Mn-0.015S-0.013P-8.85Cr-0.12Ni-1Mo-0.25V-0.069Nb (N was not determined).



more evidence of their decarburization (see Figure 5, b).

It is possible to assume that release of carbon from BM micro-areas into the weld may proceed as follows: 1) directly through the boundary of the contact BM-melt, if it has originated, by means of diffusion in solid solution and segregation through the phase interface; 2) through liquid channels, which are formed as a result of inter-grain melting and partial melting of the grains themselves, through which communicate micro-areas of BM that release carbon, and the weld melt. Increased microhardness of the weld near the pool after heat treatment is, evidently, connected with release of carbon into this zone.

When filler metal (Cu-Ni system) with even lower solidification range temperatures is used (Figure 7), metal of the near-weld zone has not hetero-phase nature associated with formation of  $\delta$ -ferrite. In this case it may be connected not only with thermal-physical properties of the deposited metal and degree of the near-weld zone overheating, but also with influence of its alloying on thermodynamic activity of carbon and its redistribution in FZ. As it is known, when less alloyed steels are welded using consumables with higher content of chromium and strong carbide-forming elements, carbon migration into the weld increases [6, 7]. Application of Ni-base welding consumables enables higher «retention» of carbon in BM.

Character of distribution of alloying elements, shown in Figure 6, a and Figure 8, proves that in all considered cases, when austenite consumables in welding (deposition) of martensite steel were used, grains of variable composition originated at once near the interface BM-weld. Pure molten BM, which would not mix up with deposited metal, in considered com-

binations of martensite steel with austenite materials having lower solidification temperatures, was not detected in these cases.

As it was noted, in welding of martensite steel using austenite materials of types Sv-04Kh19N9T and Sv-01Kh19N18G19AM4 metal of the transition area has austenite-martensite structure with high microhardness (see Figure 5, a). In case of using high-nickel alloy, martensite is not formed in the transition area. Near interface drastic transition occurs from martensite BM to softer austenite metal of the weld (see Figure 7, b). Microhardness of BM near boundary with the weld is  $HV\ 0.2-478-600$ , while that of the metal, located nearby the weld, is  $HV\ 0.2-162-248$ .

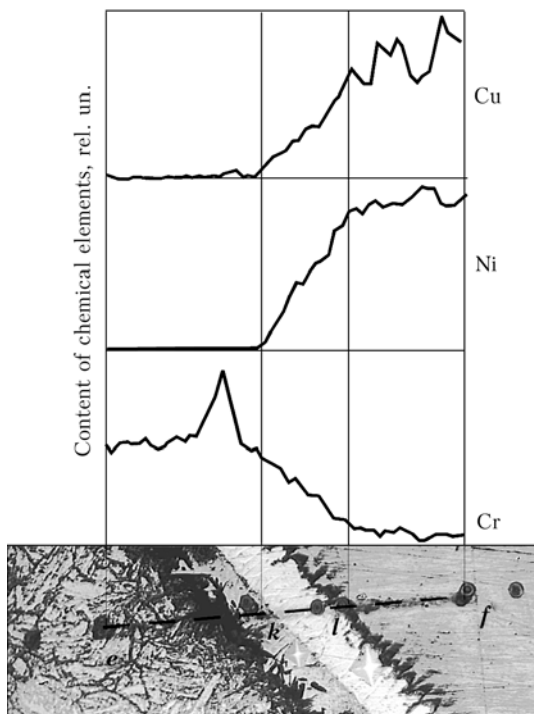
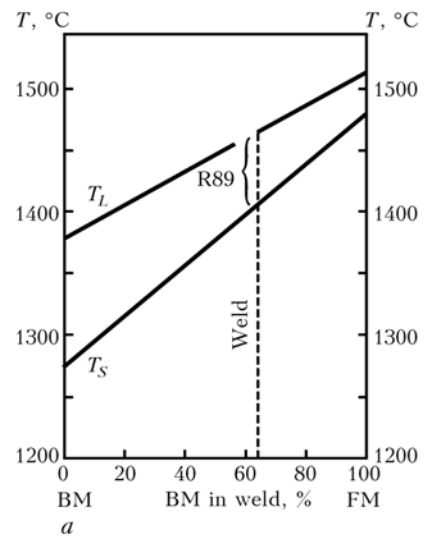


Figure 8. Qualitative distribution of alloying elements across FZ in the combination 9 % Cr martensite steel-Cu-Ni weld

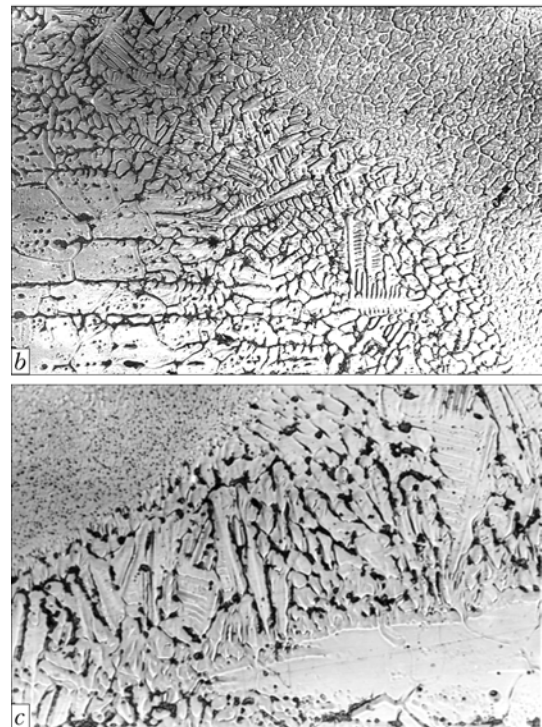


Figure 9. Schematic presentation of  $T_L-T_S$  range for steel EP794, metal deposited with electrodes R89 and metal of butt joint (a), microstructure in FZ (b) ( $\times 200$ ), and microstructure in FZ of bead deposited with electrodes KTI-9A with 12 % Cr (c) ( $\times 320$ )



So, in case of using welding consumables, which ensure lower than in the welded steel temperatures of the weld metal solidification, non-mixed zone practically does not form. However, one has to expect that at the values of the weld solidification temperature range, which partially exceed near- $T_S$  temperature range of the welded steel, development of melting along grain boundaries in the near-weld zone or maintenance of the degree of inter-grain melting, which occurred in primary heating of the metal by a welding arc, is possible.

**Dissimilar austenite-martensite combination (A-M).** In welding and deposition of steel using consumables, which ensure higher values of  $T_L-T_S$  temperatures of the weld than those of the steel, sufficient conditions are created for formation of a non-mixed zone. This statement is confirmed by the experiment, in which austenite steel 02Kh8N22S6 as BM and welding consumables (electrodes R89 and KTI-9A) were used, which ensured martensite deposited metal with higher values of solidification range temperatures than in BM (Figure 9, a). In welding of butt joints using electrodes R89 and deposition of a bead on surface of steel using electrodes KTI-9A, in FZ always formed a layer of cast metal with cellular and cellular-dendrite structures (Figure 9, b, c). Such structure with formed in inter-axial areas fusible, Si- and Ni-enriched phase is characteristic of the weld metal (and molten BM) of the type 02Kh8N22S6 [8].

In conclusion it should be noted that in this work the statement was confirmed on possibility of melting BM grains at the boundary with the weld by the heat released by the pool melt during its cooling and solidification. Trend toward formation of interlayers of

liquid BM (non-mixed zone) during solidification of the weld increases by means of the temperature values of the weld solidification range  $T_L-T_S$  increase in comparison with the welded steel. In case of equality of the values  $T_L-T_S$  of the weld and the steel, degree of melting of grains in FZ depends upon their preheating up to sub-solidus temperatures and conditions of heat withdrawal. At somewhat lower  $T_L-T_S$  values than those of the welded steel, complete melting of the BM grains was not detected, although possibility of inter-grain melting development was not excluded.

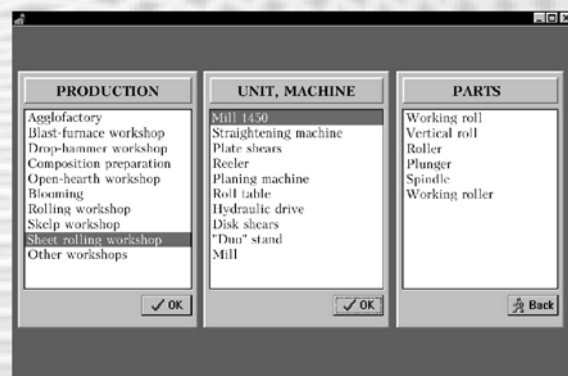
In welding of martensite high-chromium steel, using austenite materials with high content of chromium and active carbide-forming elements, in FZ certain areas form grains of  $\delta$ -ferrite as a result of carbon redistribution in it. In case of using Ni-base filler wire, formation of residual (stable up to room temperature)  $\delta$ -ferrite in FZ does not take place because of the change of the carbon redistribution character.

1. Skulsky, V.Yu. (2005) Metal structure in the fusion zone and HAZ of welded joints on high-chromium heat-resistant steels. *The Paton Welding J.*, **5**, 10-18.
2. Savage, W.F., Nippes, E.F., Szekeres, E.S. (1976) A study of weld interface phenomena in a low alloy steel. *Welding J.*, **9**, 260-268.
3. Beashlack, W.A. III, Lippold, J.C., Savage, W.F. (1979) Unmixed zone formation in austenitic stainless steel weldments. *Ibid.*, **6**, 104-312.
4. Gulyaev, A.P. (1956) *Metals science*. Moscow: Oborongiz.
5. Makarov, E.L. (1981) *Cold cracks in welding*. Moscow: Mashinostroenie.
6. Gotalsky, Yu.N. (1981) *Welding of dissimilar steels*. Kiev: Tekhnika.
7. Livshits, L.S. (1979) *Metals science for welders*. Moscow: Mashinostroenie.
8. Lipodaev, V.N., Yushchenko, K.A., Skulsky, V.Yu. et al. (1985) Properties of welded joints of corrosion-resistant steel 02Kh8N22S6. *Avtomatich. Svarka*, **4**, 41-44.

## COMPUTER SYSTEM TO DESIGN TECHNOLOGIES FOR REPAIR AND HARDENING OF METALLURGICAL EQUIPMENT PARTS

**Purpose.** The system is intended to design technologies for repair and hardening of metallurgical equipment parts by the electric arc surfacing methods. The computer system is based on the experience accumulated by 16 metallurgical plants in the field of surfacing. It allows design of a surfacing technology for 350 different parts (selection of surfacing consumables, methods, conditions, equipment, etc.) at a level of a highly skilled specialist. The system operation result has the form of a process sheet.

**Application.** The system can be used at metallurgical enterprises. It is intended for welding technologists working at a plant engineering department.



Selection of a part to be surfaced

Contacts: Prof. Makhnenko V.I.  
E-mail: d34@paton.kiev.ua



# EFFECT OF SCANDIUM ADDITIONS ON STRUCTURE-PHASE CONDITION OF WELD METAL PRODUCED BY WELDING ALUMINIUM ALLOY 1460

L.I. MARKASHOVA, G.M. GRIGORENKO, A.Ya. ISHCHENKO, A.V. LOZOVSKAYA, O.S. KUSHNARYOVA,  
T.A. ALEKSEENKO and A.A. CHAJKA  
E.O.Paton Electric Welding Institute, NASU, Kiev, Ukraine

Microstructure, element and phase compositions of weld metal of the joints produced by arc welding on alloy 1460 using filler wires Sv1201 and Sv1201 + Sc were studied. Main mechanisms of the effect of scandium on structure formation, chemical heterogeneity and mechanical properties of the weld metal were revealed. It is shown that scandium addition leads to grain refining, extra saturation of solid solution with scandium, formation of dispersed particles in the bulk of grains and complex-composition eutectic. The weld metal in this case has an increased strength.

*Keywords:* argon arc welding, aluminium alloy, scandium-containing filler wire, structure, phase components, solid solution, chemical heterogeneity, intermetallics, hardness

New class of Al-Li alloys widely applied nowadays is characterised by a combination of high mechanical properties (increased specific strength, rigidity at low density and high elasticity modulus), workability at cryogenic and increased temperatures and possibility of fabrication of welded structures [1-3].

A number of important characteristics of alloys (crack resistance, fracture toughness, resistance to cyclic loading) may dramatically change in the process of fabrication of structures and their operation. This seems to be associated with structure-phase transformations occurring during different heating processes [4, 5].

Apparently, in welding of Al-Li alloys the structural state of the materials being joined may markedly change under the effect of technological parameters of welding, which in many respects is determined by non-equilibrium solidification conditions having a substantial impact on the processes of structure-phase transformations of the weld metal. Besides, aluminium alloys doped with lithium are known to be the ageing materials, which are characterised, as a rule, by complex phase and structure transformations occurring during their heat treatment [6-10].

As shown by preliminary investigations, peculiarities of the structure-phase condition (chemical and structural heterogeneity, phase composition) of the weld and HAZ metal determine in many respects technological and structural strength of a welded joint. Strength and hardness of the base metal of alloy 1460 in the state after comprehensive heat treatment are very high, whereas strength of the welded joints on this alloy, produced by using a commercial filler wire of the Sv1201 grade, is about 50 % of that of the base metal.

In this connection, it seems expedient to study the efficiency of impact by scandium additions on forma-

tion of crystalline structure, chemical heterogeneity and phase composition of the weld metal in non-consumable electrode argon arc (TIG) welding of alloy 1460 (Al-3 % Cu-2 % Li-0.08 % Sc), as well as estimate variations in structure-phase condition of the weld metal in ageing. It is of interest to study the impact on the character of deformation of the weld metal by its structure under the effect of external loading, i.e. the impact by structure and different phase formations on the processes of accumulation of internal stresses and their relaxation. It is particularly important to estimate the impact by a contribution of different structural parameters (size of grain and sub-grain structure, dislocation density, morphology and distribution of phase precipitates, etc.) on mechanical properties of the welded joints ( $\sigma_{0.2}$  and  $\sigma_t$ ). Results of these studies will be reported in a series of publications.

**Materials and investigation procedures.** Single-pass welds in welded joints produced on alloy 1460 4 mm thick using standard filler wire Sv1201 (Al-6.5 % Cu-0.25 % Zr-0.3 % Mn) and experimental wire of the 1201 type (Al-6.5 % Cu-0.25 % Zr-0.3 % Mn) with an addition of 0.5 % Sc were used as investigation materials. The joints were investigated in the as-welded condition and after heat treatment providing a different degree of decomposition of solid solution with precipitation of hardening particles of main alloying elements and Al-Sc phases. This allowed evaluation of the state of solid solution formed during welding. The effect of precipitation hardening of the weld metal at low ageing temperature (150 °C) was caused by precipitation of the hardening particles of main alloying elements from solid solution, while that in high-temperature ageing (350 °C, 1 h) was caused by precipitation of the Al-Sc phases. If in both cases of heat treatment no hardening of the weld metal occurred, this would be indicative of the absence of formation of saturated solid solution of aluminium in the weld metal during the solidification process, or



its decomposition in cooling of a welded joint; and vice versa, hardening of metal compared with the as-welded state should be directly associated with decomposition of solid solution formed in solidification of cast metal during welding.

General mechanisms of formation of structure of the weld metal depending upon the type of filler wire were revealed by metallography. The state of the weld metal immediately after welding and after different postweld heat treatments, i.e. in a state after solid solution and precipitation hardening, was evaluated by measuring hardness. The content of elements in solid solution and individual phase precipitates was studied by the method of analytical scanning electron microscopy using the Philips unit SEM-500.

Series of comparative investigations of the welds made by using filler wires with and without scandium at the same level of main alloying elements allowed evaluation of the effect of scandium on the state of solid solution, structure, phase composition, chemical heterogeneity and mechanical properties of the weld metal in the as-welded condition.

**Investigation results.** As found by optical metallography and scanning electron microscopy, the welds made on alloy 1460 using filler wire Sv1201 have a dendritic structure. Individual coarse and long crystals are seen in the central part of the welds. As a rule, in welding of aluminium and low aluminium alloys, crystals in the welds grow from partially melted grains of the base metal, and direction of their growth coincides with direction of heat removal, i.e. crystallisation is of an epitaxial character. In welding of Al-Li alloys, such as 1460, an interlayer with a subdendritic structure is formed near the fusion line, whereas the major part of the weld has a dendritic structure. Adding scandium to welding wire Sv1201 leads to refining of structure and formation of a subdendritic or mixed dendritic-subdendritic structure.

Application of filler wire of the Sv1201 type, containing 0.5 % Sc, makes it possible to raise strength of the weld metal from 250 to 280 MPa (Figure 1). As shown by the measurement results, hardness of the weld metal in the as-welded condition in the case of wire Sv1201 + Sc is 5 units higher than that of the welds made with a similar wire containing no scandium. And this difference persists after artificial ageing (150 °C, 22 h). A substantial difference in hardness (approximately *HRB* 20) is seen after annealing at 350 °C for 1 h. Hardness of the weld metal produced by welding with filler wire Sv1201 is at a level of *HRB* 71, while that of the weld made with wire Sv1201 + Sc is far higher (*HRB* 90) (Figure 2).

The above relationships of hardness of the base and weld metals after heat treatment under different conditions allow a conclusion that TIG welding leads to formation of complex solid solution of copper and lithium in aluminium, or copper, lithium and scandium in aluminium, when welding is performed with wire Sv1201 or Sv1201 + Sc, respectively.

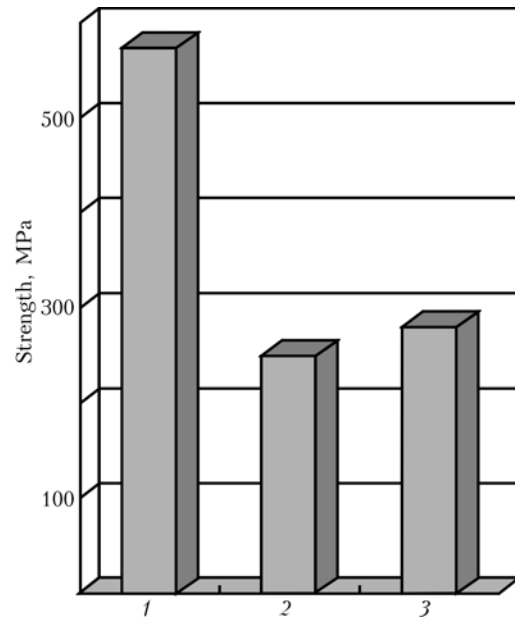


**Figure 1.** Strength of base metal (1) and welds made on alloy 1460 by TIG welding using filler wires Sv1201 (2) and 1201 + 0.5 % Sc (3)

Increase in hardness of the weld metal in the case of using filler wire Sv1201 + Sc seems to be an indirect indication of complex processes associated with formation of solid solution of scandium in aluminium, that occur in solidification of the weld metal and its decomposition to precipitate particles of the type of  $Al_3Sc$ .

Moreover, a change in hardness of the weld metal after annealing at 350 °C for 1 h must be related to differences in character of the phase formation processes when using different alloying systems, as it is a known fact that heat treatment of this type of the materials can either stimulate or hinder a simultaneous occurrence of the opposite processes, i.e. precipitation and coagulation of the hardening particles of main alloying elements (causing weakening), and precipi-

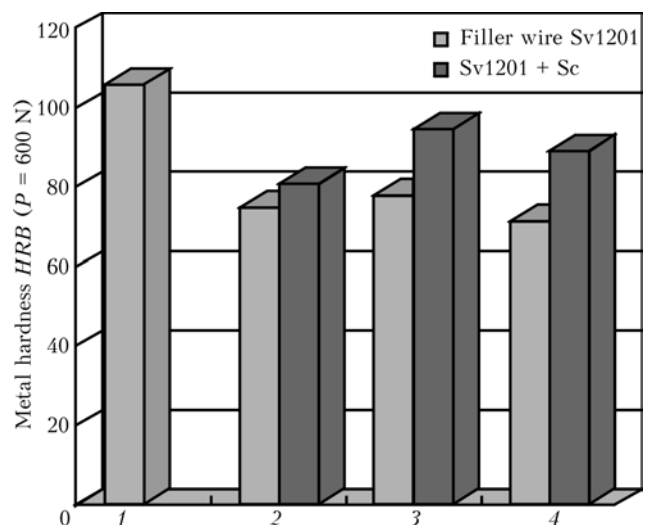


**Figure 2.** Hardness of alloy 1460 (1) and weld metal on this alloy (2-4): 1 — after quenching + artificial ageing; 2 — as-welded; 3 — after welding and artificial ageing (150 °C, 22 h); 4 — after welding and high-temperature ageing (350 °C, 1 h)

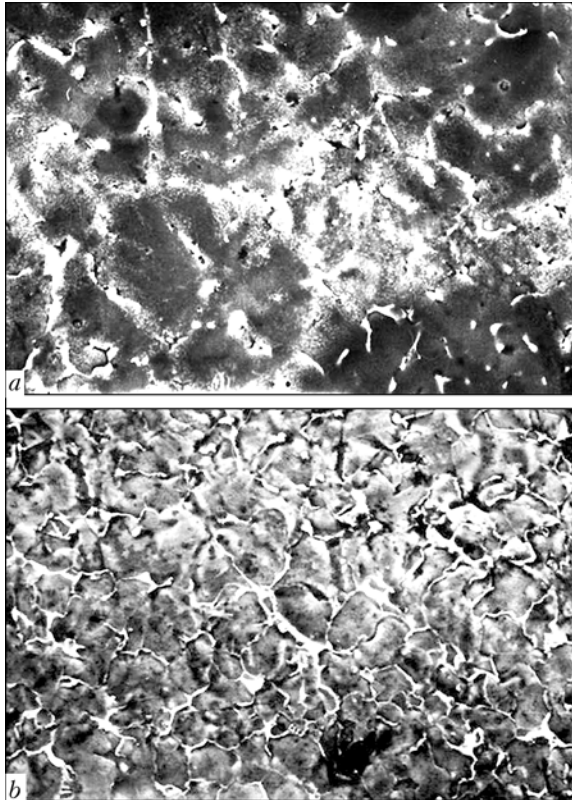


**Figure 3.** Microstructure of weld metal produced by TIG welding on alloy 1460 using filler wires Sv1201 (a) and Sv1201 + 0.5 % Sc (b) ( $\times 600$ )

tation of the Al-Sc phase particles (causing hardening).

More comprehensive studies of peculiarities of the effect of scandium on chemical and phase heterogeneity, and on formation of structure of the weld metal on alloy 1460 were conducted using analytical scanning electron microscopy. Tables 1 and 2 give results of the completed stage of investigations.

In the case of welding using filler wire Sv1201 (without scandium), the weld metal has a structure with cast grain  $D_g \approx 10\text{--}30\ \mu\text{m}$  in size and one type of eutectic (type I) along the grain boundaries (GB), containing approximately 20–30 % Cu (Figure 3, a; Table 1). The eutectic precipitates are 1–4  $\mu\text{m}$  thick.

The concentration of alloying elements in aluminium solid solution was estimated by the results of analysis of metal at the centre of grains having different sizes and configurations. Variations of the concentration within one grain were estimated on the basis of multipoint analysis in the bulk of grain. According to the analysis results, the content of copper in the central zone of grains is 1.6–2.0 %, while near the grain boundaries the concentration of copper grows to 4.0–4.5 %. Dispersed phases with particle size of  $d_p \approx 0.2\text{--}0.8\ \mu\text{m}$  and distance between the particles of  $l_p \approx 0.4\text{--}1.7\ \mu\text{m}$ , were detected in some regions inside the grains.

After heat treatment (heating to 350 °C, 1 h), the concentration of copper in the bulk of grain increases to about 4.7 %, while that at GB grows to 7 % at 0.5–1.0 % Zr. Phases  $d_p \approx 2\ \mu\text{m}$  in size, containing

about 14–18 % Cu and 0.01 % Zr, can be seen in the bulk of grains. Thickness of the eutectic precipitates (15–20 % Cu) decreases almost twice (to 1–2  $\mu\text{m}$ ).

In the weld metal produced with filler wire Sv1201 + Sc the grain size decreases to 5–12  $\mu\text{m}$  (i.e. by a factor of 2), compared with the weld metal without scandium (Figure 3, b). As seen from Figure 4 and Table 3, the copper content of solid solution varies from 2.3 % at the grain centre to 3.5–5.0 % near the grain boundaries.

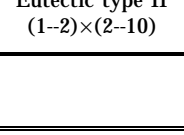
Element analysis in the bulk of other grains at the absence of dispersed inclusions shows that the copper content varies from 1.8–2.4 to 3.0 % at the centre and 3.5–4.5 % at the grain boundary. The content of transition elements varies from 0.1–0.4 to 1.0 % for Zr, and from 0.06–0.2 to 0.3 % for Sc. Isolated grains with 0.8 % Sc were revealed at its concentration in solid solution equal to 0.19–0.22 %. The degree of saturation of solid solution with alloying elements hardly depends upon the grain size. For example, grains of an identical size ( $D_g = 5\ \mu\text{m}$ ) have different chemical composition: in one of them the concentration of copper amounts to 2.5 % and that of scandium — to 0.8 %, while the other contains 3.2 % Cu and 0.2 % Sc. At the same time, a coarser grain (Figure 5) contains the same amount of copper and scandium as one of the grains 5  $\mu\text{m}$  in size (3.1 % Cu, 0.2 % Sc). The welds produced by using filler wires Sv1201 and Sv1201 + Sc (Figure 6) share a minimum copper content in the central region of grains and an increased copper content near the grain boundaries.

Variation of the scandium and zirconium concentrations is of a discrete heterogeneous character, and even within one grain there are regions with a local high level of these elements (Figure 6). A similar (discrete) distribution is characteristic also of zirconium, the concentration of which in isolated points is about 3 % (see Tables 1 and 2). Grain-boundary eutectics with a wide range of the concentration of copper (10.0–28.7 %) are formed in the case of scandium additions. An increased copper content (12–34 %) at a relatively low zirconium level (0.8 %) and low amount of scandium (0.02–0.30 %) is detected in some regions of the eutectic interlayers. At the same time, other eutectic formations are characterised to a greater extent by a decreased copper content (9–11 %) and increased scandium content (up to 0.6 %). The eutectic precipitates are 1–3  $\mu\text{m}$  thick (see Tables 1 and 2).

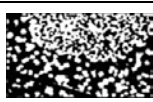
Dispersed phases less than 1  $\mu\text{m}$  in size (0.08–0.80  $\mu\text{m}$ ) are present in the bulk of grains, the distance between the particles being 0.1–0.7  $\mu\text{m}$ . The scandium content of these particles varies from 0.13 to 0.8 %, and copper content varies from 2.1 to 4.0 %. Also revealed were the isolated coarser intermetallic inclusions (Figure 7). Analysis of inclusions of Sc-containing primary intermetallics shows that they are much differing in composition (although having a similar shape and size, i.e. 6–8 $\times$ 8  $\mu\text{m}$ ). They are mostly the Al-Sc (11–13 % Sc) and Al-Cu-Sc phases formed on the base of solid solution Al-Cu (5.8 % Cu). More-



**Table 1.** Results of investigation of welds made on alloy 1460 by TIG welding using filler wires Sv1201 and Sv1201 + Sc in the as-welded condition<sup>1</sup>

Chemical composition <sup>2</sup> , wt. %		Test region	GB interlayers	
Weld metal	Filler wire		Schematic, morphology and size of precipitates, μm	Chemical composition, wt. %
Alloy 1460 (3.5–4.7Cu; ~1.0Li; Fe and Si impurities; 94.3–94.5Al)	Sv1201 (6.5Cu, 0.25Zr, 0.3Mn, 92.95Al)	Weld centre	 Eutectic type I (3×2)–12	Eutectic type I Al–(21–30)Cu
		Base metal	 Eutectic type I (1–4)×(2–15)	Eutectic type I Al–(20–30)Cu
Alloy 1460 + Sc (3.5–4.7Cu; ~1.0Li; Fe and Si impurities; 0.25–0.3Sc, 94.0– 94.25Al)	Sv1201 + Sc (6.5Cu, 0.25Zr, 0.3Mn, 0.5Sc, 92.45Al)	Weld centre	 Eutectic type II (2–5)×(2–6)	Eutectic type I Al–(12.3–34)Cu–(0–0.8)Zr– (0.02–0.3)Sc  Eutectic type II Al–(9–11)Cu–(0.2–0.6)Sc
		Base metal	 Eutectic type I (1–5)×(5–15)   Eutectic type II (1–2)×(2–10)	Eutectic type I Al–22Cu–0.1Sc  Eutectic type II Al–(2.5–8.7)Cu–(0–0.1)Zr– (0.14–0.16)Sc

**Table 1 (cont.)**

Grain					
Chemical composition of coarse phase inclusions, wt. %, and size, μm	Grain size, μm	Chemical composition, wt. %		Dispersed phases in grain bulk	
		At grain centre	At grain boundary	Size of inclusions, μm	Chemical composition, wt. %
Not detected	10–30	Al–(1.6–2)Cu	Not detected	$d_p \sim 0.2–0.8$ $l_p \sim 0.4–1.7$	Not detected
Same	10–30	Al–(1.8–2)Cu	Same	Not detected	Same
Al–(1.4–6)Cu–(5–13)Sc (8×8)	5–12	Al–(1.2–3)Cu– (0.1–0.4)Zr– (0.06–0.2)Sc	Al–(2–4.5)Cu– (0–1)Zr–(0.14–0.3)Sc	$d_p \sim 0.08–0.8$ $l_p \sim 0.1–0.7$	 Al–(2.1–4)Cu– (0.3–0.8)Sc
Al–(0.01–1.3)Cu– (1.3–3.2)Zr–(11–15)Sc– (1.4–4)Si (6–8×8)					
Not detected	10–20 (10×20)	Al–(2.1–2.8)Cu– (0–0.4)Zr–(0.12–0.3)Sc	Al–(3.1–3.6)Cu– (0.1–0.7)Zr–(0.13–0.5)Sc	$d_p < 1$ $l_p < 1$	Al–2.07Cu–0.1Zr– 0.13Sc

Notes. 1. Here and in Table 2, the composition of particles was analysed at a particle size more than 1 μm; at a particle size below 1 μm a fragment of surface area about 20×30 μm with a larger quantity of particles was scanned. 2. According to spectral analysis data.



**Table 2.** Results of investigation of welds made on alloy 1460 by TIG welding using filler wires Sv1201 and Sv1201 + Sc after heat treatment (350 °C, 1 h)<sup>1</sup>

Chemical composition <sup>2</sup> , wt. %		Test region	GB interlayers	
Weld metal	Filler wire		Schematic, morphology and size of precipitates, μm	Chemical composition, wt. %
Alloy 1460 (3.5–4.7Cu; ~1.0Li; Fe and Si impurities; 94.3–94.5Al)	Sv1201 (6.5Cu, 0.25 Zr, 0.3Mn, 92.95Al)	Weld centre	Eutectic type I 1–(2×2)–6, (2×8)–12 	Eutectic type I (15–20)Cu–Zr
		Base metal	 Eutectic type I (1–3)×(2–7)	Eutectic type I (15–21)Cu–Zr
Alloy 1460 + Sc (3.5–4.7Cu; ~1.0 Li; Fe and Si impurities; 0.25–0.3Sc; 94.0–94.25Al)	Sv1201 + Sc (6.5Cu, 0.25Zr, 0.3Mn, 0.5Sc, 92.45Al)	Weld centre	Eutectic type I 2×(2–3), (0.5–1)×(5–10)  Eutectic type II (2–3)×(2–7)	Eutectic type I (17–21)Cu–(0–0.1)Zr– (0.03–0.08)Sc  Eutectic type II (4–8)Cu–(0.04–0.1)Zr– 0.04Sc
		Base metal	Eutectic types I and II (1–2)×(2–10) 	Eutectic type I (12–26)Cu–(0–0.35)Zr– (0.01–0.08)Sc  Eutectic type II (6.46–8)Cu–(0–0.35)Zr– (0.01–0.08)Sc

**Table 2 (cont.)**

Grain					
Chemical composition of coarse phase inclusions, wt. %, and size, μm	Grain size, μm	Chemical composition, wt. %		Dispersed phases in grain bulk	
		At grain centre	At grain boundary	Size of inclusions, μm	Chemical composition, wt. %
Not detected	10–30	(2.1–4.7)Cu–(0–0.18)Zr	(2.8–7)Cu–(0–0.48)Zr	$d_p \sim 2$	(14.5–18.3)Cu–(0–0.01)Zr
Not detected	10–30	(3.7–5.7)Cu–(0–0.2)Zr	(4.4–6.5)Cu–(0–0.96)Zr	Not detected	Not detected
(1.25–1.27)Cu–(5.55–14)Zr–(0.4–1.4)Sc ( $d_{inc} \sim 1 \times 2$ )	5–12	(2.5–6)Cu–(0–0.8)Zr–(0.02–0.08)Sc	(2.9–9.9)Cu–(0–0.6)Zr–(0.02–0.18)Sc	$d_p \sim 1$	(1.25–1.27)Cu–(5.55–14)Zr–(0.4–1.4)Sc
				$d_p \sim 1$	(16–21.5)Cu–(0–0.8)Zr–(0.01–0.035)Sc
(1.3–1.8)Cu–(11–23)Zr–(2.28–2.56)Sc (5–8×6–8)				$d_p < 1$ $l_p < 1$	(4.4–5.2)Cu–up to 0.5Zr–(0.03–0.07)Sc
Not detected	10–20 (10×20)	(1.5–5)Cu–(0–0.19)Zr–(0–0.18)Sc	(4.1–7)Cu–(0.14–1.07)Zr–(0.02–0.08)Sc	Not detected	Not detected

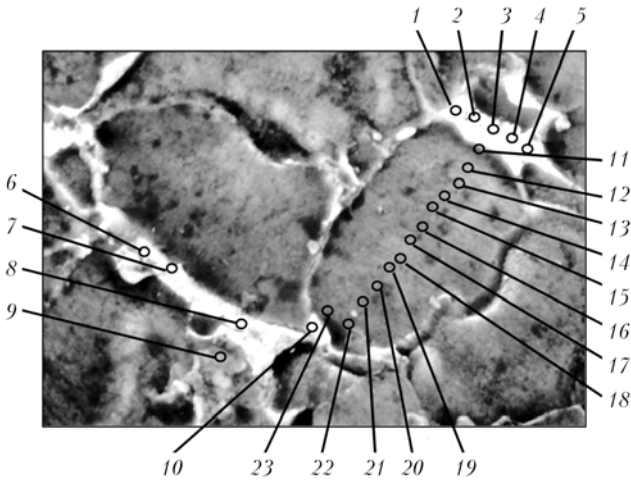


**Figure 4.** Microstructure of weld metal produced on alloy 1460 by TIG welding using filler wire Sv1201 + Sc, and analysis points (see Table 3) in the bulk of grains and at GB ( $\times 2400$ )

over, some of them have an increased silicon content (about 1.37–4.0 %).

In Sc-containing welded samples after heat treatment (350 °C, 1 h), grain size  $D_g$  in the weld does not change and amounts to 5–12  $\mu\text{m}$ . Element analysis in the bulk of grain shows an increased content of copper and zirconium (up to 6 % Cu and 0.8 % Zr, compared with their concentration in the weld metal in the as-welded condition), and decreased scandium content (from 0.06–0.20 to 0.02–0.08 %). The character and peculiarities of eutectic precipitates remain unchanged: type I --- with increased copper content (17–21 %), and type II --- with decreased copper content (4–8 %). The amount of scandium and zirconium in them is approximately the same: 0.03–0.08 % Sc and 0–0.1 % Zr. After heat treatment, eutectics along GB become thinner, their thickness being  $\delta_e \approx 0.3\text{--}3.0 \mu\text{m}$ .

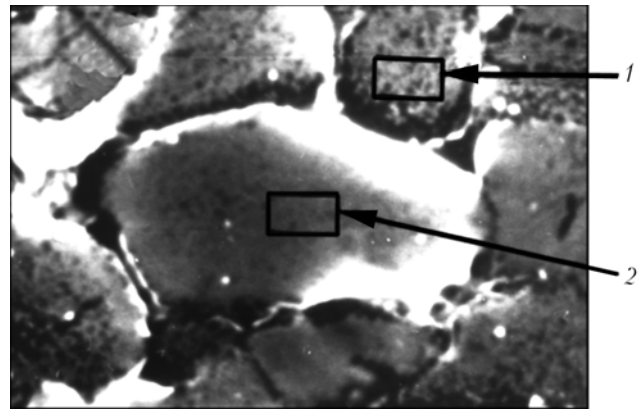


**Figure 5.** Microstructure of weld metal produced on alloy 1460 by TIG welding using filler wire Sv1201 + 0.5 % Sc in regions with different grain sizes: 1 ---  $D_g = 5 \mu\text{m}$ ; 2 ---  $D_g = 12 \mu\text{m}$  ( $\times 5000$ )

Three types of phase precipitates dominate in the internal volumes of grains: isolated coarser precipitates  $d_p \approx 1\text{--}2 \mu\text{m}$  in size with an increased zirconium content of the following composition, wt.%: 1.25–1.27 Cu, 0.4–1.4Sc, 5.55–14Zr; mean size precipitates ( $d_p \approx 1 \mu\text{m}$ ) with an increased copper content, having the following composition, wt.%: 16–21.5Cu, 0.01–0.035Sc, 0–0.8Zr; and fine phases with  $d_p < 1 \mu\text{m}$  and  $l_p$  less than 1  $\mu\text{m}$ . Element analysis of a grain fragment with dispersed phases showed the following content of chemical elements, wt.%: 4.4–5.2Cu, 0.03–0.07Sc and 0.5Zr. It should be noted that the scandium and zirconium containing phases of irregular geometry and coarse size 5–8 $\times$ 6–8  $\mu\text{m}$  (1.3–1.8 % Cu, 2.28–2.56 % Sc, 11–23 % Zr) hardly change in morphology.

Analysis of structural variations in metal of the welds, their chemical composition and phase formations of the grain-boundary and intragranular types allows the following conclusions. At the absence of scandium additions, the weld metal in the as-welded

**Table 3.** Content of chemical elements, wt.%, in the bulk of grains, in eutectic precipitates along GB at points acc. to Figure 4

Chemical element	1	2	3	4	5	6	7	8	9	10	11	12
Al	75.26	80.45	81.6	79.9	71.9	71.4	72.9	83.2	69.48	87.38	95.16	95.84
Cu	24.4	19.2	18.2	19.7	27.7	28.3	26.5	16.5	29.76	12.3	4.5	3.9
Sc	0.02	0.14	0.1	0.13	0.13	0.08	0.16	0.1	0.17	0.1	0.34	0.12
Fe	0.4	0.28	0.2	0.3	0.27	0.2	0.3	0.3	0.18	0.05	--	0.15
Zr	--	--	--	--	--	--	--	--	0.4	0.3	--	--
Si	--	--	--	--	--	--	--	--	--	--	--	--

**Table 3 (cont.)**

Chemical element	13	14	15	16	17	18	19	20	21	22	23
Al	96.51	96.82	97.3	97.49	97.6	97.2	97.41	97.1	97.2	96.9	96.1
Cu	3.3	2.7	20.45	2.35	2.3	2.35	2.3	2.4	2.7	2.9	3.5
Sc	0.2	0.18	0.15	0.17	0.18	0.2	0.2	0.3	0.2	0.18	0.19
Fe	--	--	--	--	--	0.06	0.1	--	--	0.1	0.2
Zr	--	0.3	0.2	--	--	0.2	--	--	--	--	--
Si	--	--	--	--	--	--	--	0.2	--	--	--

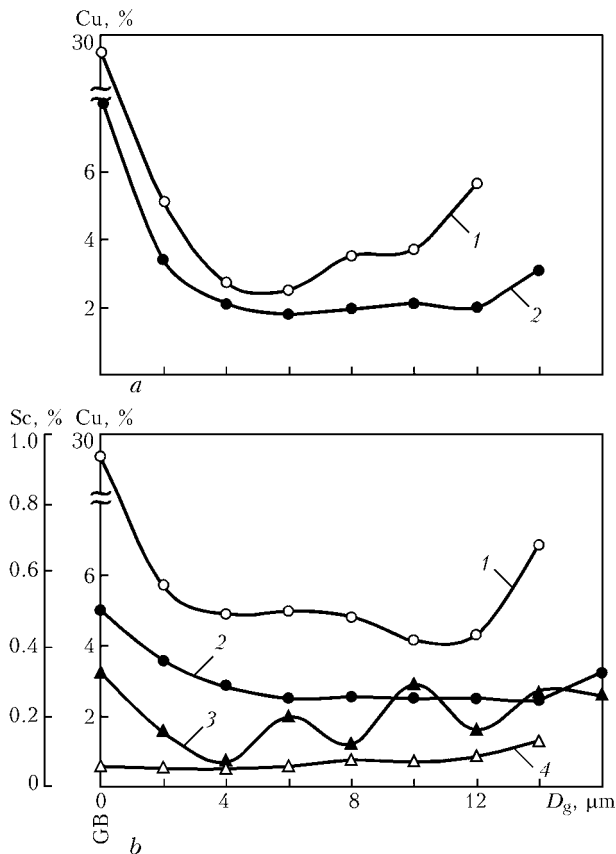


**Figure 6.** Variations of copper and scandium concentrations in transition from GB to the bulk of grains  $D_g$  of the weld metal after welding (2 and 3, respectively), and after additional heat treatment (1, 4): a — weld metal produced in welding with filler wire Sv1201; b — with filler wire Sv1201 + Sc

condition is characterised by rather coarse grains ( $D_g \approx 30 \mu\text{m}$ ), presence of the intragranular type of phase precipitates, having an increased copper content similar to that of eutectics, as well as grain-boundary eutectic precipitates with a copper content of about 20–30 %. Subsequent heat treatment at a temperature of 350 °C for 1 h does not cause a change in grain size. However, it leads to an approximately 2 times decrease in thickness of the eutectics and 25–30 % decrease in their copper content. At the same time, the copper content of the internal volumes of grains grows to some extent (approximately from 2.0 to 4.7 %). It can be assumed that both change in composition of matrix grains and formation of coarser intragranular phases are caused to a substantial degree by dissolution of the eutectics during the heat treatment process.

More complicated structure-phase transformations of the weld metal take place with adding scandium to the weld metal. Firstly, scandium additions lead to a substantial (more than twice, i.e. from 10–30  $\mu\text{m}$  without scandium to 5–12  $\mu\text{m}$  with scandium) grain refining in the weld metal after welding. More complex eutectic phases are formed, differing first of all in copper and scandium contents (from 10 to 30 % and from 0.02 to 0.6 %, respectively). Another characteristic feature is formation of intragranular-type phases, which differ in size (from less than a microme-

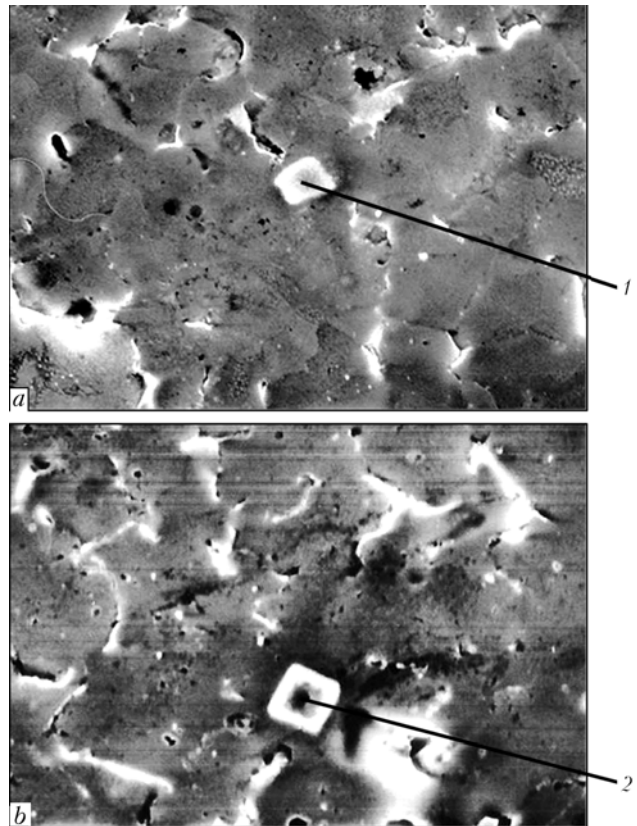


**Figure 7.** Microstructure of weld metal containing primary intermetallics in TIG welding of alloy 1460 using filler wire Sv1201 + Sc: a — intermetallic 1 (13 % Sc, 3 % Zr, 0.8 % Cu); b — intermetallic 2 (5 % Sc, 6 % Cu) ( $\times 1300$ )

tre to several micrometres) and contain an increased amount of scandium (from 5 to 15 %) and zirconium (3 %) at a not that high copper content (1–4 %). Subsequent heat treatment (like in the weld metal containing no scandium) does not lead to a change in grain size. However, it causes decrease in thickness and dispersion of grain-boundary eutectics, as well as increase in the amount of intragranular phase precipitates.

It should be noted that, although a substantial amount of phases are formed in the internal volumes of grains during heat treatment, the conventional optical metallography and scanning electron microscopy methods fail to reveal peculiarities of their internal structure and presence of finer phases ( $\leq 1 \mu\text{m}$ ), which can determine certain properties of the joints, including precipitation hardening.

It can be noted in conclusion that size of crystalline grains of the weld diminishes almost twice in the case of using filler wire Sv1201 + Sc, compared with the case where filler wire Sv1201 without scandium is used. The process of solidification of welds leads to formation of complex saturated solid solution of main alloying elements, i.e. copper and lithium, in the case of using filler wire Sv1201. With filler wire Sv1201 + Sc, the solid solution contains copper, lithium and scandium. In both cases the welds are susceptible to precipitation hardening during subsequent heat treatment. The content of scandium amounts to 0.2 %. In this case, isolated primary scandium intermetallics of



complex composition and regular geometry can be formed in the weld metal.

The copper content of solid solution (at the grain centre) varies within a wide range from 1.2 to 3.0 %, independently of the type of filler wire. With an addition of scandium into the weld metal, the solidification process leads to formation of dispersed particles less than 1  $\mu\text{m}$  in size, having a complex chemical composition, in the bulk of grains. Their scandium content varies from 0.13 to 0.8 %. The Al-Li and Al-Cu-Li base eutectics are formed along the cast grain boundaries in the weld metal, whereas with the scandium addition the eutectics change in morphology and have a more complex composition.

1. Fridlyander, I.N. (2000) Aluminium alloys in aircraft during the periods of 1970-1999 and 2000-2015. In: *Transact. of 5th Session of the Sci. Council on New Materials of the Int. Ass. of AS on Problems of Advanced Materials Science*. Kiev: Naukova Dumka.
2. Fridlyander, I.N. (1998) Aluminium alloys in aircraft engineering. In: *Transact. of 3rd Session of the Sci. Council on New Materials of the Int. Ass. of AS on Problems of Advanced Materials Science*. Kiev: Naukova Dumka.
3. Furukawa, M., Miura, Y., Nemoto, M. (1987) Temperature and strain rate dependencies of yield stress of an Al-Cu-Li-Mg-Zr alloy. *Transact. of Jap. Inst. Metals*, 28, 655-665.
4. Ryazantsev, V.I., Fedoseev, V.A. (1994) Mechanical properties of welded joints of Al-Cu system aluminium alloys. *Svarochn. Proizvodstvo*, 12, 4-7.
5. Ando, S., Ohkubo, M. (1992) Weldability of high strength aluminium alloy by electron beam welding. *J. Light Metal Welding and Construction*, 30(1), 12-18.
6. (1992) *Aluminium-lithium alloys. Structure and properties*. Ed. by I.N. Fridlyander et al. Kiev: Naukova Dumka.
7. Kajgorodova, L.I., Romanova, R.R., Drits, A.M. et al. (1992) Natural ageing of Al-Li-Cu-Zr system alloy. *Tekhnologiya Lyog. Splavov*, 1, 34-38.
8. O'Dowd, M.E., Ruch, W., Starke, E.A. (1987) Dependence of elastic modulus on microstructure in 2090-type alloys. *J. de Phys.*, 48(9), 565-576.
9. Ball, H.D., Lloyd, D.J. (1985) Particles apparently exhibiting fivefold symmetry in Al-Li-Cu alloys. *Sci. Met.*, 19, 1065-1068.
10. Gufnghui, M., Huasyun, Y., Delin, P. et al. (2000) Fraction and phase spacing of fibrous intermetallic  $\sigma$ -LiAl in hypoeutectic Al-Li alloys by unidirectional solidification. *Metallifizika. Nov. Tekhnologii*, 22(4), 58-61.

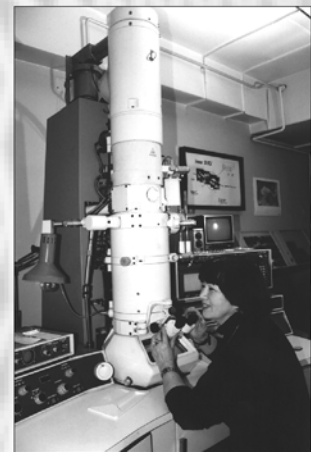
## PHYSICAL-CHEMICAL INHERITANCE OF MATERIALS

### Proposals for co-operation

- Qualitative and quantitative determination of the content of main alloying and impurity elements, including gases, in different materials – ores, concentrates, minerals, powders, slags, fluxes, cast irons, steels and alloys based on nickel, titanium, aluminium, copper, etc.
- Manufacture of microsections, detection and photography of microstructure, metallography of the quality and revealing of the nature of defects in metal products, fractography.
- Development of procedures, determination and identification of nitride, oxide and sulphide inclusions, examination of phase composition of intermetallics, carbides and other phases in different materials.
- Examination of structure and phase composition of materials by the light and electron microscopy methods: qualitative and high-temperature metallography, X-ray diffraction analysis and X-ray microanalysis.
- Development of procedures and investigation of some physical properties of metals, slags and coatings by the dilatometry, high-temperature thermal differential analysis and calorimetry methods, and investigation of interaction in gas-slag-metal systems in heating using different thermal energy sources.
- Training, probation, consultations of engineers and scientists in the above fields.

The Department is equipped with transmission electron microscope JEM-200CX (JEOL, Japan), scanning electron microscope JSM-840 with the Link analysis system (JEOL, Japan), photoelectric vacuum spectrometer DFS-51U, microprobe for X-ray microanalysis SX-50 (Cameca, France), optical emission spectrometer SPECTROVAC-1000 DV-4 (Baird, The Netherlands).

Contacts: Grigorenko G.M.  
E-mail: leco@carrier.kiev.ua



JEM-200CX



# PROCEDURE FOR DETERMINATION OF RESIDUAL STRESSES IN WELDED JOINTS AND STRUCTURAL ELEMENTS USING ELECTRON SPECKLE-INTERFEROMETRY

L.M. LOBANOV, V.A. PIVTORAK, V.V. SAVITSKY and G.I. TKACHUK  
E.O. Paton Electric Welding Institute, NASU, Kiev, Ukraine

A computer program is described for processing the interference fringe patterns in the area of a drilled blind hole, containing information on displacements caused by elastic stress relieving. Experimental and calculated values are given, which were obtained when solving the procedural problem of beam bending under the impact of the specified load. Calculated values were compared with experimental values, this allowing evaluation of the error of the suggested method of stress determination.

*Keywords:* welded structures, residual stresses, evaluation procedure, probing holes, electron speckle-shearography, elastic pre-tension

Residual stresses developing in structural elements in their fabrication are one of the main factors, allowing determination of the strength, reliability and fatigue life of products. In this connection, development and improvement of effective methods and means of studying the residual stresses is of practical interest.

There exist various methods of experimental determination of residual stresses in welded structures [1–5].

One of the most widely accepted methods is the probing hole technique [2], in which a through-thickness or blind hole is made in the studied point of the surface, and deformations caused by elastic unloading of the material bulk at residual stress releasing are measured in several directions. Deformations are measured using special strain gauge arrays glued-on in the vicinity of the drilled-out hole. Values of measured deformations are used to determine the principal directions and respective values of residual stresses applying different calculation or analytical models.

Difficulties related to stain gauge array gluing-on in the vicinity of the drilled-out hole can be overcome by using laser interferometry methods.

In recent years a new contactless method of laser interferometry — electron speckle-interferometry — has been widely accepted for determination of displacements and deformations [6–8], which is practically insensitive to accurate positioning of the drilled-out hole or its dimensions. The hole used for elastic unloading of residual stresses can be made in any point of the section illuminated by the laser beam. Light waves reflected before and after hole drilling out using a CCD-camera, are stored in the computer memory and are processed to obtain the residual stress values.

The purpose of this study is improvement of the procedure of evaluation of residual stresses in welded joints and structural elements with application of electron speckle-interferometry.

Speckle-interferometry method of residual stress determination is based on using the optical circuit of interferometric measurement system (Figure 1), in which the studied section of the object is illuminated at the same angle symmetrically in two directions, this allowing determination of the plane components of the displacement vector, characterizing object deformation in its plane.

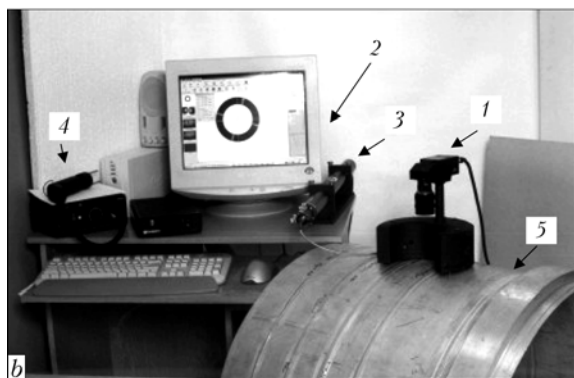
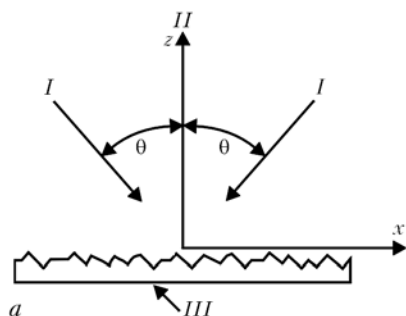


**Figure 1.** Optical circuit (a) and general view (b) of speckle-interferometric measuring system: *I* and *II* — directions of illumination and observation, respectively; *III* — studied object section; *1* — drilling device; *2* — computer; *3* — laser; *4* — speckle-interferometer; *5* — studied object

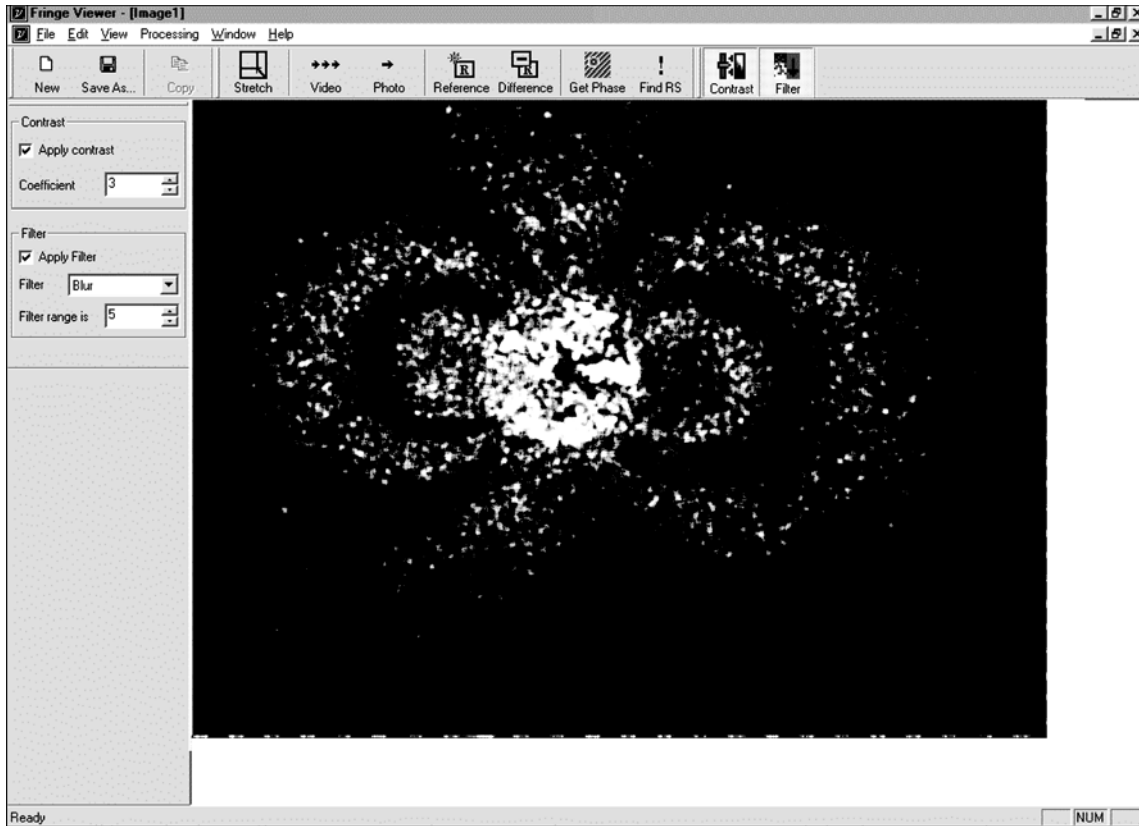


Figure 2. Typical fringe pattern in the vicinity of blind hole in residual stress field

Studies showed that optimum angle  $\theta$  between the normal to the point of the considered section and direction of illumination is equal to  $57^\circ$ .

In order to determine the residual stresses in the structural elements and assemblies based on the given optical circuit, a small-sized speckle-interferometry module was developed, which is mounted directly on the studied object surface (Figure 1, b).

Measurement of residual stresses by the speckle-interferometry method is performed as a following sequence. The small-sized speckle-interferometric module is mounted on the studied object surface. Reflected light wave, characterizing the initial condition of the controlled section, is stored in the computer memory using a CCD-camera. After elastic unloading of stresses due to drilling of a blind hole of diameter  $D$  and depth  $H$  of approximately 1–2 mm, the reflected light wave is also stored in the computer memory. After computer processing of the two light waves, generated before and after local unloading of residual stresses, the monitor displays the interference fringe pattern in the hole vicinity, containing information on residual stresses in the controlled point of the studied section of the object (Figure 2).

For a stretched plate with a through-thickness hole, displacements in the hole vicinity can be calculated analytically using the obtained dependencies [9].

In the case of a stretched plate with a blind hole, analytical solution for calculation of displacements in the vicinity of such a hole is absent, so that empirical formulas are used [10, 11].

Dependence of displacements  $u_r$  and  $u_\theta$  (Figure 3), resulting from elastic unloading of stresses  $\sigma_{xx}$ ,  $\sigma_{yy}$  and  $\tau_{xy}$ , on angle  $\theta$  at a certain distance from hole center  $r$ , is expressed by the following formulas [12]:

$$u_r(r, \theta) = \bar{A}(\sigma_{xx} + \sigma_{yy}) + \bar{B}[(\sigma_{xx} - \sigma_{yy}) \cos 2\theta + 2\tau_{xy} \sin 2\theta];$$

$$u_\theta(r, \theta) = \bar{C}[(\sigma_{xx} - \sigma_{yy}) \sin 2\theta - 2\tau_{xy} \cos 2\theta],$$

where  $\bar{A}$ ,  $\bar{B}$  and  $\bar{C}$  are the empirical coefficients dependent on mechanical properties of the material, distance from the hole center and its diameter.

Developed procedure envisages measurement by the method of electron speckle-interferometry of displacement component  $u_x$  at a constant distance from

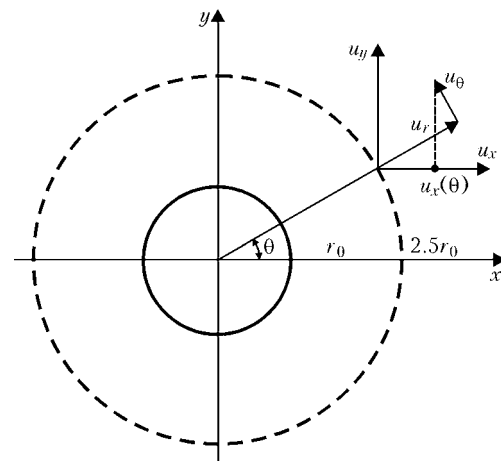
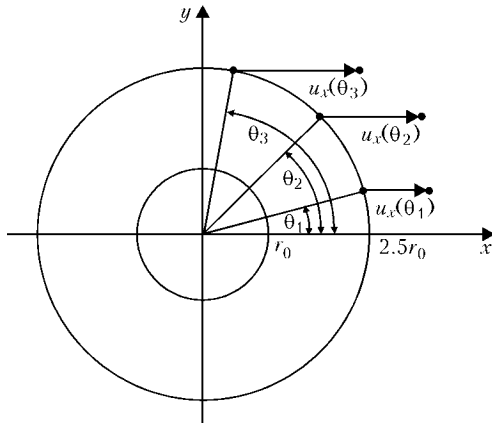


Figure 3. Schematic of location of co-ordinate axes and measured components of the displacement vector at elastic unloading of residual stresses using hole drilling



**Figure 4.** Schematic of location of points at residual stress determination

the hole center (for instance,  $r = 2.5r_0$ ), which is related to displacements  $u_r$  and  $u_\theta$  (Figure 3) by the following relationship:

$$u_x(r, \theta) = u_r(r, \theta) \cos \theta - u_\theta(r, \theta) \sin \theta. \quad (1)$$

After transformations equation (1) becomes

$$u_x(\theta) |_{r=2.5r_0} = F(\theta)\sigma_{xx} + G(\theta)\sigma_{yy} + H(\theta)\tau_{xy}, \quad (2)$$

where

$$\begin{aligned} F(\theta) &= (\bar{A} + \bar{B} \cos 2\theta) \cos \theta - \bar{C} \sin 2\theta \sin \theta, \\ G(\theta) &= (\bar{A} - \bar{B} \cos 2\theta) \cos \theta + \bar{C} \sin 2\theta \sin \theta, \\ H(\theta) &= 2\bar{B} \sin 2\theta \cos \theta + 2\bar{C} \cos 2\theta \sin \theta \end{aligned}$$

are the functions, dependent on mechanical properties of the material, distance from the hole centre and its diameter, respectively.

As equation (2) includes three unknowns  $\sigma_{xx}$ ,  $\sigma_{yy}$  and  $\tau_{xy}$ , then to solve the system of linear equations

$$\begin{cases} F(\theta_1) & G(\theta_1) & H(\theta_1) \\ F(\theta_2) & G(\theta_2) & H(\theta_2) \\ F(\theta_3) & G(\theta_3) & H(\theta_3) \end{cases} \begin{cases} \sigma_{xx} \\ \sigma_{yy} \\ \tau_{xy} \end{cases} = \begin{cases} u_x(\theta_1) \\ u_x(\theta_2) \\ u_x(\theta_3) \end{cases} \quad (3)$$

and find the unknown components of the stress tensor, it is enough to have the data on displacements in three points ---  $u_x(\theta_1)$ ,  $u_x(\theta_2)$ ,  $u_x(\theta_3)$  (Figure 4).

Solution of a system of equations (3) allows finding  $\sigma_{xx}$ ,  $\sigma_{yy}$  and  $\tau_{xy}$ , while principal stresses  $\sigma_1$ ,  $\sigma_2$  and angle  $\eta$  between axis  $x$  and direction  $\sigma_1$  are determined from the following equations:

$$\sigma_1, \sigma_2 = \frac{\sigma_{xx} + \sigma_{yy}}{2} \pm \sqrt{\left(\frac{\sigma_{xx} - \sigma_{yy}}{2}\right)^2 + \tau_{xy}^2}; \quad (4)$$

$$\eta = \begin{cases} \frac{1}{2} \tan^{-1} \left( \frac{2\tau_{xy}}{\sigma_{xx} - \sigma_{yy}} \right) & \text{if } \sigma_{xx} > \sigma_{yy}, \\ \frac{\pi}{4} & \text{if } \sigma_{xx} = \sigma_{yy}, \\ \frac{\pi}{4} + \frac{1}{2} \tan^{-1} \left( \frac{2\tau_{xy}}{\sigma_{xx} - \sigma_{yy}} \right) & \text{if } \sigma_{xx} < \sigma_{yy}. \end{cases} \quad (5)$$

It should be noted that at computer analysis of speckle-interferograms, their automatic processing is essentially affected by the phase pattern noise, made up by the electronic noise of the video camera, speckle-noise, laser radiation noise, etc. If the phase pattern contains a lot of noise, additional correction of the algorithm of speckle-pattern interpretation by the operator is required, this leading to an essential extension of processing time, as well as a certain subjectivity of the obtained results. Therefore, for evaluation of the noisiness of the phase pattern, a noise parameter was proposed and its threshold value was established, at which the probability of successful automatic processing is more than 90 %.

To determine the distance, at which measurement of displacements with the speckle-interferometer will be the most accurate, a number of experiments were performed by the following procedure: holes of radius  $r_0$  were drilled out in a stressed sample, and the thus formed interference fringe patterns were recorded.

As a two-dimensional algorithm of the «shortest path» is optimum for interferogram processing, it is necessary to determine a region, in which displacement values are calculated. It is obvious that the narrower is this region, the lower is the probability of a successful fulfillment of the «shortest path» algorithm. However, use of a too wide region leads to considerable time consumption, and does not yield any significant improvement of the effectiveness of computer processing of the interferograms.

Investigation showed that to measure displacements along a circumference of radius  $kr_0$  (where  $k \geq 2.0$  is an arbitrary coefficient), it is sufficient to study a region in the form of a ring of a width equal to the radius of a drilled-out hole of radius  $r_0$  and with inner radius  $(k - 0.5)r_0$ .

Figure 5 shows that at  $k = 2.0$  the noise level in the interferogram is higher than the threshold, at which automatic determination of the values of displacements around a circumference is possible; at  $k = 2.5$  the noise level does not exceed the threshold value, and at  $k = 3.0$ , its value drops practically to zero.

It should be noted that displacements occurring after hole drilling in a stressed material are the higher, the smaller is  $k$  value (the closer is the displacement measurement point to the hole edge). Thus, in order to improve the measurement accuracy, it is necessary to try to achieve such minimum  $k$  values, at which stable automatic computer processing of the interferogram is performed. Therefore, distance equal to  $2.5r_0$

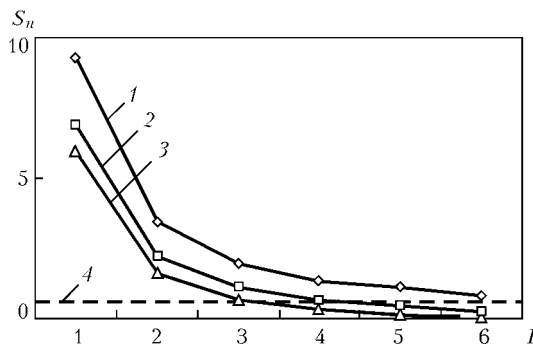


**Figure 5.** Dependence of level of noise  $S_n$  on number of iterations  $I$  of filtration in the circular regions of test interferogram at different values of  $k$  parameter: 1 --- 2.0; 2 --- 2.5; 3 --- 3.0; 4 --- threshold



from hole center, is optimum for measurement of displacements around a circumference.

To solve the system of linear equations (3) and determine the components of the stress tensor, it is necessary to find empirical coefficients  $\bar{A}$ ,  $\bar{B}$  and  $\bar{C}$  [10]. It is known [10] that these coefficients calculated for a uniaxial stressed state of the studied object, should be also valid for a biaxial state.

Therefore, to determine empirical coefficients  $\bar{A}$ ,  $\bar{B}$  and  $\bar{C}$  the sample was tested by uniaxial tension in a mechanical press, with the known stress level  $\sigma$ . The developed speckle-interferometer was used to store in the computer memory the initial speckle-patterns of the sample surface, obtained at its illumination by the laser in two directions normal to each other, namely along and normal to the axis of tension. Then a hole of radius  $r_0$  was drilled out so that its depth were equal to diameter ( $H = D = 2r_0$ ), and the speckle-pattern of the surface after hole drilling out was stored in the computer. Their processing was followed by calculation of the projection of the displacement vector on axis  $Ox$  in points  $u_0$  and  $u_{45}$  at angles of 0 and 45° at distance of  $2.5r_0$  from the center of the drilled out hole (Figure 6). Then the module of the speckle-interferometer was installed normal to its initial position, and the projection of the displacement vector to  $Oy$  axis was determined in a similar fashion in points  $v_0$  and  $v_{45}$  at angles of 90 and 45° at a fixed distance of  $2.5r_0$  from the center of the drilled out hole.

Measured displacements  $u_x$  were used to determine the unknown empirical coefficients  $\bar{A}$ ,  $\bar{B}$ , and  $\bar{C}$ :

$$\begin{aligned} \bar{A} &= \frac{1}{2} \frac{u_0 + v_0}{\sigma} = \frac{\sqrt{2}}{2} \frac{u_{45} + v_{45}}{\sigma}, \\ \bar{B} &= \frac{1}{2} \frac{u_0 - v_0}{\sigma}, \\ \bar{C} &= \frac{\sqrt{2}}{2} \frac{u_{45} - v_{45}}{\sigma}. \end{aligned} \quad (6)$$

It should be noted that empirical coefficient  $\bar{A}$  can also be calculated from two relationships (6). This allows additional checking of the correctness of the staged experiment on determination of empirical coefficients. It should be also noted that these coefficients are independent on the stress level and are only valid for the given hole parameters and distance, at which displacements are measured, as well as set of elastic constants.

In order for the empirical coefficients to be independent on hole diameter and elastic constants of the studied materials, it is convenient to calculate the following dimensionless empirical coefficients:

$$\bar{a} = \frac{2E}{r_0(1+\nu)} \bar{A}, \quad \bar{b} = \frac{2E}{r_0} \bar{B}, \quad \bar{c} = \frac{2E}{r_0} \bar{C}.$$

Thus, for any isotropic materials, it is possible to calculate the respective empirical coefficients  $\bar{A}$ ,  $\bar{B}$  and  $\bar{C}$  from (7) to determine the stressed state:

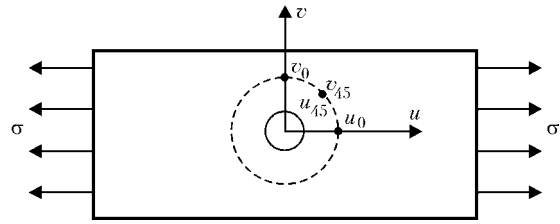


Figure 6. Schematic of measurement of displacements at experimental determination of empirical coefficients  $\bar{A}$ ,  $\bar{B}$  and  $\bar{C}$

$$\bar{A} = \frac{r_0(1+\nu)}{2E} \bar{a}, \quad \bar{B} = \frac{r_0}{2E} \bar{b}, \quad \bar{C} = \frac{r_0}{2E} \bar{c}. \quad (7)$$

Performed investigations allowed development of an algorithm for determination of residual stresses by drilling a blind hole and measurement of displacements, resulting from elastic unloading of stresses, which consists of the following stages:

1) using the known mechanical constants of the studied material, empirical coefficients  $\bar{A}$ ,  $\bar{B}$  and  $\bar{C}$  are calculated by formulas (7);

2) at distance of  $2.5r_0$  from the center of the drilled out hole, three points are selected at arbitrary angles  $\theta_1$ ,  $\theta_2$  and  $\theta_3$  relative to the axis of illumination;

3) method of electron speckle-interferometry is used to measure  $u_x(\theta_1)$ ,  $u_x(\theta_2)$ ,  $u_x(\theta_3)$  displacements in the selected points;

4) system of linear equations (3) is constructed;

5) system of linear equations (3) is solved, this allowing finding unknown components of the stress tensor  $\sigma_{xx}$ ,  $\sigma_{yy}$  and  $\tau_{xy}$ ;

6) formulas (4), (5) are used to calculate the values of principal stresses  $\sigma_1$ ,  $\sigma_2$ , and angle  $\eta$ , measured between the axis of illumination of speckle-interferometer and  $\sigma_1$  direction;

7) repetition of stages 2–6 for the other three points with subsequent averaging of the obtained results of stress calculation allows a considerable improvement of the accuracy of residual stress determination.

To evaluate the accuracy of measurement of plane displacements using a small-sized speckle-interferometer and automated computer processing of the interferograms, the problem of bending of a cantilever beam (Figure 7) with a restrained end by a force applied to the beam free end [13] was solved.

Displacements and stresses  $\sigma_{xx}$  induced by load application, were calculated by the following formulas:

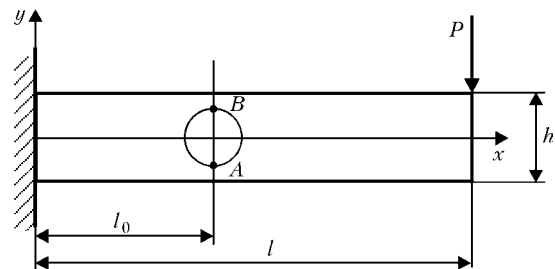
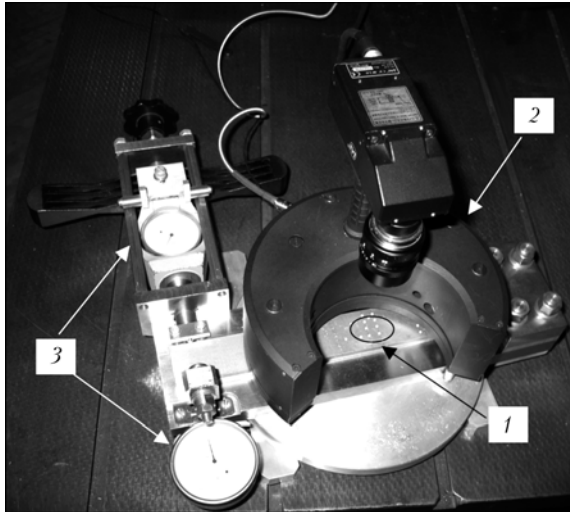


Figure 7. Schematic of loading and measurement of displacements  $u_x$  in the studied sample:  $l_0$  — distance from section AB to point of beam restraint (for the rest see designations in the text)



**Figure 8.** General view of speckle-interferometer: 1 — device for monitoring beam displacements under the impact of load; 2 — small-sized instrument; 3 — studied sample

$$u_x = -\frac{P}{EJ}y \left( lx - \frac{x^2}{2} \right) - \frac{P}{6EJ}(\nu + 2)y^3 + \frac{P}{6EJ}(\nu + 2)h^2y; \quad (8)$$

$$\sigma_{xx} = \frac{P(l - x)y}{J}, \quad (9)$$

where  $P$  is the applied load;  $E$  is the Young's modulus;  $J = 2bh^3/3$  is the moment of inertia of the beam cross-section relative to a neutral line;  $\nu$  is the Poisson's ratio;  $l$ ,  $h$  and  $b$  are the beam length, height and width, respectively.

During the experiments a  $270 \times 40 \times 8.5$  mm beam from aluminium alloy AMg6 rigidly restrained by a special mechanical device was studied. Load  $P = 600$  MPa was applied to the beam free end, its level being controlled using a dynamometer. Shifting of the beam free end under the impact of the applied force was further controlled using a micrometer. Speckle-interferometer (Figure 8) was mounted so that it was possible to record displacements in the sample central part (in Figure 7 the measurement region is marked by a circle of 6 mm diameter,  $l_0 = 110$  mm). Values of projection of displacement vector  $u_x$  of beam surface points on axis  $Ox$  were determined experimentally using the developed compact speckle-interferometer and were compared with the theoretical values calculated by formula (8).

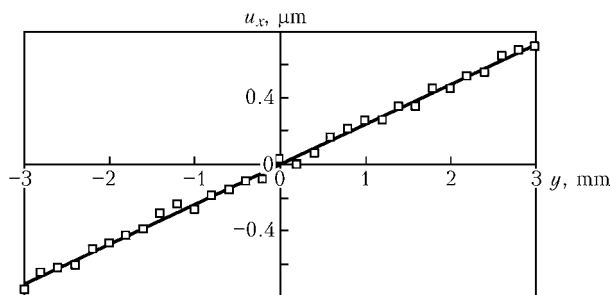


**Figure 9.** Distribution of displacements  $u_x$  along section AB (see Figure 7):  $\square$  — experimental data obtained with the speckle-interferometer; solid line —  $u_x$  design values

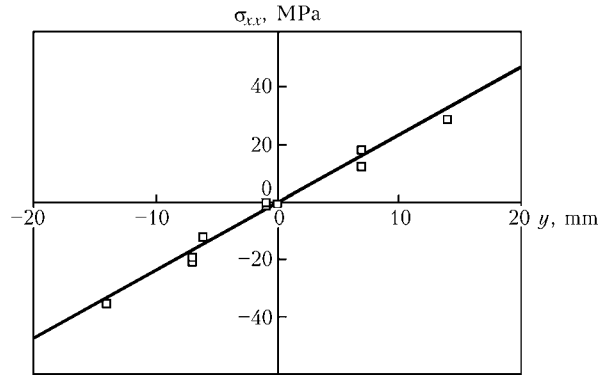


**Figure 10.** Distribution of stresses  $\sigma_{xx}$  along studied section AB ( $P = 600$  MPa):  $\square$  — experimental data; solid line —  $\sigma_{xx}$  design values

As is seen from Figure 9, maximum deviation of experimental data from the theoretical data calculated by formula (8), is equal to  $0.04 \mu\text{m}$  (error of displacement measurement —  $\lambda/15$ , where  $\lambda$  is the wave length of a coherent radiation source).

Distribution of stresses  $\sigma_{xx}$  along AB section (Figure 10) shows that deviation of stress values determined by speckle-interferometry method from the theoretical values calculated by formula (9) does not exceed 5 % of the studied material yield point ( $\sigma_{0.2} = 160$  MPa).

Developed procedure of residual stress determination allowed studying the stressed state in welded joints, made by the regular technology and with application of pre-tension of the elements being welded. At retrofitting of the technology of welding butt joints two sheets of alloy AMg6 each of  $1000 \times 240 \times 6$  mm dimensions, were used. Butt joints were made using AC TIG welding.

From Figure 11 it is seen that welding of a butt joint under the conditions of an elastic pre-tension

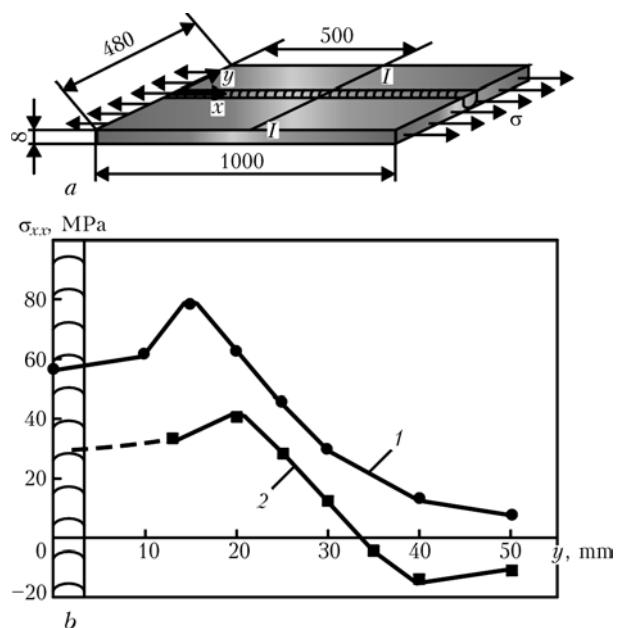


**Figure 11.** Schematic of sample (a) of welded joint of AMg6 alloy and distribution of residual stresses in it (b) along section I-I in welding without (1) or with (2) pre-tension



(up to  $\sigma = 0.75\sigma_{0.2}$ ) allowed reducing the residual stresses 2 times.

Performed research showed that the developed procedure of determination of residual stresses in welded structure elements based on electron speckle-interferometry in combination with a probing hole, as well as the developed small-sized instrument allow studying the stress distribution over the surface of the controlled objects quickly and with a high accuracy (of approximately 5 % of material yield point). The developed procedure of residual stress determination, compactness of the equipment and efficiency of computer processing of optical information opens up new possibilities for studying the structures under the laboratory and shop conditions.

1. Kasatkin, B.S., Kudrin, A.B., Lobanov, L.M. et al. (1981) *Experimental methods of strain and stress study*. Kiev: Naukova Dumka.
2. (1990) *Experimental mechanics*. Ed. by A. Kobayashi. Book 2. Moscow: Mir.
3. Birger, I.A. (1985) Residual stresses in structural elements. In: *Transact. of 2nd All-Union Symp. on Residual Technological Stresses*. Moscow: Mir.
4. Lobanov, L.M., Mikhoduj, L.I., Pivtorak, V.A. et al. (1995) Influence of peculiarities of submerged-arc welding technology on stressed state of welded joints of high-strength steels. *Avtomatich. Svarka*, **9**, 70-73.
5. Bratukhin, A.G., Lobanov, L.M., Pivtorak, V.A. et al. (1995) Residual stresses in aircraft structure elements of 1420 alloy. *Ibid.*, **3**, 10-13.
6. Moore, A.J., Tyrer, J.R. (1996) Two-dimensional strain measurement with ESPI. *Opt. Lasers Eng.*, **24**, 381-402.
7. Zhang, J. (1998) Two-dimensional in-plane electronic speckle pattern interferometer and its application to residual stress determination. *Ibid.*, **37**, 2402-2409.
8. Sirohi, R.S. (1993) *Speckle metrology*. New York.
9. Lobanov, L.M., Pivtorak, V.A. (1998) Development of holographic interferometry for study of stress-strain state and quality control of welded structures. In: *Advanced materials science of the 21st century*. Kiev: Naukova Dumka.
10. Makino, A., Nelson, D. (1994) Residual stresses determination by single-axis holographic interferometry and hole-drilling. Part. 1. *Theory Exp. Mech.*, **34**, 66-78.
11. Wu, Z., Lu, J., Joulaud, P. (1997) Study of residual stresses distribution by moire interferometry incremental hole drilling method. In: *Proc. of 5th Int. Conf. on Residual Stresses* (LinKoping, Sweden, June 1997). LinKoping.
12. Schaer, G.S. (1981) Application of finite element calculations to residual stresses measurements. *J. Eng. Mater. Tech.*, **4**(103), 157-163.
13. Timoshenko, S.P. (1972) *Course of elasticity theory*. Kiev: Naukova Dumka.

## ELECTRON SHEAROGRAPHY – EXPRESS METHOD OF NON-DESTRUCTIVE QUALITY CONTROL OF STRUCTURE ELEMENTS

At the E.O. Paton Electric Welding Institute a mobile shearographic equipment and technology for non-destructive quality control of objects of optional shape, manufactured from different structural materials, have been developed.

The electron shearography allows producing directly the lines of constant values of derivatives from displacements along the preset direction of shear. This stipulates non-sensitivity of shearography to rigid displacements of the object caused by the effect of surrounding medium and, as a result, the feasibility of its application for the quality control of structures under the industrial conditions.

The mobile shearographic complex consists of a laser light source 1, a distributing optical system 2, a small-sized shearographic interferometer 3 and a portable computer 4. Shearographic equipment operates in real-time conditions and allows revealing defects of type of cracks, lack of penetration, inclusions, areas of concentration of deformations and non-quality adhesion or brazing in elements of structures manufactured from metallic and composite materials.

**Purpose and application.** Electron shearography can be used in industry for measuring and analysis of deformations; non-destructive quality control of elements of arbitrary shape and sizes, made from different structural materials, and also for optimizing assemblies of mechanisms and elements of structures.

**Proposals for co-operation.** Conductance of non-destructive quality control of structure elements. Delivery of equipment and technology of shearographic non-destructive quality control to the Customer, training of personnel.

Contacts: Prof. Lobanov L.M.  
E-mail: office@paton.kiev.ua



# INCREASING FATIGUE RESISTANCE OF WELDED JOINTS BY HIGH-FREQUENCY MECHANICAL PEENING

V.V. KNYSH, A.Z. KUZMENKO and O.V. VOJTENKO  
E.O. Paton Electric Welding Institute, NASU, Kiev, Ukraine

Given are the results of fatigue tests of welded joints treated by strengthening high-frequency mechanical peening right after welding, as well as after operating for 50 % (and more) of their fatigue life. Factors were determined, which promote increase in welded joint fatigue resistance after application of this treatment, namely lowering of stress concentration coefficient, inducing of compressive residual stresses and strain hardening of metal surface layer.

*Keywords:* welded joint, mechanical peening, fatigue limit, cyclic fatigue life, fatigue curve, residual stresses, stress concentration coefficient, strain hardening, peening efficiency

Load-carrying capacity of welded metal structures operating under alternating loading is determined by fatigue of welded joints in members of these structures. As-welded joints have lower fatigue resistance, compared with base metal, which may not ensure the required life of a structure. One of the ways of increasing fatigue resistance of welded joints is to use additional strengthening treatments. The effect of some of them is based on decreasing the concentration of stresses (mechanical and electric arc treatment of welds), whereas the effect of others is based on redistribution of residual stresses within the stress raiser zones (general and local heat treatment, local heating, preliminary static overloading, surface work hardening, local plastic deformation, vibration and explosion treatment).

In the last years much consideration has been given to high-frequency mechanical peening (HFMP) of welded joints as one of the most promising methods, in terms of cost effectiveness, for increasing fatigue resistance of welded structural members. This method of plastic surface deformation of metal of welded joints within the stress raiser zones is based on utilisation of the ultrasound energy. The method can be imple-

mented both under production and service conditions. This treatment is sufficiently well studied. Main mechanisms of increasing cyclic fatigue life and fatigue limits of welded joints strengthened by HFMP were identified, and its advantages compared with other known methods of plastic surface deformation of metal were determined [1–6].

At the same time, there are some issues that remain to be solved, associated with determining the mechanisms of increasing fatigue resistance of welded joints strengthened by HFMP and peculiarities of application of this technology under structure service conditions. First of all, this concerns inspection of the quality of treatment of welded joints by HFMP and investigation of the efficiency of its utilisation for extending cyclic fatigue life of structures in operation after accumulation of a certain level of fatigue damages within the zones of stress raisers in their welded members. Only a limited number of publications are dedicated to these issues, and they cover mostly particular problems. For example, study [7] considers results of investigations of variations in the concentration of stresses in HFMP strengthened welded T-joints on high-strength steel, and study [8] gives experimental estimation of remaining life of tubular structures after HFMP performed during their operation.

The purpose of this study is to replenish experimental data required to comprehensively solve problems of practical application of the HFMP technology, particularly in terms of extending fatigue life of active welded structures characterised by accumulation of different levels of fatigue damage.

It is a known fact that extension of cyclic fatigue life of welded structures strengthened by HFMP is provided by an integrated effect of a number of factors, such as relieving tensile stresses and inducing favourable compressive residual stresses within the stress raiser zones, decreasing the concentration of effective stresses, and strain hardening of the surface layer of metal. The last of the above factors can be used as a basis for assessment of quality of HFMP of welded joints. For example, at a set speed of HFMP in HAZ of a welded joint (as a rule, it equals about 0.5 m/min) the quantity of passes of a work tool,

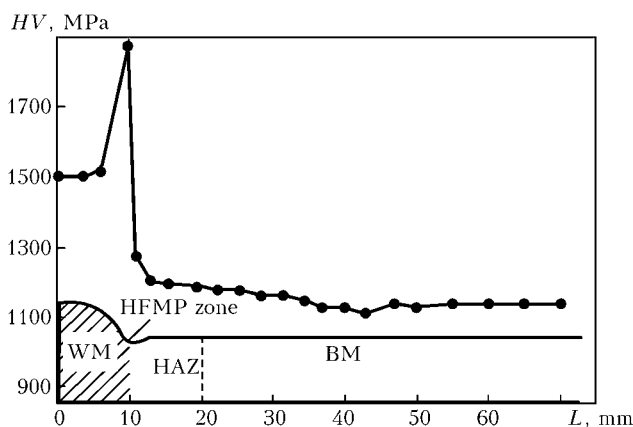


**Figure 1.** Dependence of hardness  $HV$  of surface metal layer strengthened by HFMP upon distance  $L$  to a fillet welded stiffener: WM — weld metal; BM — base metal

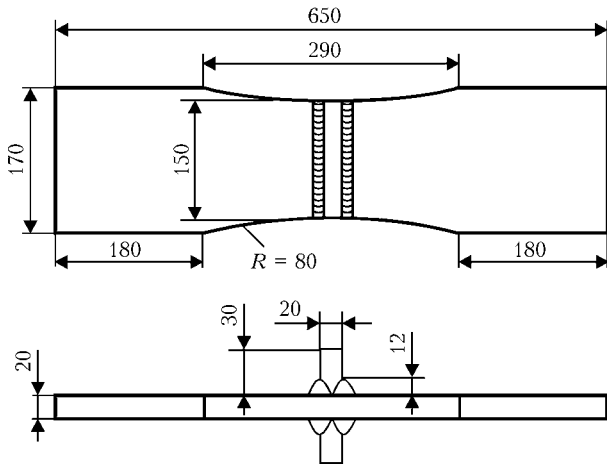


**Figure 2.** Schematic of welded joint in low-carbon steel St3sp

which provides the maximal level of strain hardening of the surface metal layer, can be taken as optimal.

Hardness of different regions of a T-joint in steel St3sp (killed) with distance from the treated weld was measured to study strain hardening of the HAZ metal after HFMP (Figure 1). Samples of T-joints with fillet welds that bear no load (Figure 2) were made by manual electric arc welding with full penetration of metal. Base metal (St3sp) had the following chemical composition, wt. %: 0.21C, 0.205Si, 0.52Mn, 0.019S, 0.007P, 0.04Cr, 0.04Ni, and less than 0.01Cu. It was characterised by the following mechanical properties:  $\sigma_y = 260$  MPa,  $\sigma_t = 465$  MPa,  $\delta = 37.6$  %, and  $\psi = 63$  %.

The results obtained (see Figure 1) are indicative of a substantial growth of metal hardness directly in the groove, which is usually 2–7 mm wide and 0.2–0.5 mm deep in the case of quality HFMP. Increase in values of metal hardness in the groove compared with hardness of the base metal was about 60 %, while that compared with hardness of the HAZ metal was about 40 %, and that compared with hardness of the weld metal was 27 %.

The dependence of variation in hardness of metal of welded joints in the same steel strengthened by HFMP upon the quantity of passes of a work tool (Figure 3) was derived. The measurements of hardness were made in the said groove within the zone of weld to base metal transition after HFMP at a certain quantity of passes of the work tool. This dependence indicates to the fact that maximal values of hardness of metal of the steel St3sp welded joints are stabilised

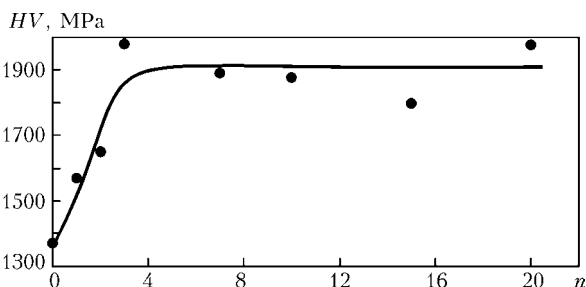


**Figure 3.** Dependence of hardness HV of surface metal layer in groove of sample of the T-joint in steel St2sp strengthened by HFMP upon quantity n of passes of work tool

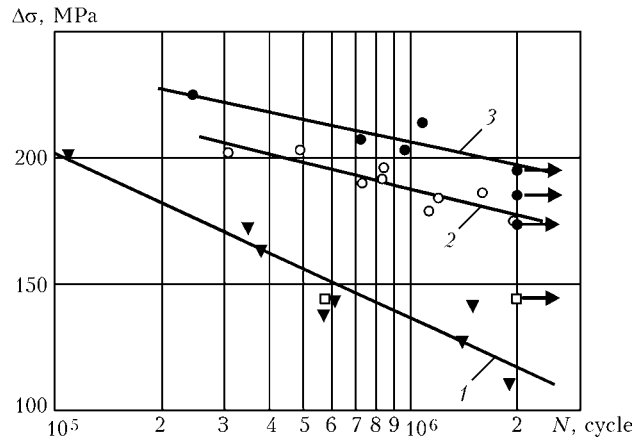


**Figure 4.** Fatigue curves of welded joints in low-carbon steel St3sp plotted for sample in as-welded condition (1), treated by HFMP in as-welded condition (2) and after operation for 50 % of fatigue life (3): □ — results of tests after operation of sample for about 95 % of its fatigue life

after four passes of the work tool. This may be used as a criterion for quality HFMP of welded joints in steel of the said grade at a preset speed of the work tool travel equal to 0.5 m/min. Therefore, postweld HFMP of the investigated welded joints (see Figure 2) was performed on the basis of the established criterion.

To estimate the efficiency of application of HFMP for increasing fatigue resistance of welded joints after operation for 50 % of their fatigue life, three series of welded samples (see Figure 2) were fatigue tested using testing machine TsDM 200pu at uniaxial alternating tension with cycle asymmetry  $R_\sigma = 0$ .

Samples of the first series were tested in the as-welded condition, samples of the second series were subjected to HFMP in the as-welded condition, and samples of the third series — after operation for 50 % of their fatigue life. The resulting fatigue curves (Figure 4) demonstrate a more than 2 times extension of fatigue life of the samples tested in a range of maximal values of stresses  $\sigma_{max} = 175$ –225 MPa, compared with the second series of the samples, and an order of magnitude extension of fatigue life compared with the first series of the samples tested at the same levels of maximal stresses. In this case, the fatigue limits on a base of  $2 \cdot 10^6$  cycles of alterna-

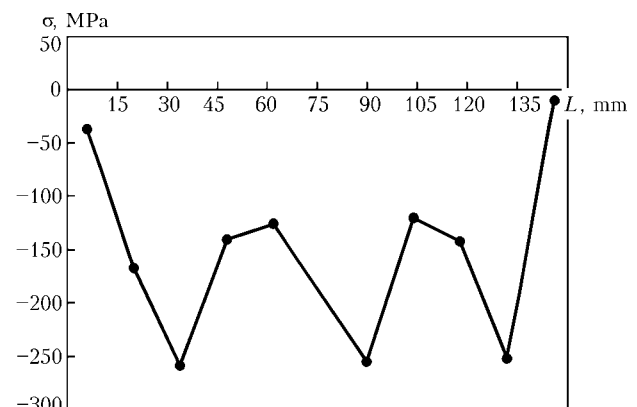


**Figure 5.** Distribution of transverse residual stresses in sample of steel St3sp T-joint along the groove formed in HFMP

Averaged values of profile geometry parameters, stress concentration coefficient  $K_t$  and its square deviations  $S_d$

Sample No.	Type of treatment	$\rho$ , mm	$\theta$ , deg	$b$ , mm	$h$ , mm	$K_t$	$S_d$
1	Without treatment	1.86	47.9	20	23	2.06	0.193
2	HFMP	1.94	35.6	27	22	1.78	0.066
3	Pneumatic peening	4.12	42.5	30	20	1.61	0.024
4	Shot blasting	1.95	35.7	25	22	1.85	0.076
5	Argon arc glazing	5.40	42.8	25	24	1.56	0.018
6	HFMP + argon arc glazing	6.14	44.3	30	22	1.46	0

Note.  $\rho$  and  $\theta$  --- radius and angle of weld to base metal transition in welded joint, respectively;  $b$  and  $h$  --- weld width and height, respectively.

tion of stresses increased by 50 %, compared with the initial state, for the second series of the samples, and by 66 % for the third series of the samples. This increase in fatigue life for the third series of the samples, which were preliminarily tested in the initial, as-welded, condition to operation for 50 % of their fatigue life at  $\sigma_{\max} = 200$  MPa and higher is attributable to overloading (formation of plastic strains) within the stress raiser zones and, accordingly, inducing of compressive residual stresses in these zones in the first loading cycles. Fatigue life of the samples additionally grew with subsequent HFMP.

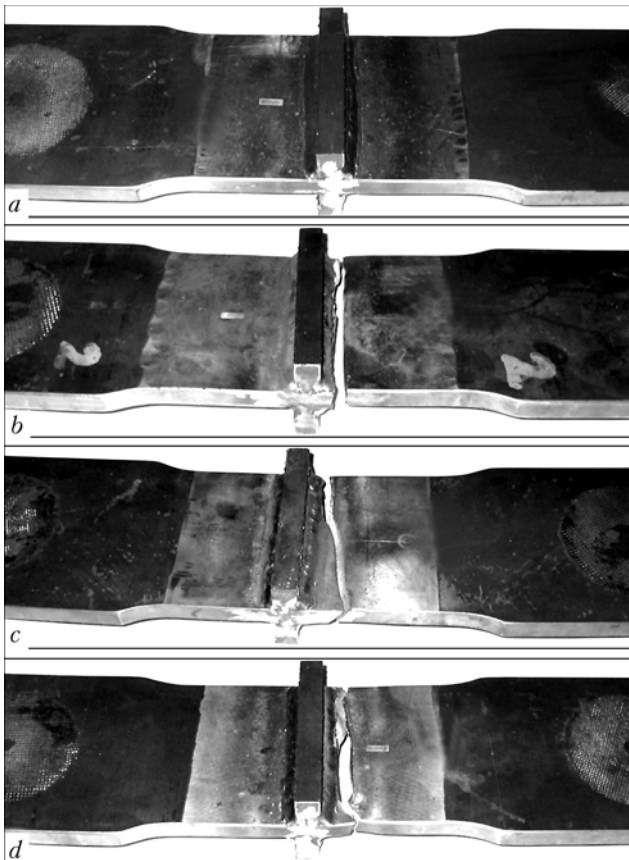


**Figure 6.** General view of fractured samples of T-joint in steel St3sp after fatigue tests at axial tension with cycle asymmetry  $R_\sigma = 0$ : *a* --- non-fractured sample subjected to HFMP; *b* --- sample tested in as-welded condition (without treatment); *c, d* --- samples tested after HFMP treatment in as-welded condition and after operation for 50 % of their fatigue life

Figure 4 shows the results of testing one sample at  $\sigma_{\max} = 145$  MPa, which was treated by HFMP after it had been in operation for about 95 % of its fatigue life. Prior to unloading and subsequent strengthening, the sample was visually examined to check initiation of fatigue cracks, and the latter were not detected. Further tests of the sample under the same loading conditions as before strengthening showed no cracks up to 2 million cycles of alternation of stresses.

The character of distribution of residual stresses in surface layer of the HAZ metal of welded joints subjected to work hardening was investigated to study factors leading to extension of cyclic fatigue life of welded joints treated by HFMP. As reported in [9–11,

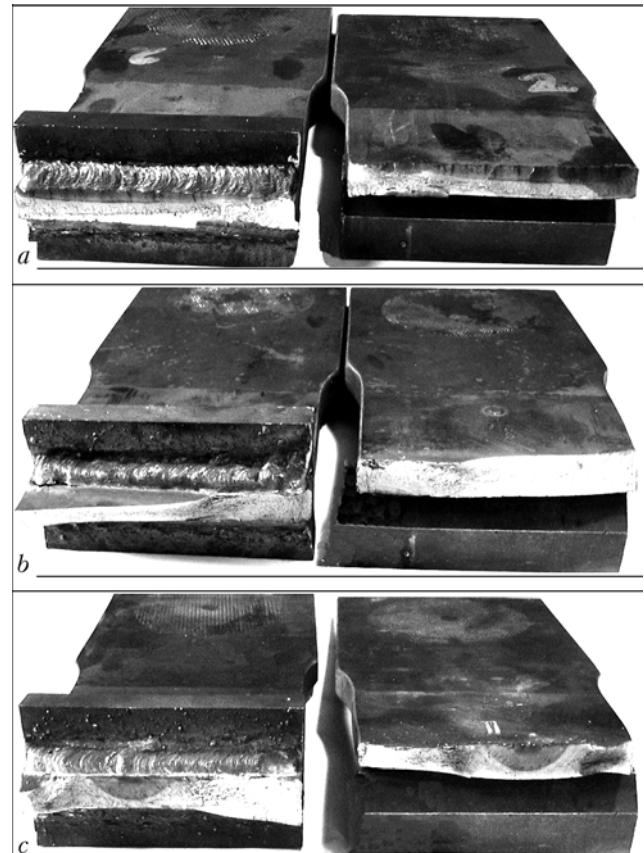


**Figure 7.** Fatigue fractures in samples of T-joint in steel St3sp: *a* --- sample tested in as-welded condition; *b, c* --- samples treated by HFMP in as-welded condition and after operation for 50 % of their fatigue life, respectively



etc.], the fields of tensile residual stresses are formed in large-scale specimens of the as-welded T-joints, and the value of a transverse component of these stresses may amount to yield stress of the base metal.

In this study the measurements were made by a destructive method [12], i.e. by successive mechanical unloading of fragments of the HAZ metal of a joint. Standard strain gauges with a gauge length of 1 mm were used to measure stresses. The strain gauges were placed in the immediate proximity to the end of the groove formed in strengthening of the HAZ metal.

The resulting dependence of distribution of the transverse component of residual stresses in a welded sample is shown in Figure 5. It can be seen from the Figure that the average value of the component of residual stresses in HAZ of the joint, which is oriented in the same direction as stresses due to the effective load, is higher than half of the yield stress value, and that it is close to zero at the ends of the sample. It is this fact that led to initiation of fatigue cracks when tests were conducted at the edges of the second series of the samples (using HFMP in the as-welded condition), unlike the first series of the samples, where cracks initiated at the centre (Figures 6 and 7). Cracks in the third series of the samples initiated far from the edges as a result of a combined effect of overloading and strengthening by HFMP (see Figures 6 and 7).

The role of another factor affecting increase of fatigue resistance of welded joints after HFMP, i.e. decrease of stress concentration coefficient  $K_t$ , was also investigated. For this, parameters of profile geometry of the welds in T-joints of low-alloy steel Weldox 420 were measured by the method of replicas [13]. The measurements were made in six series of welded joint samples: in the as-welded condition, after HFMP (diameter of a striker --- 3 mm), pneumatic peening, shot blasting, argon arc treatment, and argon arc glazing plus HFMP. The values of  $K_t$  and their square deviations (Table) were determined from the calculated dependencies recommended for a given type of joints in [14]. It can be seen from the Table that HFMP and other types of welding treatments widely applied in industry lead to decrease in  $K_t$  of welded joints. The maximal decrease in the stress concentration coefficient occurs after HFMP + argon arc glazing (30 %), whereas after HFMP alone it is only 14 %.

Insignificant decrease in  $K_t$  of the samples strengthened by HFMP, compared with the as-welded samples, cannot explain a substantial increase in fatigue resistance of the steel Weldox 420 samples strengthened by HFMP [5]. Therefore, a factor of decrease in  $K_t$  of the joints treated by HFMP plays a less important role in raising their fatigue resistance

than inducing of compressive residual stresses in stress raiser zones.

## CONCLUSIONS

1. Criterion of quality of the HFMP treatment of welded joints, conducted to provide an efficient growth of fatigue resistance of the joints, can be such a quantity of passes of the work tool at a speed of 0.5 m/min, at which stabilisation of the maximal level of hardness of metal within the treatment zone is achieved (four passes for T-joints in steel St3sp).
2. HFMP is efficient for extension of cyclic fatigue life and increase of fatigue limit of T-joints in steel St3sp both in treatment in the as-welded condition and after operation for 50 % or more of their fatigue life.
3. Compressive residual stresses induced in sub-surface layers of metal of the HFMP treatment zone are a decisive factor increasing fatigue resistance of the HFMP treated welded joints.

1. Trufiyakov, V.I. (1998) Increase of fatigue resistance of welded joints and structures. *Avtomatich. Svarka*, **11**, 11–19, 31.
2. Mikheev, P.P. (1990) Increase of fatigue resistance of structural welded joints by ultrasonic peening treatment. In: *Coll. on Problems of Welding and Special Electrometallurgy*. Kiev: Naukova Dumka.
3. Mikheev, P.P., Garf, E.F., Kuzmenko, A.Z. et al. (1992) Increase of fatigue resistance of pipe welded assemblies by ultrasonic peening treatment. *Avtomatich. Svarka*, **11/12**, 3–6.
4. Trufiyakov, V.I., Statnikov, E.S., Mikheev, P.P. et al. (1998) The efficiency of ultrasonic impact treatment for improving fatigue strength of welded joints. *IIW Doc. XIII-1745–98*.
5. Statnikov, E.S., Muktepavel, V.O., Trufiyakov, V.I. et al. (2000) Comparison of ultrasonic impact treatment (UIT) and other fatigue life improvement methods. *IIW Doc. XIII-1817–2000*.
6. Trufiyakov, V.I., Mikheev, P.P., Kudryavtsev, Y.F. (1995) *Fatigue strength of welded structures. Residual stresses and improvement treatments*. London: Harword AP.
7. Mikheev, P.P., Vojtenko, O.V. (2001) Role of stress concentration reduction at high frequency peening for fatigue resistance increase in welded joints. *The Paton Welding J.*, **11**, 42–44.
8. Garf, E.F., Litvinenko, A.E., Smirnov, A.Kh. (2001) Assessment of fatigue life of tubular connections subjected to ultrasonic peening treatment. *Ibid.*, **2**, 13–16.
9. (1990) *Strength of welded joints under alternative loads*. Ed. by V.I. Trufiyakov. Kiev: Naukova Dumka.
10. Makhnenko, V.I. (1976) *Computational methods of study of kinetic welding stresses and strains*. Kiev: Naukova Dumka.
11. Kasatkin, B.S., Prokhorenko, V.M., Chertov, I.M. (1987) *Stresses and strains in welding*. Kiev: Vyscha Shkola.
12. Dajchik, M.L., Prigorovskiy, N.I., Khurshudov, G.Kh. (1989) *Methods and equipment for full-scale tensometry*. Moscow: Mashinostroenie.
13. Asnis, A.E., Ivashchenko, G.A. (1978) *Increase of strength of welded structures*. Kiev: Naukova Dumka.
14. Makhnenko, V.I., Mosenkis, R.Yu. (1985) Calculation of stress concentration coefficient in butt and fillet welded joints. *Avtomatich. Svarka*, **8**, 7–18.

# REPAIR WELDING OF TITANIUM BLADES OF GAS TURBINE ENGINE COMPRESSORS

V.N. ZAMKOV, E.L. VRZHIZHEVSKY, V.F. TOPOLSKY and I.K. PETRICHENKO  
E.O. Paton Electric Welding Institute, NASU, Kiev, Ukraine

The feasibility was proved of reconditioning repair of the profile part of titanium alloy VT9 blades of gas turbine engine compressors made integral with disks.

*Keywords:* repair welding, compressor blades, titanium alloy, cladding, filler metals, microhardness, structure

Utilisation of titanium alloys in manufacture of gas turbine engine compressors depends in many respects upon the feasibility of reconditioning repair of blades to remove defects formed during operation. This issue takes on special significance if the design of a compressor provides for the use of all-milled impellers, i.e. blisks, where the blades are made integral with the disks.

Typical service defects in airfoils subject to repair include fracture of seals on the blade periphery, erosion damage of leading edges, and isolated fine cracks on trailing edges of blade profile parts, having the form of nicks and chips. If a blade is made integral with a disk, and an airfoil is not subject to repair, the blade can be replaced only by welding a new airfoil to the blisk disk.

The purpose of this study was to develop the repair method and technology to provide minimal (permissible) distortions after welding and acceptable mechanical properties of repaired blades to allow their further operation. It should be noted that in repair of blades of integral blisks it is impossible to subject them to postweld heat treatment.

As the type, size and location of a defect on the profile part of a specific blade are of a random character, and removal of the defect should be performed directly on a rotor, the technology available for repair of blade airfoils was based on application of manual TIG welding. Welding of a new airfoil to the blisk disk was performed by the electron beam method. Investigations were conducted on full-scale compressor blades of titanium alloy VT9 (Table 1), containing defects formed in operation, as well as fragments of

the disks with blades simulating integral blisks. As seen from Table 1, as to chemical composition meeting requirements of GOST 19807–91 for alloy VT9, the blade metal is a heat-resistant two-phase ( $\alpha + \beta$ ) titanium alloy of the martensitic type. It is intended for the manufacture of parts operating for a long time at a temperature of up to 500 °C. At this temperature its strength is equal to or higher than 600 MPa, while at normal temperature its tensile strength in the annealed state is over 1050 MPa.

Strength characteristics of the blade metal could not be determined because of a limited size of the blade. Therefore, properties of the base metal and metal of the blade regions subjected to repair were evaluated from the microhardness measurement results. It was found that microhardness of metal of the blades studied (base metal) was 3300 MPa on the average. Microstructure of metal across the blade section was characterised by heterogeneity: metal regions located near the airfoil edge had a globular structure (Figure 1, a, b), and metal of the central part of the blade had a globular-laminated structure (Figure 1, c, d).

For the blade to have an assigned performance, in addition to retaining the shape and size, it is necessary to ensure mechanical properties of the deposited metal close to those of the base metal. In the cases where it is impossible to perform postweld heat treatment, the above closeness of mechanical properties can be achieved mostly through selecting a proper chemical composition of the deposited metal, i.e. filler wire. Thus, defects on the blades were repaired by manual argon-arc welding using different grades of titanium welding wire (Table 2) and a specially developed welding torch of the T-1 type (Figure 2).

**Table 1.** Chemical composition (wt.%) of metal of titanium alloy VT9 blades

Sample location	Al	Mo	Zr	Si	Impurities, not more than				
					Fe	C	O <sub>2</sub>	N <sub>2</sub>	H <sub>2</sub>
Base metal	5.80–7.00	2.80–3.80	1.00–2.80	0.20–0.35	0.25	0.10	0.15	0.005	0.0150
Airfoil and fir-tree form	6.27	3.41	1.93	0.27	0.13	0.02	0.09	0.012	0.0032

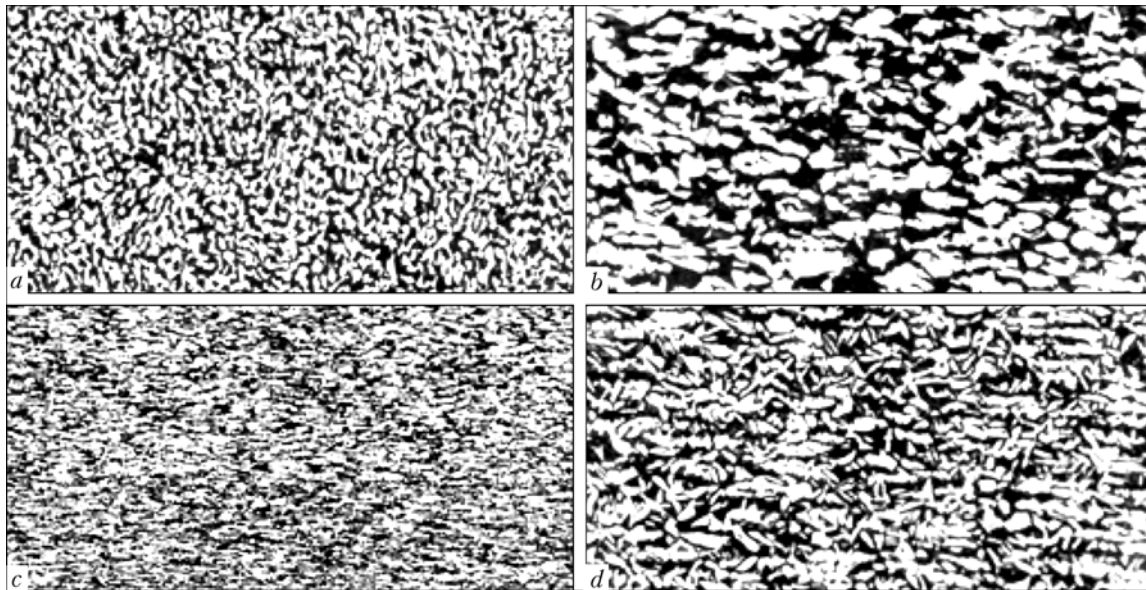


Figure 1. Microstructure of alloy VT9 blade metal: a, c ---  $\times 250$ ; b, d ---  $\times 800$

Table 2. Chemical composition (wt.%) of titanium-base filler wires

Wire grade	Al	Mo	V	Nb	Zr	Fe	Si	$K_{\beta}^{**}$
VT1-00sv	0.15	--	--	--	--	--	--	---
VT6sv	4.03	--	2.80	--	--	--	--	0.20
VT9*	6.25	3.41	--	--	1.93	--	0.27	0.31
VT20-1sv	2.62	1.41	1.34	--	1.20	--	--	0.23
SP15	4.30	2.18	2.35	4.50	1.51	--	--	0.53
T110*	5.60	1.00	1.20	4.30	0.35	1.25	--	0.62

\* --- rods cut from plate; \*\*  $K_{\beta}$  ---  $\beta$ -phase stabilisation coefficient.

In all cases the deposited metal had an acicular martensite-like structure. The deposited metal produced by using a filler wire of commercial titanium VT1-00sv had a heterogeneous microstructure characterised by the presence of the fine martensitic  $\alpha'$ -phase (Figure 3). In metal deposited by using wires VT6sv and VT20-1sv characterised by a lower alloying degree compared with the base metal (VT9), the length of martensite needles was larger than in the HAZ metal (Figure 4, a, b).

Structure of the metal deposited with filler metal of the same composition as base metal (VT9) was identical to that of the near-weld HAZ metal (Figure 4, d). Utilisation of filler wires SP15 and T110 with a higher alloying degree compared with the base metal led to formation of a fine martensitic structure in the deposited metal. It should be noted that violation of the technology of preparation of the blade surface for welding (cladding) leads to formation of defects of the type of micropores (Figure 5, a) and lacks of penetration (Figure 5, b).

Microhardness of the deposited metal along and across the weld bead was studied using the PMT-3 device. The results are shown in Figure 6. Hardness of the metal deposited with wire of commercial titanium and alloys VT6sv and VT20-1sv was lower than

that of the HAZ metal by 1000, 600 and 300 MPa, respectively.

Values of microhardness  $HV$  of the deposited metal produced by using filler metal VT9 and wire SP15 were close to values of microhardness of the HAZ and base metals. Therefore, it can be concluded that utilisation of the above filler metals can provide the high-

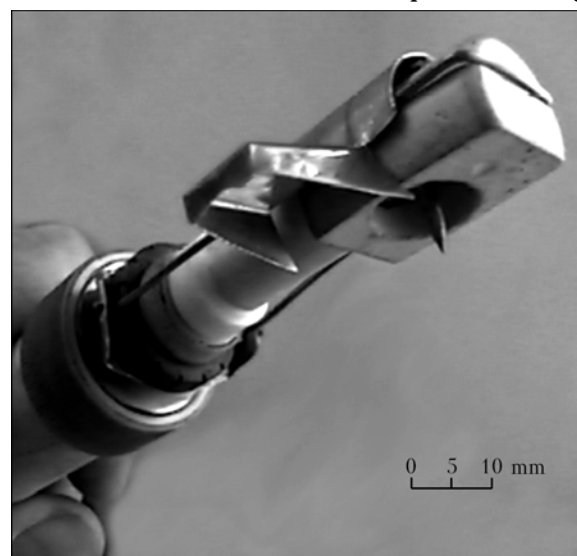


Figure 2. Small-size torch of the T-1 type for TIG welding

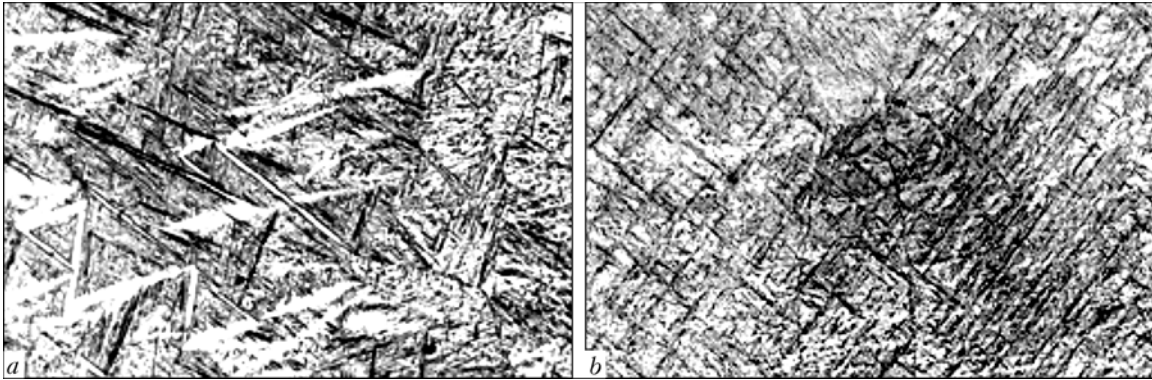


Figure 3. Microstructure of deposited metal of the blade region subjected to repair using wire VT1-00sv with coarse- (a) and fine-acicular (b) structure (x250)

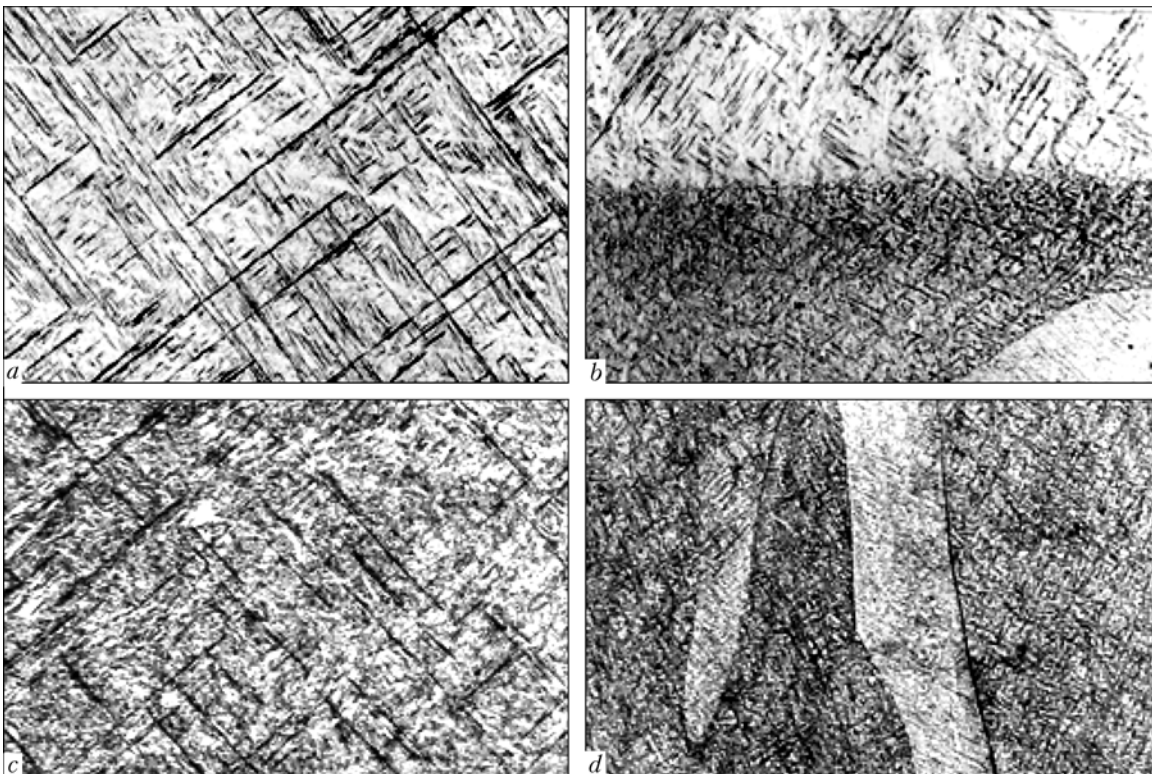


Figure 4. Microstructure of metal deposited with filler metals having a different alloying degree: a, b — VT6sv (a — deposited metal; b — fusion zone); c — VT20-1sv; d — VT9 (x250)

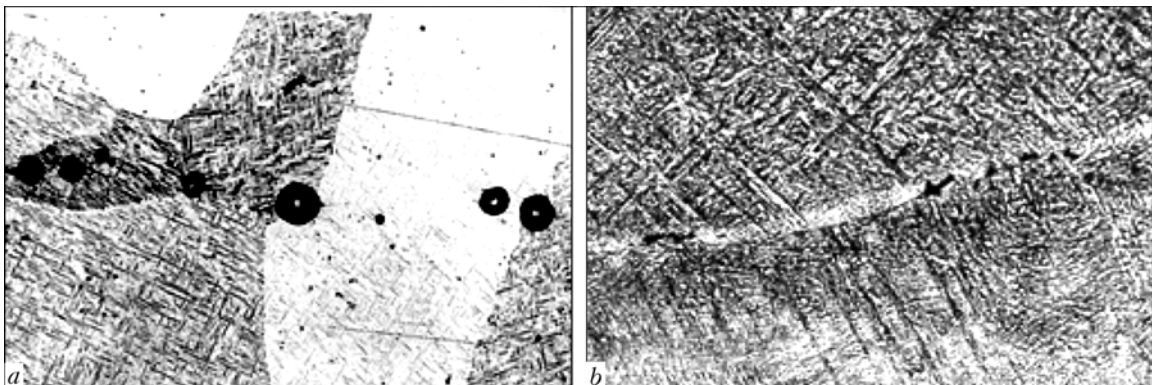
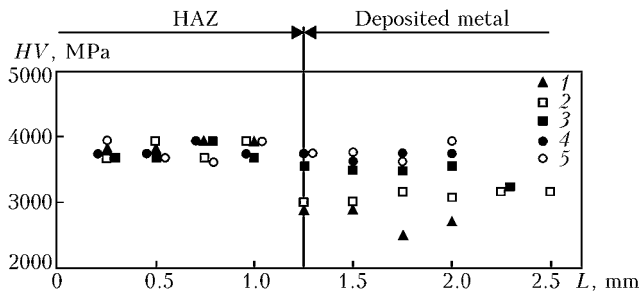


Figure 5. Microstructure of weld metal containing defects caused by violation of the edge preparation technology: a — micropores (x200); b — lacks of penetration (x250)



**Figure 6.** Distribution of microhardness in metal of the blades repaired by using different filler metals: 1 — VT1-00sv; 2 — VT6sv; 3 — VT20-1sv; 4 — VT9; 5 — SP15sv ( $L$  — distance)

est operating reliability of blades after repair. At the same time, it is reported that increase in the amount of  $\beta$ -stabilisers in the weld metal of low and medium titanium alloys leads to decrease in its ductility and toughness, in addition to increase in strength. Therefore, for welding (cladding) alloys of the martensitic grade, where alloy VT9 belongs to, it is recommended [1, 2] to use filler metal with a lower alloying degree.

Fatigue tests of full-scale blades subjected to repair using filler wires of different compositions were conducted to finally decide on a filler metal. Cladding of seals on the blades and repair cladding of leading edges, nicks, chips and erosion damages were performed without groove preparation, but with preliminary scraping and degreasing of the surfaces to be treated. For repair cladding of mechanical damages on the surface of the profile parts of the blades, the defects were preliminarily machined. Cladding parameters are given in Table 3.

The device for argon shielding of the surface of the blade reverse side, which is heated in welding (cladding), was used for repair of all defects.

Fatigue tests of the blades were conducted on a base of  $1 \cdot 10^8$  cycles. The maximal fatigue life on a base of  $20 \cdot 10^8$  cycles at stresses of 300–350 MPa was exhibited by the blades repaired by using wire VT6sv. The blades repaired with wire SP15 (on a base of  $3 \cdot 10^8$  cycles at a maximal stress of 250 MPa) showed the best test results. Therefore, repair cladding of parts of the martensitic type alloys confirmed an assumption of the expediency of using filler metal having a lower alloying degree compared with base metal.

As noted above, if the blades are physically made integral with the disks, and if the airfoils have service

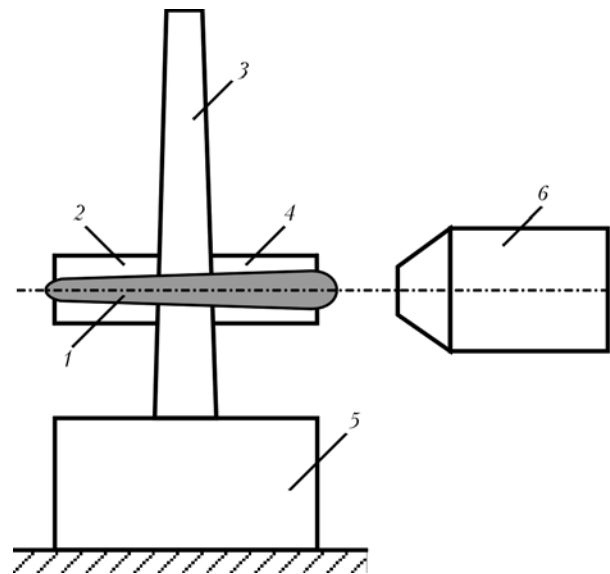


**Figure 7.** Schematic of assembly band for welding airfoils by the EBW method: 1 — weld; 2, 3 — face and reverse sides of the blade band, respectively; 4 — airfoil to be welded; 5 — blade root part; 6 — electron beam gun

damages that are not subject to repair, they can be replaced only by welding a new airfoil to the disk.

Solution of the technological problem was simulated on some detachable blades, the allowance being made for the gap between them on a disk and complexity of subsequent machining of the weld. Airfoils and root parts were assembled using special clamps, the elements being then joined by manual argon-arc welding. Multiple attempts to provide sound welded joints by electron beam welding of the elements assembled by the above method failed to give the positive results. Variations in metal thickness along the length of a joint resulted in either burns-through at the beginning and end of the weld, or (with decreased welding parameters) lacks of penetration in the central part of the blade. Despite the use of run-in and run-off tabs, defects in the form of fade-outs and undercuts were formed in the beam entry and exit locations. With this assembly method it was impossible even to provide the assigned geometry of a welded blade. In this connection, all further studies were aimed at development of assembly bands of alloy VT9, which could, on the one hand, prevent deformation in the welding zone and maintain the set profile of the blade,

**Table 3.** Parameters of repair cladding of blades

Defect type	Filler wire diameter, mm	Welding current, A	Maximal welding time, s	Maximal cooling time, s	Argon flow rate, l/min	
					in torch	for back shielding
Nicks in leading edges	0.8	40	80	160	4–6	2–4
Chips	0.8	50	60	180	5–6	2–4
Mechanical damages	0.8–1.0	60	50	180	6–7	3–4
	0.8–1.0	80	30	180	7–8	4–5

Notes. 1. The parameters given can be adjusted depending on the type, shape and size of a defect. 2. Welding and cooling time depends on the design of a welding torch.

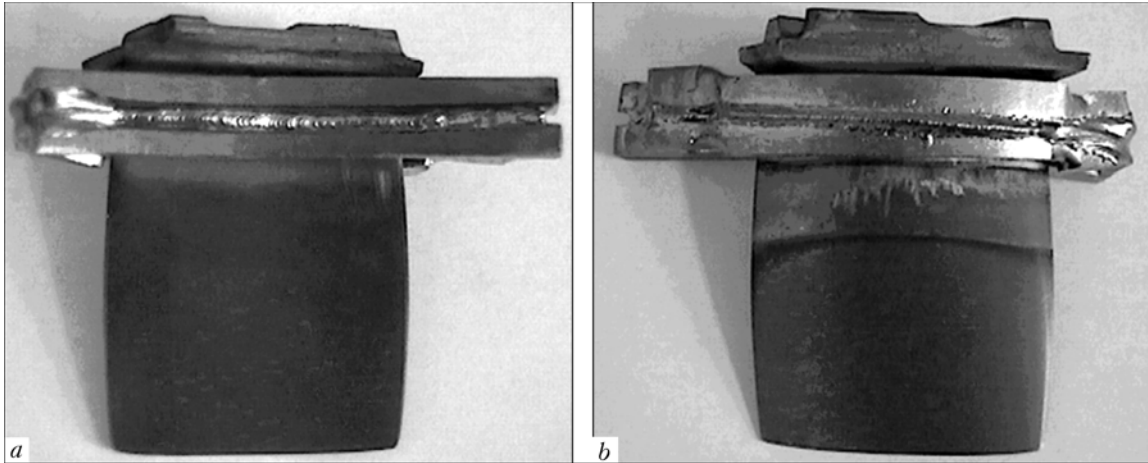


**Figure 8.** Appearance of the face (a) and reverse (b) sides of blade with airfoil welded to it

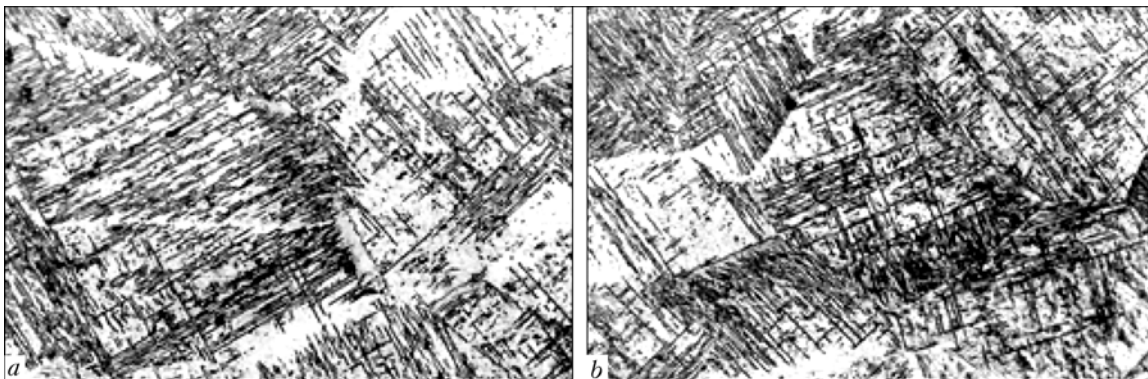


**Figure 9.** Microstructure of metal of EB-welded joint between the airfoil and root part of the blade: a — weld; b — HAZ ( $\times 250$ )

and, on the other hand, ensure constant thickness of the elements welded (Figure 7).

EBW of blade elements assembled in this band was performed in flat position under the following conditions: accelerating voltage  $U_{acc} = 60$  kV, welding current  $I_w = 90$  mA, focusing current  $I_f = 980$  mA, and welding speed  $v_w = 25$  m/h. After welding (Figure 8) the band was removed by machining, and the weld was X-ray inspected. No defects were detected in this case. However, metallography of welded joints revealed isolated micropores not more than 0.07 mm in size, present in the fusion zones.

Microstructure of the cast weld metal consisted of relatively coarse primary  $\beta$ -grains with the martensitic  $\alpha'$ -phase located inside them (Figure 9, a). Similar structure was formed also in the near-weld region of HAZ (Figure 9, b). Values of microhardness (3400–3700 MPa) in different regions of a welded joint were close to that of the base metal.

Fatigue tests of the blades with the airfoils welded by the EBW method were conducted by the same procedure as those of the blades which had been repaired by the argon-arc welding. Tests on a base of  $1 \cdot 10^8$  cycles showed that the fatigue limit of the blades

with welded airfoils was within a stress range of 320–360 MPa.

## CONCLUSIONS

1. The feasibility was proved of reconditioning repair of the profile part of gas turbine engine compressor blades of titanium alloy VT9, made integral with a disk. For this purpose, the special small-size welding torch was designed, manufactured and successfully tested under service conditions.

2. As found on the basis of the results of metallographic examinations and fatigue tests of the repaired blades of alloy VT9, to ensure their high performance it is recommended to carry out repair welding and cladding using welding wire VT6sv.

3. It was suggested that the airfoil and root elements of the blades should be assembled in a special band, and then welded by the EBW method with through penetration using no filler wire to ensure high quality of the welded joints.

1. Gurevich, S.M., Kulikov, F.R., Zamkov, V.N. et al. (1975) *Welding of high-strength titanium alloys*. Moscow: Mashinostroenie.
2. Moiseev, V.N., Kulikov, F.R., Kirillov, Yu.G. et al. (1979) *Titanium alloy welded joints*. Moscow: Metallurgiya.



# RENOVATION OF BODIES OF ENERGY-ABSORBING MECHANISMS OF FREIGHT RAILWAY CARS

V.V. SNISAR, E.L. DEMCHENKO, A.I. FENOGENOV and D.V. VASILIEV  
E.O. Paton Electric Welding Institute, NASU, Kiev, Ukraine

Technology of mechanized arc welding and surfacing without preheating or heat treatment of high-carbon steel 30GSL-B in renovation of bodies of energy-absorbing mechanisms of automatic coupling devices of freight railway cars is presented.

*Keywords:* arc welding, surfacing, body of energy-absorbing mechanism, hardenable steel, renovation technology, preheating, heat treatment, structure, mechanical properties, flux-cored wire, shielding gas, introduction

Reduction of specific quantity of metal per structure, increase of a structure operation reliability and service life are important tasks of state-of-the art machine-building processes. In national railway car-building industry cast parts and units from carbon low-alloy steel of increased strength, for example, bodies of energy absorbing mechanisms of automatic coupling devices, are widely used.

Body of energy-absorbing mechanism of freight railway car is a cast part of complex shape, which is manufactured according to GOST 22253-76 from high-carbon low-alloy steels of increased strength of the types 30GSL-B and 32Kh06L.

In our case possibility is considered of renovating bodies manufactured from steel 30GSL-B (GOST 977-75) of the following chemical composition, wt. %: 0.25-0.35C; 1.1-1.4Mn; 0.6-0.8Si;  $\leq 0.04P$ ;  $\leq 0.04S$ ;  $\leq 0.3Cr$ ;  $\leq 0.3Ni$ ;  $\leq 0.3Cu$ . In case of hardening at 920-950 °C and tempering at 570-650 °C steel 30GSL-B has the following mechanical properties [1]:  $\sigma_{0.2} \geq 400$  MPa;  $\sigma_t \geq 650$  MPa;  $\delta_5 = 14$  %;  $\psi = 30$  %;  $KCU = 49$  J/cm<sup>2</sup>.

In the process of long operation internal surfaces of the body necks are subjected to shock attrition, which causes significant wear of working surfaces and opening of the internal cast defects of the body. Because of this the need occurs in renovation of the parts by surfacing, which would ensure mechanical properties of the metal that are not inferior to those of steel 30GSL-B.

During operation of energy-absorbing mechanisms on internal and external surfaces of their bodies often occur cracks and spallings caused by conditions of operation and cast defects. It is necessary to welding up the latter, whereby a welded joint should be of the same strength as the base metal. Taking into account shape and size of mentioned bodies, the most applicable for their renovation are arc methods of welding and surfacing, in particular, manual welding and surfacing using stick electrodes and mechanized CO<sub>2</sub> surfacing using hose semi-automatic machines.

It is known that steels of the type 30GSL-B are susceptible to formation in HAZ metal of brittle hardening structures under action of thermal cycles of arc welding, which may cause origination of cold cracks at once after welding (surfacing) or in the process of the item operation. That's why existing technologies of arc welding and surfacing of high-carbon steels of mentioned type envisage [2] obligatory preheating and postweld heat treatment of renovated bodies, which makes process of repair much more complex and requires for availability of special thermal equipment.

Known in the field is also technology of welding and surfacing of high-carbon steels without preheating and heat treatment using austenite consumables [2]. However, it may not be used in this case, because it may not ensure deposited materials with sufficiently high wear resistance and mechanical properties characteristic of steel 30GSL-B. In addition, majority of existing technologies for producing high-strength wear-resistant deposit imply presence of cracks on deposited metal, which is unacceptable in our case.

At PWI new method of arc welding (surfacing) of high-strength low- and medium-alloy hardenable steels [3], to which also relate steel of 30GSL-B type, is proposed. This method consists in application of welding consumables, which ensure as a result of decomposition of overcooled austenite ( $\gamma \rightarrow \alpha_m$ ) at temperatures below 200 °C formation in the deposited metal (the weld metal) of austenite-martensite structure. Formation of decomposition products in deposited metal ensures for it a complex of mechanical properties with high strength characteristics and good level of ductility and toughness. Proposed method allows performing arc welding and surfacing of hardenable steels without preheating and postweld heat treatment of welded joints, like in case of using austenite consumables, and receive deposited metal and welded joints with high strength characteristics ( $\sigma_t \geq 900$  MPa). On the basis of this method technologies and materials for mechanized and manual arc welding and surfacing of hardenable high-strength steels were developed at PWI [4].

Welding consumables of new generation of series ANVP for electric-arc welding and surfacing ensure production of deposited metal with various levels of



**Figure 1.** Macro-section of neck fragment of energy absorber body with renovated areas of internal surface

strength ( $\sigma_t = 900\text{--}1200$  MPa) depending upon established requirements. For mechanized  $\text{CO}_2$  welding or in Ar +  $\text{CO}_2$  mixture flux-cored wire PP-ANVP80 was developed. Exactly semi-automatic  $\text{CO}_2$  welding using mentioned wire of 1.6 mm diameter was tested by the authors for renovating bodies of energy-absorbing mechanisms of freight railway cars.

In the process of the technology development optimum parameters of the condition were established:  $I_w = 260\text{--}280$  A,  $U_a = 26\text{--}28$  V. Deviation from mentioned parameters worsens stability of the arc burning and affects saturation of the deposited metal with hydrogen and nitrogen. So, if arc voltage exceeds 29 V, saturation of the deposited metal with hydrogen is observed, which may cause worsening of its ductility properties and even reduction of its resistance against formation of cracks if concentration of hydrogen in the deposited metal exceeds  $6.3 \text{ cm}^3/100 \text{ g}$  of the metal. To ensure reliable protection of the arc and the pool,  $\text{CO}_2$  flow should be within 7–12 l/min. At higher values worsening of welding-technological characteristics is possible.

Welding and surfacing are performed on DCRP using a source with rigid external characteristics. It is recommended to use gas driers and heaters. Stable burning of the arc, good formation of deposited metal,

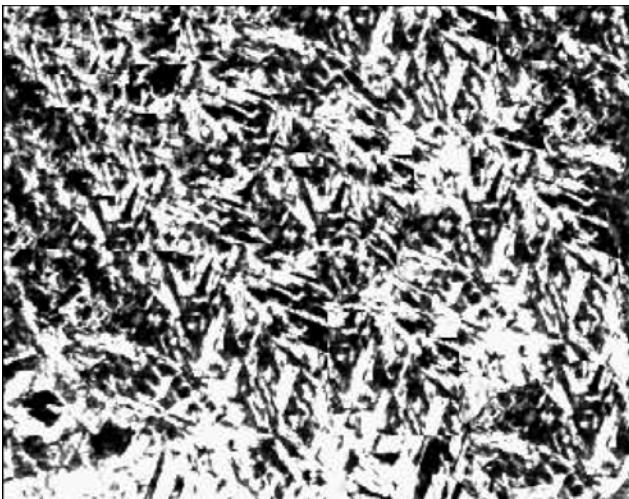


**Figure 2.** Microstructure of deposit of flux-cored wire PP-ANVP80 on steel 30GSL-B ( $\times 600$ )

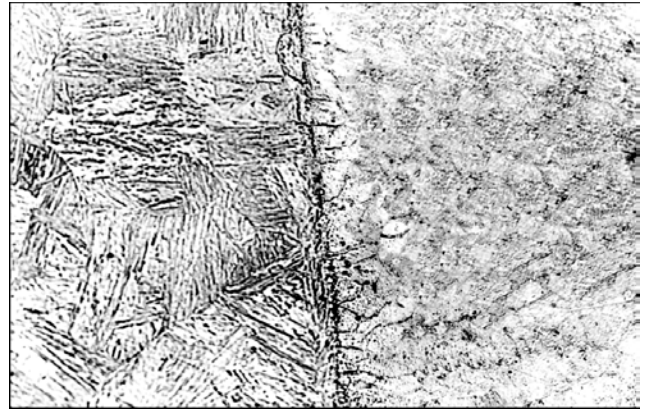


**Figure 3.** Microstructure in fusion zone of deposit of flux-cored wire PP-ANVP80 on steel 30GSL-B ( $\times 320$ )

fine-ripple surface of beads, spontaneous crust separation, and insignificant sputtering are ensured, provided mentioned recommendations are observed. Surfacing is performed by «through-thickness» separate beads with electrode in backward position and deviation of the torch from vertical axis at  $30\text{--}60^\circ$  in direction of surfacing. Each layer is cooled down to  $100^\circ\text{C}$  prior to surfacing the next one, recommended direction of surfacing being in parallel to generatrix of the body neck. Each previous bead should be overlapped by the subsequent one by one third of its width; number of layers of the deposits is not limited. It is allowed to welding up through defects with application of steel and copper backings with subsequent removal thereof.

Estimation of quality of renovating worn surfaces by surfacing and welding up defects was performed taking into account data of metallographic studies of macro- and micro-sections and studies of mechanical properties of deposited and weld metal. Performed metallographic studies of macro- and micro-sections showed that cracks, pores, and other defects were absent in deposited metal, welded joints, fusion zone and HAZ metal (Figures 1–3). Deposited metal has austenite-martensite structure (Figure 2), main component of which is high-strength low-carbon high-al-

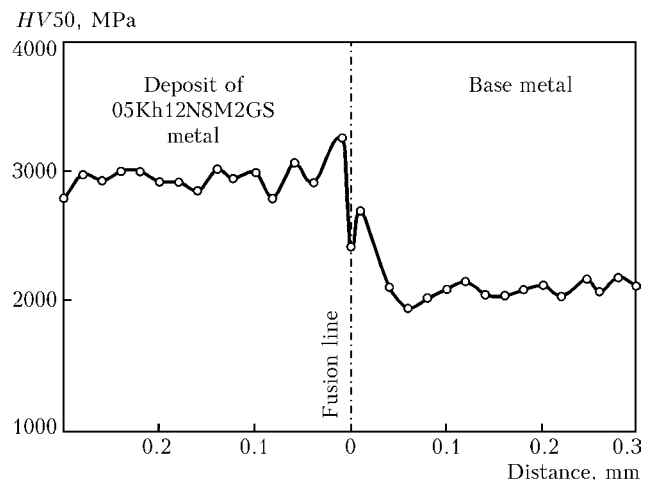


**Figure 4.** Distribution of microhardness in fusion zone of deposited metal with steel 30GSL-B



Mechanical properties of deposited and weld metal produced in welding up a crack on steel 30GSL-B using semi-automatic CO<sub>2</sub> welding with flux-cored wire PP-ANVP80 of 1.6 mm diameter without preheating and heat treatment

Area of study	$\sigma_{0.2}$ , MPa	$\sigma_t$ , MPa	$\delta_5$ , %	$\psi$ , %	KCU <sub>+20</sub> , J/cm <sup>2</sup>	KCU <sub>-60</sub> , J/cm <sup>2</sup>
Deposit	835.0–870.2	1074.1–1084.5	11.0–12.8	32.0–34.0	55.0–62.0	35.0–40.0
	847.5	1079.64	12.04	33.6	60.0	37.8
Weld metal	765.0–820.2	1045.0–1082.0	11.0–12.5	25.0–30.0	55.0–62.0	32.0–38.0
	795.0	1064.4	11.8	28.8	58.8	34.4

Note. In numerator minimum and maximum values obtained in testing of five specimens, and in denominator mean values are given.

loy martensite (up to 85 wt.%), residual austenite, and the rest ---  $\delta$ -ferrite. Mechanical properties of deposited and weld metal in welding up defects on steel 30GSL are given in the Table, and distribution of microhardness in zone of the deposited metal fusion with steel 30GSL is shown in Figure 4.

Level of strength characteristics of the deposited metal significantly exceeds requirements established by GOST 977–75 to steel 30GSL-B properties, but in this case it is quite admissible, because it allows increasing wear resistance of working surfaces of renovated bodies and prolonging their service life.

Proposed technology for renovating bodies of energy-absorbing mechanisms passed trials at Stry and Darnitsa railway car repair plants. Positive results of the trials were registered in respective acts. Technology for renovating bodies of energy absorbers and flux-cored wire PP-ANVP80 were introduced into pro-

duction. The technology is included into departmental manual on welding and surfacing for repair of freight railway cars and containers (TsV-0019).

*Flux-cored wire PP-AN-VP80 is commercially produced at the E.O. Paton Electric Welding Institute. Information on conditions of purchase and technological support may be obtained by tel.: (044) 287-6546, fax (044) 271-2439.*

1. Sorokin, V.G., Volosnikova, A.V., Vyatkin, S.A. et al. (1989) *Steel and alloy grade classification*. Ed. by V.G. Sorokin. Moscow: Mashinostroenie.
2. (1974) *Technology of electric welding of metals and alloys*. Ed by B.E. Paton. Moscow: Mashinostroenie.
3. Gotalsky, Yu.N., Snisar, V.V., Kuprev, A.L. et al. *Method of arc welding of quenching steels*. USSR author's cert. 880671. Int. Cl. B 23 K 28/00. Publ. 15.11.81.
4. Snisar, V.V., Demchenko, E.L., Ivanchenko, E.V. (2000) Challenging technologies for high-strength steel welding without preheating and heat treatment. *The Paton Welding J.*, **11**, 37–40.

## OF BODY PARTS WELDING OF OFF-SHORE PIPELINES

At the E.O. Paton Electric Welding Institute the following adhesion-bonded technologies for repair of body parts have been developed:

- single-sided resistance spot welding of thin-sheet cover plates over the layer of adhesive, preliminary deposited on the mating surfaces;
- stud welding, deposition of adhesive with a next fixation of a strengthening part using an adhesion-threaded joint;
- trepanning of cracks, intermittent welding, filling of interweld space with an adhesive composition (Photo);
- restoration of geometry of working surfaces and repair of cracks using high-filled adhesive compositions.

Special adhesive compositions are developed for each technology, providing the quality repair works under different service conditions.

**Purpose and application.** Repair of components of internal combustion engines, casings of compressors, working chambers and blades of hydraulic pumps, pipelines without interruption of transportation of products.

**Proposals for co-operation.** Implementation of technology at the Customer's facility and delivery of repair adhesives.



Contacts: Prof. Lobanov L.M.  
E-mail: office@paton.kiev.ua



## SYSTEM OF LASER FOLLOWING OF WELD REINFORCEMENT

F.N. KISELEVSKY, E.V. SHAPOVALOV and V.A. KOLYADA  
E.O. Paton Electric Welding Institute, NASU, Kiev, Ukraine

A system of laser following of weld reinforcement has been developed, which is designed for operation as part of an automated ultrasonic testing unit. The system allows performing automatic correction of the US transducer position relative to the reinforcement with the required accuracy.

*Keywords:* non-destructive testing, weld, laser following, reinforcement bead, optical sensor, AUST unit, automatic correction, device for discrete input-output

In connection with increased requirements to the quality of welded pipes applied in construction of the main pipelines, modern units for automated ultrasonic testing (AUST) should be used for a guaranteed detection of defects in longitudinal welds. During ultrasonic testing of longitudinal pipe welds, transverse displacements of the weld relative to the ultrasonic transducers are observed, which essentially influences the testing quality.

The E.O. Paton Electric Welding Institute developed a system for laser following (LFS) of the weld reinforcement for NK 360 ultrasonic unit, which is described in [1]. The main purpose of the LFS is detection of transverse displacement of the reinforcement bead center relative to a certain fixed position, and formation of transverse correction signals. The latter are sent to the master controller of AUST unit, which directly controls the drive of the module of horizontal displacement of the console with ultrasonic transducers.

The following system consists of the two main components, namely optical TV sensor, based on the laser triangulation method, and LFS controller based

on an industrial computer. Laser triangulation method is described in [2], and generalized block-diagram of LFS is given in Figure 1.

The optical TV sensor includes two basic elements: laser linear oscillator, projecting a narrow light band on the pipe surface, and video camera filming the image of the light band projection. Each image frame is transmitted to LFS controller for processing, which results in evaluation of transverse displacement of the reinforcement bead center. LFS controller also has the function of interaction with the main controller of AUST unit by means of reception/generation of discrete information and controlling signals.

LFS controller is designed for solving the following subtasks: digitizing the video signal coming from the optical TV sensor, preprocessing of the digitized video signal, taking a decision on the obtained signal characteristics, evaluation of transverse displacement of the reinforcement bead center, and interaction with the main controller of AUST system.

Video signal digitizing is performed using video capture devices, included into the hardware means of LFS controller. In the digital form each frame, captured from the video flow, is a matrix of integer numbers, in which the element index corresponds to the position of points in the image, while the element

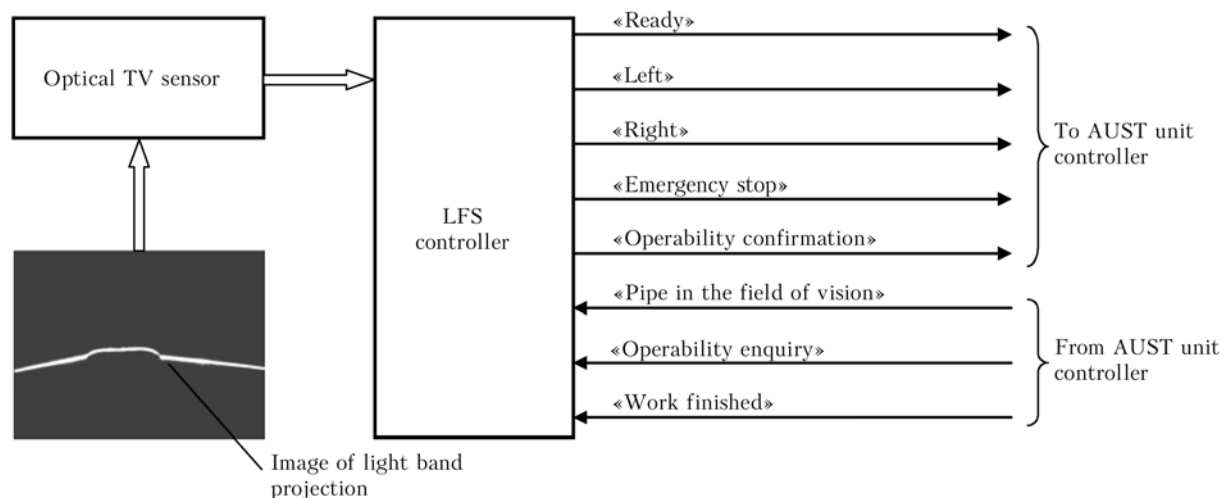


Figure 1. LFS block-diagram



value is directly proportional to the pixel brightness intensity. The main purpose of image preprocessing procedure consists in isolation of the contour of light band projection. The contour is a curve, corresponding to the kind of the measured object surface. Signal analysis is performed using a totality of decision functions based on the image preprocessing results. Analysis result is a decision on the degree of correspondence of the obtained curve to the contour of weld bead reinforcement. If the contour curve corresponds to the reinforcement bead, further processing of the image is performed. Otherwise processing is interrupted, and the system signals about a malfunction in the following process.

Evaluation of transverse displacement of the reinforcement bead center includes the following operations:

- determination of points in the image, which correspond to the edges and center of weld reinforcement bead;
- conversion of point co-ordinates from the image co-ordinate system into a system of real space co-ordinates, i.e. transition from image pixels to millimeters;
- determination of the extent and direction of transverse displacement of the reinforcement bead center relative to the reference point of the following system (the latter is established during adjustment).

To perform the transition from the image pixels to millimeters of the real space, first a procedure of sensor calibration is performed using a standard. The applied method of calibration of triangulation optical sensors is described in [3]. Figure 2 gives the results of image processing and evaluation of the transverse displacement of the reinforcement bead center.

Interaction of the following system with the controller of AUST unit is performed through the discrete input-output device with a galvanic decoupling. Output discrete signals are as follows:

- «Ready» --- following system is ready for operation;
- «Right» --- signal of correction to the right;
- «Left» --- signal of correction to the left;
- «Emergency stop» --- failure of following system;
- «Operability confirmation» --- confirmation of the working condition of the following system.

Input signals:

- «Pipe in the field of vision» --- switching on the automatic following mode;
- «Operability enquiry» --- enquiry about the (working) condition of the following system;
- «Work finished» --- automatic switching off of the following system controller.

After switching on LFS controller and loading the software, the following system generates a «Ready» signal and goes into standby mode (automatic correction is off). When «Pipe in the field of vision» signal comes, the automatic following mode is switched on, during which the correction actions «Right» and «Left» are applied, depending on the direction of

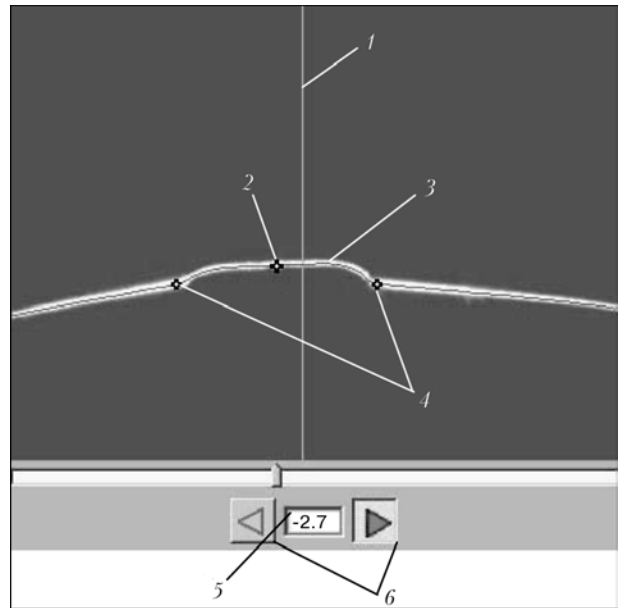


**Figure 2.** Results of image processing: 1 — axis determining the system reference point; 2 — reinforcement bead center; 3 — contour of light band projection; 4 — reinforcement bead edges; 5 — mismatch value, mm; 6 — indicators of correction direction

transverse displacement of the reinforcement bead center relative to the system reference point.

The following system has a certain insensitivity zone, thus allowing prevention of development of the self-oscillation mode at certain settings of the transverse correction drive. Dimensions of the insensitivity zone determine the accuracy of the following process. When the high potential at the «Pipe in the field of vision» input disappears, the system goes into standby mode. If the following system cannot find the reinforcement bead for a certain time, an error message --- «Emergency stop» output signal is sent to the AUST unit controller. As LFS controller is based on industrial computer, there is always a probability of its accidental «hanging». Program-hardware watchdog timer was implemented to determine this type of malfunction. AUST unit controller sends «Operability enquiry» signal to the following system, and waits for a reply in the form of «Operability confirmation» signal for a certain time. If such a signal is received,

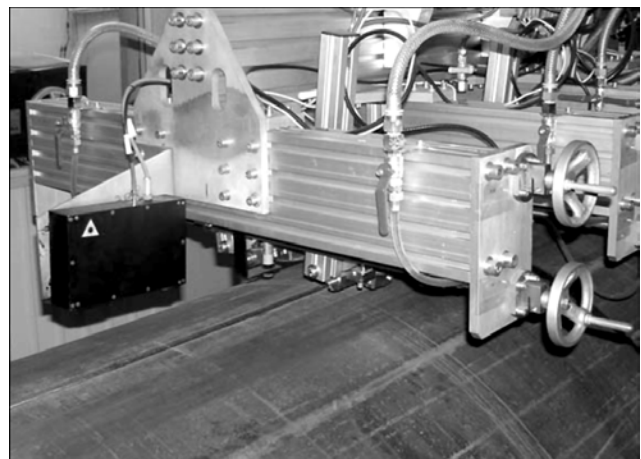


**Figure 3.** TV sensor on the first acoustic module of NK 360 unit



AUST system controller again generates an «Operability enquiry» signal, etc. If the «Operability confirmation» signal has not come to the AUST controller input during the set time interval, a decision is taken about a malfunction of the following system.

When «Work finished» signal is received, the following system automatically correctly switches off the LFS controller power.

**LFS specification**

Accuracy of following the bead reinforcement, mm .....	±0.5
Admissible height of reinforcement bead, mm .....	0.5–3.5
Working zone in the transverse direction, mm .....	±30
Nominal distance from sensor module lower panel to the pipe, mm .....	100
Working zone along the vertical, mm .....	±20
Average time of system reaction, ms .....	40
Working temperature range, °C .....	5–50

As NK 360 unit has two acoustic modules, two independent following systems are installed in it, their

functioning being supported by one LFS controller. Figure 3 shows a TV sensor, mounted on the first acoustic module.

The following system has successfully passed production trials as part of NK 360 unit at the plant of OJSC «Vyksunsky Metallurgichesky Zavod». Similar systems can also be used in other sectors of production automation. Work is currently in progress to develop automatic following systems for the mills for inner and outer welding of longitudinal butt welds of large-sized pipes.

1. Najda, V.L., Mozzhukhin, A.A., Lobanov, O.F. (2004) New generation of equipment for automatic ultrasonic testing of welded pipes. *The Paton Welding J.*, **9**, 57–61.
2. Boillot, J.P., Noruk, J. (2002) The benefits of laser vision in robotic arc welding. *Welding Technique*, **8**, 33–34.
3. Kiselevsky, F.N., Kolyada, V.A. (2005) Calibration of triangular optical sensors. *The Paton Welding J.*, **5**, 48–49.

## TECHNOLOGY OF REPAIR WELDING OF RAILWAY ROLLING STOCK COMPONENTS

A technology has been developed for welding up cracks in such critical components of railway cars as automatic couplers and coupler yokes, spring beams, side frames of car trucks, open freight car posts. All the above carrying parts, except for posts, are made of difficult-to-weld cast carbon low-alloyed structural steels of type 20L, 20GL, 35L, etc. Developed technology of repair welding does not require any preheating of the parts or postweld heat treatment, and the welded joints do not have any defects and are equivalent to the base metal.



Cracks in the traction yokes welded up on the outside



Welded-up through-thickness crack in the rear part of automatic coupler head



Welded-up crack in the automatic coupler case in the tail piece transition to the head



Welded-up longitudinal cracks in the carriage side frames

Contacts: Dr. Maksimov S.Yu.  
E-mail: maksimov@paton.kiev.ua



# CONTENT OF ACICULAR FERRITE IN WELD METAL IN WET WELDING

S.Yu. MAKSIMOV and D.V. KRAZHANOVSKY  
E.O. Paton Electric Welding Institute, NASU, Kiev, Ukraine

Influence of weld metal alloying in flux-cored wire underwater welding on the proportion of microstructural components was studied. Possibility of a considerable increase of the share of acicular ferrite in the deposited metal due to its alloying with titanium and boron was established.

*Keywords:* underwater welding, flux-cored wire, weld metal, alloying, microstructure, acicular ferrite

Welding is the main process (similar to regular conditions) in repair of underwater metal structures. In most of the cases, it is performed (despite the high cost) using specialized chambers, isolating the work zone from ambient water and providing a high quality of the produced welds. Wet welding can be a real alternative to such a process. However, its application is limited by several factors, one of which is an insufficient level of mechanical properties, primarily, ductility. In view of the engineering complexity of using the techniques applied in practical welding in air, a solution to this problem can be found using metallurgical methods.

Addition of titanium and boron to the flux-cored wire charge allowed the authors of [1] to achieve an essential improvement of the properties of weld metal of ferrite type by increasing the content of acicular ferrite (AF) in its structure up to 90%. As in welds of a similar type, made under the water with the currently available electrode consumables, the main structural components are grain-boundary ferrite (F) and ferrite with the secondary phase, while AF fraction is usually not higher than 20%, it appears promising to improve the weld metal ductility through optimization of its structure.

The purpose of this work is studying the influence of titanium and boron additives to the flux-cored wire charge on the weld metal structure and AF content in it.

A series of flux-cored wires of PPS-AN1 type [2] were manufactured for the investigations, to the charge of which FeTi (FTi65, GOST 4761-80) and FeB (Fb-1, GOST 14848-69) were added. As there is no published data on titanium and boron transition from the flux-cored wire into the weld in underwater welding, the amount of FeTi and FeB in the charge was varied in a quite broad range of 0-15 and 0-3%, respectively, to ensure up to 0.08% Ti and 0.008% B in the deposited metal (similar to the data given in [1]). Flux-cored wires were drawn down to a diameter of 1.8 mm with the fill factor of 32-34%. Bead deposition on St3 steel plates was performed in a laboratory water tank at 1 m depth in the following modes:  $U_a =$

$= 30-32$  V,  $I_w = 160-180$  A, at reverse polarity current.

Samples for metallographic examination and composition analysis were cut out of the deposited metal. Obtained results are given in the form of 3D graphs. Titanium being an extremely strong deoxidizer, should promote an essential lowering of oxygen content in the weld metal. As is seen from Figure 1, at minimum alloying level (0% B and 0.0014% Ti) oxygen concentration in the weld is close to 0.12%. At increase of titanium content in the weld up to 0.045% and that of boron to 0.007%, oxygen content drops to 0.04%, i.e. almost 3 times. Obtained data are indicative of the effectiveness of titanium and boron impact on oxygen concentration in the weld metal. A similar dependence is also found in welding in air, but at a lower oxygen concentration [1].

Influence of titanium and boron alloying on weld metal hardness is shown in Figure 2. The dependence has several extremums, to which the low and high values of hardness correspond. Hardness rises at increase of titanium and boron content, reaching maximum values in the region of the highest contents of alloying elements. A number of combinations of titanium and boron content (0.015-0.02 and 0-0.001%;

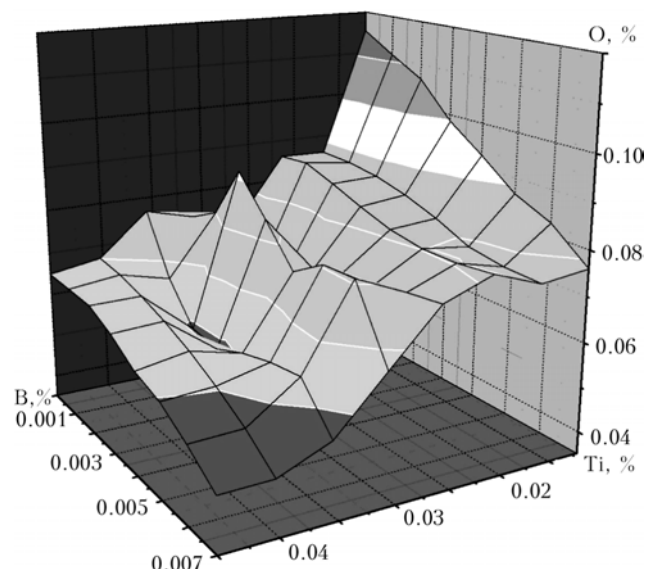
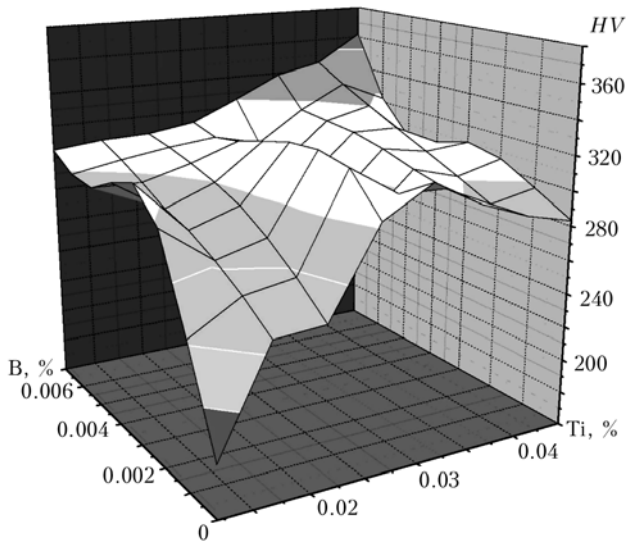
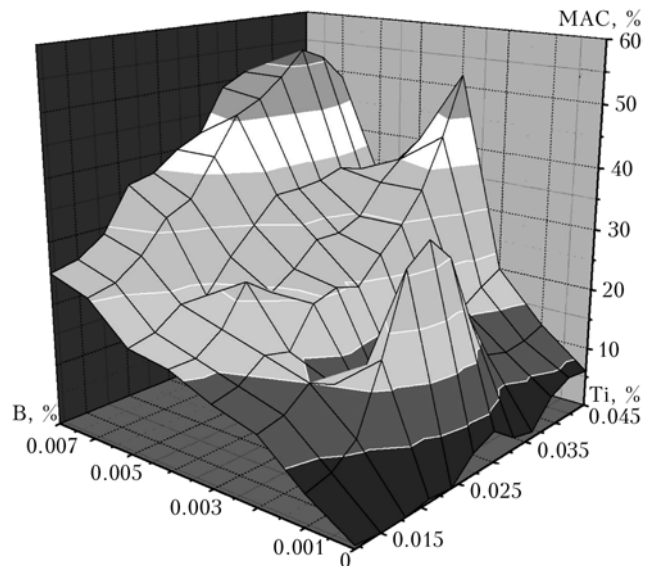


Figure 1. Influence of weld metal alloying with titanium and boron on oxygen concentration in it



**Figure 2.** Influence of weld metal alloying with titanium and boron on its hardness



**Figure 5.** Influence of weld metal alloying with titanium and boron on content of martensite and MAC-phase in the weld metal

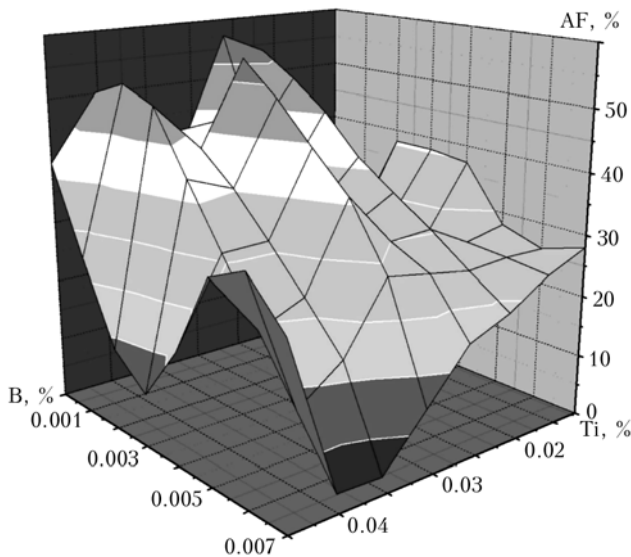


**Figure 3.** Influence of weld metal alloying with titanium and boron on AF fraction in the weld metal

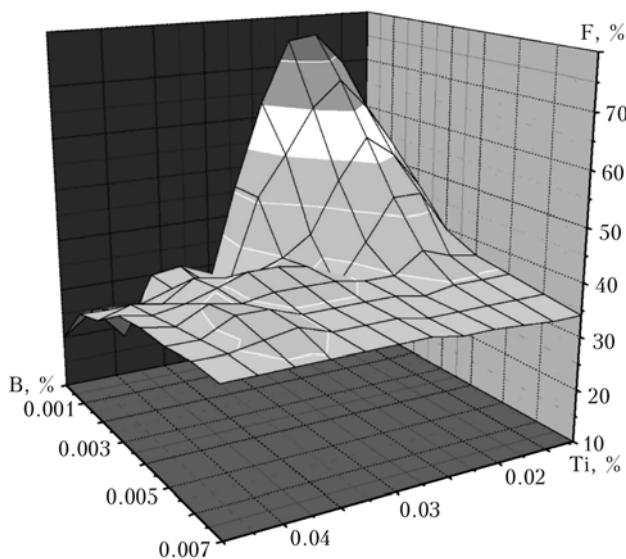


**Figure 4.** Influence of weld metal alloying with titanium and boron on fraction of ferrite with secondary phase in the weld metal

0.025–0.035 and 0.0015–0.002 %, respectively), provide a relatively soft and possibly more ductile structure.

Metallographic analysis also revealed martensite and MAC-phase in the deposited metal, in addition to various ferrite modifications. Figure 3 shows the influence of alloying on AF formation, as well as existence of two regions, in which AF amount exceeds 50 %. The highest AF content corresponds to weld alloying with approximately 0.025 % Ti and 0.001 % B. At a low alloying level (0–0.02 % Ti and 0–0.0002 % B) AF content is quite negligible. This range of compositions is characterized by a high content of ferrite with the secondary phase (Figure 4). At increase of titanium content above 0.035 % and that of boron above 0.003 %, the susceptibility to hardening structure formation is markedly increased, and the weld develops martensite and MAC-phase (Figure 5). Such an effect is known in metallurgy, when small boron additives at a low content of carbon essentially increase the steel hardenability [3].

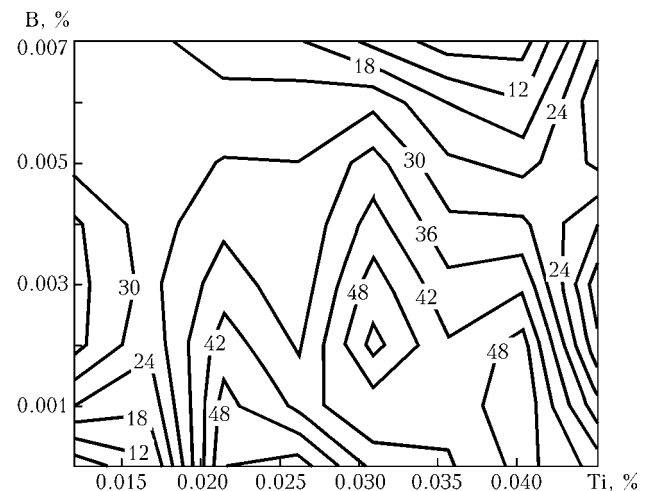


**Figure 6.** Dependence of AF content in the deposited metal on boron and titanium content



For a comparative estimate it is more convenient to present the dependence of AF content on alloying in the form of a contour map (Figure 6). Compared to the results obtained in air [1], the optimum range of titanium and boron content in terms of obtaining the maximum amount of AF, shifts towards their smaller values.

Thus, performed studies confirmed the possibility of a considerable increase of AF content in the metal of welds, made under the water by weld alloying with titanium and boron. However, the effectiveness of this measure turned out to be almost 2 times lower than

in welding in air. Two regions with the maximum AF content on the level of 56–57 % were found in the studied compositional range. Here the content of titanium and boron in the weld metal is 0.023–0.027 % and 0–0.0002 % for the first region, and 0.03–0.032 % and 0.0016–0.0023 % for the second one, respectively.

1. Oh, D.W., Olson, D.L. (1990) The influence of boron and titanium on low-carbon steel weld metal. *Welding J.*, **4**, 151–158.
2. Savich, I.M. (1969) Underwater flux-cored wire welding. *Avtomatich. Svarka*, **10**, 70.
3. Meskin, V.S. (1959) *Principles of steel alloying*. Moscow: Metallgizdat.

## THESIS FOR A SCIENTIFIC DEGREE

### Priazovsky State Technical University

**I.A. Galtsov** (East-Ukrainian National University) defended on 21 October 2005 candidate's thesis «Quality Improvement of Metal Structures of Austenite Metastable Steel 10Kh1318DU by Welding with Forced Cooling».

The dissertation is devoted to study of weldability and quality improvement of welded joints of austenite steel 10Kh13G18DU (DI-61U) by application of forced cooling.

One of the methods of improving mechanical properties and structure of welded joints of austenite steels is their postweld austenitization (heating up to 1150–1100 °C and rapid cooling). But because of impossibility of performing heat treatment in manufacturing large-size metal structures (bodies of railway cars), method of welding with forced cooling was developed, which allows obtaining welded joints with required properties.

In the work on the basis of experimental data mechanical characteristics, phase-structural composition, resistance to corrosion and crack formation, and level of formation of residual stresses and strains in welded joints in welding without forced cooling and with cooling are analyzed. Behavior of steel 10Kh13G18DU in high-temperature heating is studied and it is shown that level of stresses, undesirable structures and phases, and probability of crack formation may be reduced by reducing the time of the weld and HAZ metal stay within critical temperature range of phase-structural transformations. Such conditions may be achieved by forced cooling of welded joints. Optimum rates of forced cooling are  $w_{6-5}^{cool} = 100-$

110 °C/s, but not more than  $w_{6-5}^{cool} = 120$  °C/s within temperature range 600–500 °C.

For the purpose of measuring residual stresses and determining phase-structural composition of the weld metal and near-weld zone method of magnetic diagnostics of welded joints by change of the percent content of  $\alpha$ -phase (martensite) was developed.

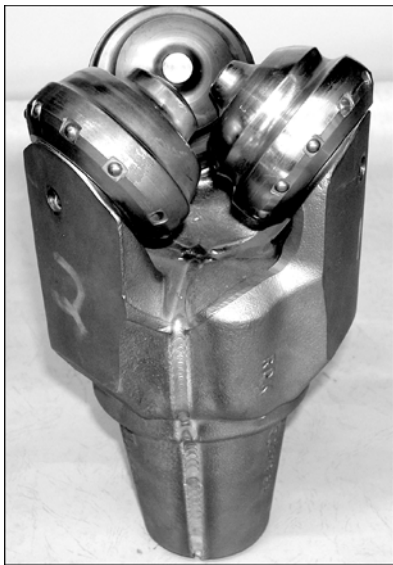
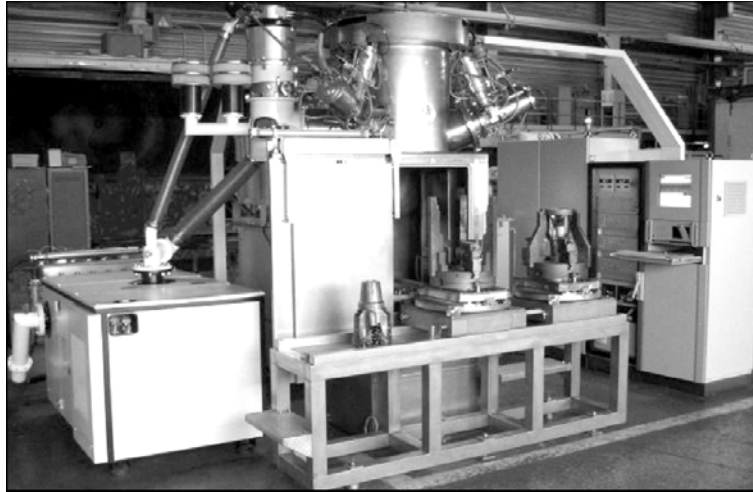
Adoptable to stream-lined production heat-absorbing materials and mediums are found, which may be used in commercial production. The cheapest and the most adoptable to stream-lined production heat absorbers for application under commercial production conditions are activated (seething) layer of a liquid ( $w_{6-5}^{cool} = 110-115$  °C/s) and porous materials (glass wool and mineral wool) impregnated with liquid ( $w_{6-5}^{cool} = 20-25$  °C/s).

It is shown on example of the developed welding benches for welding side walls and entrance doors of Diesel trains that combined use of porous materials and activated layer of liquid is advisable.

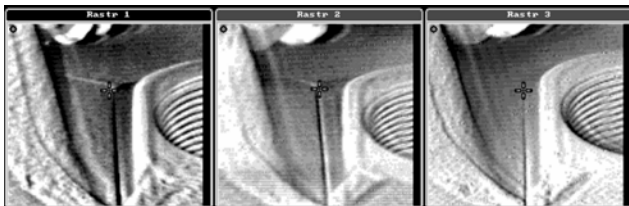
Occurrence of strains and stresses in elements of Diesel and electric trains (side walls, entrance and tambour doors) at all stages of technological manufacturing process is studied (assembly-welding of individual modules, leveling and straightening of modules, assembly-welding of car bodies, and trial runs).

Developed method of welding (with forced cooling) makes it possible to significantly facilitate operation of assembly-welding of carriages of Diesel and electric trains, excludes laborious operation of leveling and straightening, significantly increases purity of welded joints in regard to the content of carbides, allows controlling phase-structural state, and increases resistance of metal against intercrystalline corrosion and formation of cracks.

## 3-GUN MACHINE KL-117 FOR ELECTRON BEAM WELDING OF DRILL BITS



✓ Machine is intended for electron beam welding of drill bits up to 17.5" diameter with simultaneous performance of three welds, thus increasing both accuracy of drill bits dimensions and welding output.



✓ Application of a powerful control electronic tube in the accelerating voltage source prevents the arc processes in the welding gun by a short interruption of accelerating voltage, which does not lead to weld formation defects.

✓ The RASTR system, functioning on the principles of raster electron microscope, enables following the welding process and automatic coquidance of each of three electron beams to the butts of groove faces in the real time. The clear picture of the welding process is displayed on the monitor screen and is not exposed to the welded metal vapors, which is characteristic for traditional optical observing systems.

✓ Machine is provided with the electron beam diagnostic system allowing an operator:

- to define the beam focusing plane position prior to welding;
- to periodically evaluate changes in space and energy beam parameters in order to define the necessity of the welding gun cathode replacement.

✓ Lanthanum hexaboride cathode as a tablet has service life of not less than 40 h in the welding mode at beam power of 20 kW, and the beam axis position does not change at changes in beam focusing.

✓ Control of all equipment subsystems by means of CNC + PLC.

✓ The computer system of electron beam scanning stabilizes the molten pool state and improves the quality of face and root surfaces formation of the weld.

E.O. Paton Electric Welding Institute of NASU  
11, Bozhenko Str., 03680, Kiev, Ukraine; Tel./ fax: (38044) 525 4319  
E-mail: nazarenko@technobeam.com.ua www.nas.gov.ua/pwj/beam/index.html



## FORTHCOMING BOOK INFORMATION

**Vladimir I. Makhnenko, Viktor E. Pochynok. STRENGTH CALCULATION OF WELDED JOINTS WITH CRACK-LIKE IMPERFECTIONS.**

**Approx. 266 pp., 165 × 235 mm, hardback. November 2005. US\$ 90**

In this manuscript, the idea of the fitness-for-purpose concept is used to improve strength calculations of welded joints with crack-like imperfections caused by structural or technological factors. These include welded joints with fillet, spot, slot and butt welds having sharp fissures brought by geometry of the elements welded and limited sizes of the weld sections. Such joints are widely encountered in modern general-purpose welded structures used in civil building, shipbuilding, automobile industries, etc.

The welded joints just mentioned do not usually cause problems for structures of relatively ductile materials with small-to-medium thicknesses of component sections, and operating under predominantly static loading. However, the use of new structural materials, especially high-strength steels and aluminum alloys, etc., large cross sections of structural elements, and loading with alternate loads, requires a certain caution to be taken. Nonetheless, the technological advantages that these joints produce attract an interest in their use, of course, when it does not cause any harm to the structure safety and its residual service life.

Performing strength calculations based on the fitness-for-purpose criterion for the joints encountered in general-purpose structures, allows ensuring the requirements concerning the service life-time. However, there is a difficulty of implementing such calculations in wide engineering practice. As shown by the authors, a successful implementation of the mentioned concept for general-purpose welded joints and for wide range of users is possible only when it is based on the use of corresponding computer systems with friendly user interface, which do not require a user to have a special knowledge in fracture mechanics, deformation mechanics, numerical methods, etc. Such systems are to be portable and efficient, i.e. calculations of appropriate section sizes or verification of strength of specific joints should be done promptly. In turn, it requires development of numerical procedures and creation of specialized databases that simplify and accelerate calculations.

**Viktor Ya. Kononenko. TECHNOLOGIES OF UNDERWATER WET WELDING AND CUTTING.**

**Approx. 140 pp., 140 × 200 mm, softback. December 2005. US\$ 40**

The book deals with the features of arcing, metal transfer and joint formation in consumable-electrode wet underwater welding. Principles of development of coated electrodes and self-shielded flux-cored wires for underwater welding and cutting are established. Characteristics of welding consumables and mechanical properties of weld metal are given. Some types of joints, procedure of preparation and fit-up for welding, possible defects of the joints and methods to prevent their formation are described.

Information on characteristic damage to the underwater metal structures is generalized, and technological solutions are given, which have been implemented during restoration of their performance, using wet processes of underwater welding and cutting. The book gives the characteristics of the equipment for implementation of underwater arc welding process.

The main processes of thermal underwater cutting are presented, and characteristics of consumable materials and equipment for its implementation are described. Examples of work performance using underwater cutting are given.

The book is designed for scientific and engineering-technical personnel, qualified welders-divers involved in design, fabrication and repair of underwater constructions.

The book is written by a specialist, who is developing electrode materials and technologies and has a vast experience of practical work under the water.

**TITANIUM: Titanium and its alloys. Technologies. Equipment. Production. Electrometallurgy. Welding****Approx. 180 pp., 200×290 mm, softback. December 2005. US\$ 50**

The collection presents papers on electrometallurgy and welding of titanium and its alloys published between 2002 and 2005 in «Advances in Electrometallurgy» and «The Paton Welding Journal» journals. The authors of the papers are scientists and specialists in the field of titanium and its production, known in Ukraine and abroad. The collection is designed for a broad range of readers dealing with the problems of production, processing and use of titanium.

**ORDER FORM**

Please return to:

**International Association «Welding»**,  
11, Bozhenko str., Kiev, 03680, Ukraine  
Tel.: (38044) 287 6757, 287 6049, 529 2623  
Fax: (38044) 287 4677  
E-mail: journal@paton.kiev.ua; tomik@mac.relc.com

Please send me:

- Vladimir I. Makhnenko, Viktor E. Pochynok «Strength Calculation of Welded Joints with Crack-Like Imperfections». US\$ 90, postage included
- Viktor Ya. Kononenko «Technologies of Underwater Wet Welding and Cutting». US\$ 40, postage included
- «Titanium». Collection of Scientific Paper. US\$ 50, postage included

How to Pay and Payment Details

- By bank transfer (or mail a cheque) into our account  
№ 2600801283433  
UKREXIMBANK, Kiev, Ukraine  
S.W.I.F.T.: EXBSUAUX  
CORR. ACC. #04-094-227  
Bankers Trust Company,  
New York, U.S.A.  
S.W.I.F.T.: BKTR US 33

 Please Invoice Your Details

Name \_\_\_\_\_

Organization \_\_\_\_\_

Address \_\_\_\_\_

Signed \_\_\_\_\_ Date \_\_\_\_\_

